Technische Universität München

Fakultät für Physik

Unique Stepping Behavior of Kinesin-2

Kinesin Stepping: One Head at a Time

Dissertation by

Willi Leopold Stepp

Technische Universität München
Fakultät für Physik

Unique Stepping Behavior of Kinesin-2

Kinesin Stepping: One Head at a Time

Willi Leopold Stepp

Vollständiger Abdruck der von der Fakultät für Physik der Technischen Universität München zur Erlangung des akademischen Grades eines Doktors der Naturwissenschaften (Dr. rer. nat.) genehmigten Dissertation.

Vorsitzender:

Prof. Dr. Martin Zacharias

Prüfer der Dissertation:

1. TUM Junior Fellow Dr. Zeynep Ökten
2. Prof. Dr. Hendrik Dietz

Die Dissertation wurde am 17.12.2019 bei der Technischen Universität München eingereicht und durch die Fakultät für Physik am 02.03.2020 angenommen.

List of publications

Kinesin-2 motors adapt their stepping behavior for processive transport on axonemes and microtubules.
Stepp WL, Merck G, Mueller-Planitz F, Ökten Z
EMBO Rep 2017;18:1947–56. doi:10.15252/embr.201744097.

Resolving kinesin stepping: one head at a time.
Stepp WL, Ökten Z.
Life Science Alliance 2019; 2, 5. doi:10.26508/lsa.201900456.

Reconstitution reveals motor activation for intraflagellar transport.
Mohamed MAA, **Stepp WL**, Ökten Z.
Nature 2018;557:387–91. doi:10.1038/s41586-018-0105-3.

Myosin Va's adaptor protein melanophilin enforces track selection on the microtubule and actin networks in vitro.
Oberhofer A, Spieler P, Rosenfeld Y, **Stepp WL**, Cleetus A, Hume AN, Ökten Z.
Proc Natl Acad Sci 2017. doi:10.1073/pnas.1619473114.

Kinesin-2 from C. reinhardtii is an atypically fast and auto-inhibited motor that is activated by heterotrimerization for intraflagellar transport.
Sonar P, Youyen W, Cleetus A, Wisanpitayakorn P, Mousavi IS, **Stepp WL**, Hancock WO, Tuezel E, Ökten Z.
bioRxiv, 11 2019. doi:10.1101/855940.

Summary

In eukaryotic cells, molecular motors provide means for directed long-range transport on the cytoskeleton that cannot be accomplished by diffusion alone. Kinesin is one such microtubule-based motor that is deployed for active transport throughout the cell and in specialized cell protrusions called cilia. At least 45 different kinesin motors are encoded in the human genome many of which are essential for astonishingly diverse tasks.

The so far best understood kinesins are homodimeric with two N-terminal catalytic 'heads' that are dimerized via coiled-coil interactions in the respective stalk domains. Two co-ordinated ATP-hydrolysis cycles in the heads deliver the energy for a 'hand-over-hand' type of movement that closely resembles human walking. It is long-known that the distal C-terminus, the so-called tail domain, can fold back onto the head domains and suppress the motor's ATPase activity. This auto-inhibitory folding is thought to be brought about by a 'kink' that is found roughly in the middle of the stalk domain in most kinesins. Consistent with this notion, removal of the flexibility which is mostly due to the presence of one or more glycine residues indeed relieves the auto-inhibition. A direct impact of this self-inhibitory mechanism on the stepping could so far not be demonstrated.

Among the members of the kinesin super family, the kinesin-2 motor resents a particularly intriguing case as it combines two different motor subunits into a heterodimer. It is argued that the heterodimeric kinesin-2 has co-evolved with the ciliary machinery to specifically function during the intraflagellar transport (IFT) as a heterotrimeric motor that is assembled with a third non-motor subunit. It is long-known that IFT takes place on cilia-specific axonemes that are formed by nine cylindrically arranged microtubule doublets A and B. Strikingly, IFT trains driven by oppositely directed kinesin-2 and dynein-2 motors were shown to move exclusively on the B and A tubules respectively. Together these findings provoke the question whether the kinesin-2 motor has been adapted to such specialized transport environment to ensure a 'collision-free' movement of IFT trains on the A and B tubules. However, mechanisms underlying these observations remained unknown.

Indeed, previous findings with the kinesin-2 motor already provided first clues that the two different head domains in the heterodimer are kinetically distinct. Like prototypical homodimeric kinesins, the heterodimeric kinesin-2 contains a conserved kink in its stalk and consequently displayed auto-inhibition in vitro. Unlike the homodimers, however, the inhibition of the heterodimeric motor was found to be asymmetric. While the wild-type kinesin-2 was switched off as judged from bulk ATPase assays, solely switching the relative positions of the head domains sufficed to activate the motor. The latter in-

dicated that the tail-mediated inhibition preferentially impacts one head domain and not the other within the heterodimeric motor. Yet, no direct evidence of such inhibition of the heads by the tail domain is so far available.

In this thesis, several open questions are adressed about the heterodimeric kinesin-2 stepping mechanism and its regulation. To this end, a fluorescence based super-resolution microscopy technique called FIONA (Fluorescence Imaging with One Nanometer Accuracy) was used. Towards a comprehensive description of kinesin-2 stepping, the dual-color FIONA (dcFIONA) technique is established to simultaneously track the two different heads of the heterodimeric kinesin-2 motor at nanometer resolution. For the first time, dcFIONA allowed the direct visualization of two different heads during kinesin stepping and exposed the distinct stepping behaviors of the two different head domains in the heterodimeric kinesin-2 motor. While one head displayed a single exponential dwell time distribution as expected, its partner head surprisingly displayed a double exponential distribution, suggesting a second rate-limiting step in the ATP-hydrolysis cycle. This feature was enhanced in the wild-type motor, remarkably however, was revoked when the relative positions of the head domains were switched. The latter demonstrates the asymmetry in the inhibition mechanism in the heterodimeric kinesin-2 motor as observed previously in bulk ATPase assays. By simultaneously tracking the two heads in the heterodimer using dcFIONA, it was thus possible to unmask the kinetic differences between the two head domains in the heterodimeric kinesin-2 and demonstrated for the first time the inhibitory influence of the tail on the catalytic head domains during processive stepping.

Lastly, to interrogate whether the kinesin-2 is specifically adapted to the axonemes during IFT in vivo, the stepping behavior of the heteromeric motor on microtubules and on axonemes was contrasted. Consistent with previous results from multi-motor experiments that showed a left-handed spiraling of the motors with a characteristic pitch, this visualized the left-handed spiraling of single motors on the microtubules. Strikingly, this spiraling was completely suppressed when the motor moved on axonemes suggesting that taking left-handed side steps eventually restricts the kinesin-2 to one side of the microtubule doublet. Such directed partitioning on the microtubule doublet would in fact provide a simple mechanism for the oppositely directed IFT trains to use the A and B tubules in an exclusive manner and ultimately get out of each other ways in vivo.

This thesis provides unprecedented insights into the stepping mechanism of heterodimeric kinesin-2 motors. On the long-run it will serve as a road map to unravel the intricacies of this essential motor and its interplay with other motors in the IFT machinery in even more detail. With the introduction of multi-color FIONA and specific labeling a whole field of questions in this field is now open to be answered.

Zusammenfassung

Molekulare Motoren sind für Transport über weite Strecken in Eukaryoten zuständig, der wegen den großen Entfernungen nicht durch Diffusion möglich ist. Kinesine sind Mikrotubuli-Motoren, die überall in der Zelle und in speziellen Zellausstülpungen (Zilien) aktiv sind. Der aktive Teil des Motors ist ein Dimer mit zwei 'Köpfen' am N-Terminus, einem 'Schaft' für die Dimerisierung und 'Enden' am C-Terminus die für die Bindung der Fracht zuständig sind. Zwei Zyklen für ATP-Hydrolisierung in den Köpfen sorgen für die Energieversorgung der Fortbewegung. Dies findet mit einem Mechanismus statt, der dem menschlichen Gang ähnelt. Dabei überholt der hintere Kopf immer den Vorderen in einem Prozess der 'hand-over-hand' genannt wird. Diese Schritte können durch einen Mechanismus beeinflusst werden, der Autoinhibierung heißt. Ein Knick im Schaft ermöglicht dazu eine Interaktion der Köpfe mit den Enden. Wenn der Schaft durch eine Mutation gestreckt wird, oder die Enden entfernt werden, ist die Inhibierung reduziert.

Kinesin-2 Motoren, von denen man denkt, dass sie mit Zilien co-evolviert sind, sind speziell unter den Kinesinen auf drei unterschiedliche Weisen. 1) Sie sind Heterodimere und verwenden zwei unterschiedliche Köpfe für das Laufen. 2) Ihr Mechanismus zur Autoinhibierung scheint asymmetrisch zu sein, mit der Notwendigkeit für eine spezifische Positionierung der Köpfe. 3) Wenn sie auf einem Mikrotubulus laufen, spiralisieren sie um die Längsachse. Wie beeinflussen diese speziellen Eigenschaften das Laufverhalten von heterodimeren Kinesin-2 Motoren? Hier habe ich mich an die Beantwortung dieser Frage mit Hilfe von Fluoreszenz basierter super-resolution Mikroskopie (FIONA) gemacht.

Für FIONA (Fluorescence Imaging with One Nanometer Accuracy) habe ich kinesin-2 Motoren an beiden Köpfen mit einem Fluoreszenzfarbstoff gefärbt. Mit einem speziell konstruierten Mikroskop kann man ein 2D Gaussprofil auf die brechungslimitierten Punkte von jedem Fluorophore anpassen, um die genaue Position des Farbstoffes bis auf einige Nanometer genau zu bestimmen. Wenn die Motoren durch Reduzierung der ATP Konzentration verlangsamt werden, können einzelne Positionswechsel der Köpfe aufgelöst werden. Indem ich die Heterodermizität der Kinesin-2 Motoren ausgenutzt habe, konnte ich die Köpfe verschieden färben und eine Farbe einer der Untereinheiten zuordnen. Das machte es zum ersten Mal für ein Kinesin möglich, die Schrittgrößen und Verweildauern für jeden Kopf einzeln aus den Daten zu gewinnen.

Hier zeige ich dass die unterschiedlichen Köpfe von KLP11/20 (*C. elegans*) unterschiedliches Schrittverhalten zeigen. Die Verweildauern von KLP11 zeigen eine Verteilung, die einem Doppelexponential gleichen. Dies lässt vermuten, dass ein zweiter Raten-limitierender Vorgang im ATP-Hydrolyse Zyklus des Kopfes stattfindet. Dieses Verhalten tritt verstärkt

auf bei einem nicht modifizierten 'wild-typ' Motor im Vergleich zu einer ee-Mutation die für einen gestreckteren Schaft sorgt. Es liegt daher nahe, dass die Autoinhibierung vor allem den KLP11 Kopf beeinflusst.

Basierend auf einem Modell das in unserem Labor entwickelt wurde, habe ich eine theoretische Beschreibung für das Schrittverhalten von untypischen Kinesin Motoren entwickelt. Mit der Einbeziehung von Seit- und Rückschritten konnte ich Daten für einen untypischen Kinesin-14 Motor nachvollziehen.

Die Evolution von Kinesin-2 Motoren ist stark mit dem Aufkommen von Zilien verbunden. Das heißt, dass sie vor allem auf dem speziellen Filament des Ziliums, dem Axonem, aktiv sind. Meine Daten zeigen, dass KLP11/20 und KLP3A/B (*X. Iaevis*) um Mikrotubuli spiralisieren, nicht aber um Axoneme. Zusammen mit ihrer Tendenz Schritte nach links zu machen, erklärt dass den Mechanismus der bereits gezeigten Separierung von Hin- und Rücktransport in Zilien.

Diese Arbeit klärt den Schrittmechanismus von Kinesin-2 Motoren in großem Detail auf. Dies war möglich durch die Einführung eines Experiments, dass beide Köpfe mit identifizierbaren Farben gleichzeitig verfolgt. Auf lange Sicht werden diese Ergebnisse helfen die Rolle von Kinesin-2 Motoren in vielen Ziliopathien zu klären.

Contents

Chapter 1

Introduction

1.1 Molecular motors

1.1.1 Logistics as a global challenge

In the globalized world, logistics is one of the overwhelming challenges we face. For a cellphone for example, the components will have traveled over $250\,000\,\mathrm{km}$ before it reaches the customer [1]. Parts of the device are manufactured all over the world, e.g. NFC controllers from the Netherlands, the accelerometer from Germany and the home button from a supply chain all over China. In the view of logistics, a eukaryotic cell resembles a globalized world in a miniaturized form. Various different cargoes have to be transported through the whole cell in order for this highly complex system to work. Proteins for example are mostly produced centrally and then distributed to their vast amount of sites of employment all over the cell by an active transport system.

A look at the final stretch of the phone's journey over the world shows the complexity of the necessary logistics. After final assembly and testing in China, the phone is transported by a combination of trucks, trains, airplanes and ships to the city of its customer. If the customer is of the old school, he will go to a store and pick up one of the devices, for example by bike. After all, a journey employing many different means of transport, that use vastly different infrastructures. Again, not too different from the final journey of a produced protein in a cell on its way to its operation site.

Considering a tubulin that is destined to form part of an axoneme inside a cilium, the tubulin has to travel from the place of translation to the cell periphery and into the specialized compartment of the cilium. The logistics for this are provided by molecular mo-

tors together with the cytoskeleton. The first long stretch of this journey is, comparable to the airfreight of the phone, performed by a kinesin motor that walks on a microtubule leading close to the cell periphery [2]. After being targeted to the base of the cilium, maybe mediated by a myosin (the train to the city), it is transported to the ciliary tip by a complex system (the customer and his bike) called intraflagellar transport (IFT) machinery [3, 4]. It will be incorporated there into the axoneme supporting ciliary function.

Just as the customer wants his phone shortly after placing the order, cellular transport has to be timed and organized well, in order to deliver the cargo efficiently and effectively. An estimated 50 to 100 different molecular motors are at work to organize the dynamic life in a eukaryotic cell. Comparative genetic analyses and functional data suggest that five motor families are universally responsible for cargo transport throughout the eukaryotic phyla: the microtubule-associated kinesin-1, kinesin-2, KIF1, dynein, and the actin-associated myosin V [3]. For IFT for example it is known that the lack of one of the components, a kinesin-2 motor, induces polycystic kidney disease [5]. As a bike is human-built, we know how it works and are able to repair it, to a certain stage. Molecular motors and their regulation are however, in many ways, still a mystery that nature has constructed for us. This work therefore aims to extend the understanding of one of the gears that drives IFT, heterodimeric kinesin-2 motors that contribute to the transport of cargo from the base of a cilium to its tip.

1.1.2 Kinesin motors

Kinesin motors are active in many different settings, from transport in neurons and melanosome transport in the cytoplasm to the highly specialized function in cilia. Different kinesin families are therefore employed in cells, with the main subject of study to date being the 'prototypical' kinesin-1. The main part of a typical kinesin motor are two dimerized proteins, with catalytic heads at the n-terminal, followed by the coiled-coil domain for dimerization called 'stalk' and the c-terminal 'tails' (Figure 1.1). The heads bind to the trail, while the tails, typically in cooperation with adapter proteins, are responsible for cargo attachment.
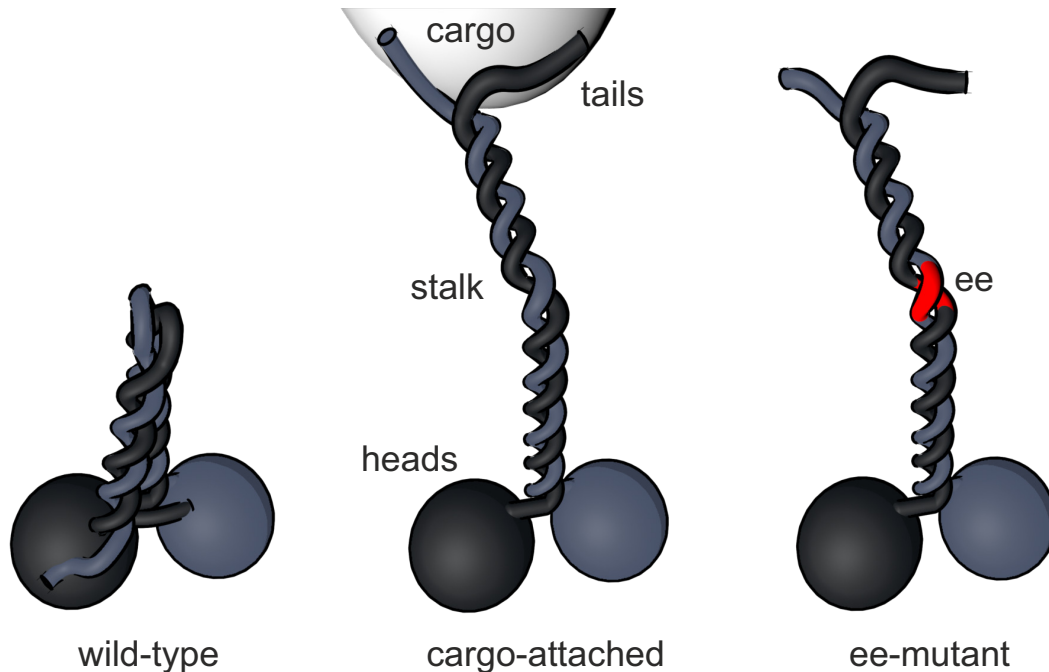
Figure 1.1: Depiction of the different states of a kinesin motor.
Kinesin motors are comprised of two subunits that dimerize to form the motor. The n-terminal domains are called heads and are responsible for ATP hydrolysis and locomotion as well as the binding to the microtubule. The middle domains form the stalk by dimerization to a coiled-coil structure. The c-terminal 'tail' domains are responsible for the cargo-binding and are part of the auto-inhibition mechanism that controls the motor activity. In the wild-type, a kink in the stalk allows it to fold and bring the tails in proximity to the heads (left panel). This allows for an interaction of the tails with the heads that leads to auto-inhibition. In nature, this regulation is relieved by the binding of a cargo to the tails (middle panel). For experimental purposes, a mutation called ee-mutant is often used, that stiffens the stalk region and thus impedes its folding and the interaction of heads and tails (right panel).

Kinesin walking mechanism

Coordinated ATP-hydrolysis cycles in the heads deliver the energy for movement. For walking, the trailing head of the motor takes a step in front of the other, a mechanism called 'hand-over-hand walking' that is very similar to the human gait [6, 7]. As track, the motor uses a filament called microtubule (MT), a tube constructed of typically 13 protofilaments of tubulin dimers. Most kinesin motors are plus-end directed motors that walk towards the fast growing ends of microtubules. Each tubulin dimer is in size ~8 nm along the MT axis and provides one binding site for the motors' heads (Figure 1.6). This leads to a step size of 16 nm for each displacement of one head on the same protofila-

ment. This mechanism also provides the framework for a property of many dimeric motors called processivity. It describes the motors capability to move for several micrometers during each interaction with a microtubule. As dimeric motors are often used for long-range transport in the cell, this is one of the defining parameters molecular motors are described by. The binding affinity of the head to the filament depends on the nucleotide state of the ATP-hydrolysis cycle in the head. These cycles in the head are offset temporally, so that one head is always in the tightly bound state. This ensures that at least one head always remains bound to the filament [8, 9]. Kinesin-1 employs this mechanism to achieve run-length of $1\,\mu m$ and speeds of $1\,\mu m\,s^{-1}$ [10]. If walking against a hindering load, kinesin-1 can achieve forces of $6\,pN$ and hold those for a extended time.

Kinesin auto-inhibition

Kinesins have to be localized and directed in the cell in order to optimally fulfill their function. This is achieved in vivo by modulating their activity (number of filament interactions), speed, run-length and their affinity to different cargoes. The mechanisms of this regulations are unknown for most settings [11]. One mechanism that is studied fairly well is the so-called auto-inhibition, mainly thought of as a mechanism that prevents futile ATP-hydrolysis when the motor is not bound to a cargo and important for localization of the motor within the cell [12]. A kink in the stalk of the motor enables the tails to fold back to the heads [13, 14]. The interaction of the tail-region with the heads leads to a regulation of the ATP-hydrolysis and is able to impede binding to the microtubule. Biochemical work first demonstrated that one of the C-terminal distal tails is involved in the suppression of the ATPase in the dimeric motor [15]. Subsequently, a crystal structure of the dimeric head domains of the motor with the inhibitory tail visualized this 'half-site-inhibition' model at atomic resolution [16] (Figure 1.2).
In many motors, the auto-inhibition can be abrogated by a mutation in the kink-region that leads to a stretched stalk which in turn counters the head-tail interaction (Figure 1.1 & 2.6). More relevant for the regulation in cells is the release by the competitive binding of a cargo to the tails [11] or a modulation of the affinity of the tails for the heads by phosphorylation [17, 18]. Auto-inhibition has been studied mainly by comparing the ATP ase activities of modified, truncated or mutated versions of the respective motor. It was possible to show that auto-inhibition is not always an on/off mechanism by comparison of the speeds of wild-type (inhibited) versus modified (non-inhibited) versions of some motors [11, 19]. The interaction of the tails with the heads has been studied in great de-

kinesin-1   kinesin-2
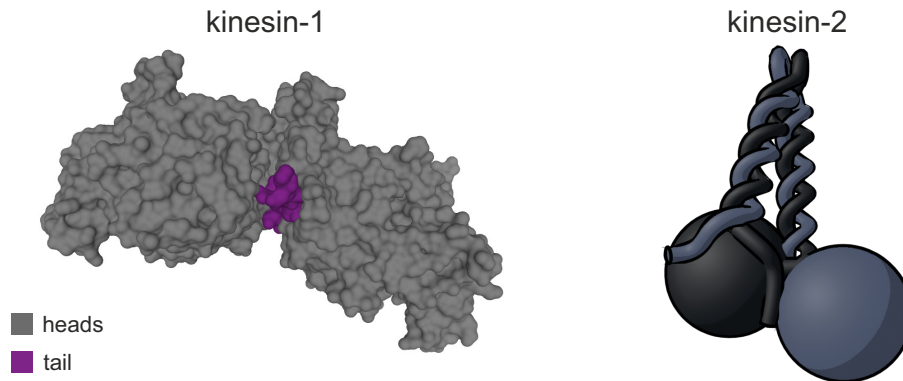
■ heads
■ tail

Figure 1.2: A crystal structure of kinesin-1 head domains shows a kinesin-tail bound in between the heads.
A crystal structure of a kinesin head and tail complex shows, that one tail binds between the two heads locking them together. In the heterodimeric kinesin-2, two different tails are present at the heads in the wild-type folded conformation. For an asymmetric inhibition mechanism, one of the tails would interact with the heads preferably. Adopted from [16].

tail using crystallography and cryoEM approaches as mentioned above. These studies showed the binding of the tail to the heads and proposed different ways this interaction can influence the walking ability of the motor. The two main models are a restriction by physically 'crosslinking' the head domains to suppress mobility and an influence on the ATP-hydrolysis cycle, the ADP release time more specifically [20–23].

1.1.3 Kinesin-2 motors

One of the essential toolbox motors, kinesin-2, is mainly associated with IFT in cilia. There, it is essential for the build-up and maintenance of these important structures, making it an interesting subject of study. Interestingly, many kinesin-2 motors are comprised of two distinct subunits, forming a heterodimeric motor. Why this is the case and how it influences the motor's function is not known in detail. The C-terminus of the heterodimeric motor further associates with a non-motor subunit, termed Kinesin Associated Protein (KAP) that in turn links the motor to its cargo in vivo [24, 25].
Kinesin-2 motors tend to show different properties than kinesin-1. Early experiments on the motors suggested a curtailed run-length at ~0.5 μm [26, 27] and slower speeds at ~0.5 μm s^{-1} [24]. We and others have meanwhile been able to show that under the right conditions, kinesin-2 can achieve similar or even longer run-lengths than kinesin-1 [28, 29]. Unpublished data in our lab now also suggest that some heterodimeric kinesin-2 mo-

tors can also show velocities that exceed the usually reported velocity for kinesin-1 at $1\,\mu m\,s^{-1}$. We were also able to measure the force generation properties of these motors. The data showed, that the motor can produce force close to that of kinesin-1 (~6 pN), but is not able to hold these forces for a long time, e.g. does not stall at these forces but falls off the track [26]. These special properties of kinesin-2 motors are summarized nicely by the kinesin-2 pioneer Jon Scholey in [30]. We were previously able to show that heterodimeric kinesin-2 motors use the 'hand-over-hand' mechanism for walking as does kinesin-1 [31]. The differences in the movement parameters therefore have to originate from the detailed implementation of this mechanism in the respective motor.

An intriguing property of heterodimeric kinesin-2 motors is that they spiral around the filament if walking on a microtubule. This behavior was known for non-processive or artificial kinesin motors for some time, for processive motors however, our lab showed this in 2012 for the first time [32, 33]. It was also possible to link this behavior to the length of the neck-linker region joining the heads of the motors to the stalk. Even for the normally protofilament-tracking kinesin-1, a torque generation could be introduced by elongating the wild-type neck-linker by mutation. The fact that all of the processive motors show a torque generation to the 'left' implies a distinct function for this behavior. A similar but not directed behavior has since been shown also for dynein motors [34]. There are different theories as to why the motors show this behavior, that are all heavily based on assumptions. The most prominent one is the avoidance of roadblocks, e.g. microtubule associated proteins on the motors protofilament [35]. However, admittedly at different efficiencies, this behavior has also been shown for kinesin-1 [36]. A more important function of this consistent torque generation to the left might therefore exist. This work suggests another function of the spiraling that is linked to its important function in IFT in cilia. The mechanism can explain the organization of IFT in the very tight space of the cilium by an interplay of the motors walking mechanism and the special properties of the central filament in cilia called axoneme.

It is known, that different kinesins show different transport parameters. It has therefore been discussed, why two different subunits have been combined in the heteromeric kinesin-2 motors. One of the main discussions has evolved around a limp in the motor, e.g. a difference in the stepping times between the heads [18, 33, 37–42]. These studies have been mainly performed on optical tweezers, following the steps of single motors bound to micron sized glass beads. As steps from the heads cannot be attributed to one specific subunit in this case, recorded runs must be rather long in order to get enough

```
A7LGV1|fla8_cr    LDAEQIRAEKEALAKKLKAMESKILKGDQA-GGLAEVTKKKEEELKRKEQELERRRKEEE 567
P46869|fla10_cr   GAIEKEKQEKAVLESRIKEMEGKIVVGGVN---MLEKVDELKQKSEDIKREAAIRKRQEE 577
Q965T6|KLP20_ce   AELKKARSEHEKLRSKLEKIEKKLIVGGEN---LLEKVEEQAKLLEVNNKELEQSKFQEA 506
P28741|KIF3A_mm   KDLLKAQQEHQSLLEKLSALEKKVIVGGVD---LLAKAEEQEKLLEESNMELEERRRRAE 546
Q98TI1|kif3a_xl   KDLFKAQQEHQSLLEKLSALEKKVIVGGVD---LLAKAEEQEKLLDESNFELEERRKRAE 544
Q19633|KLP11_ce   DLLEKERIEQARVAERIANIQSRLIVGSEEDGRLESRTKEQHAQLEKKRRELAEQKRRER 516
Q61771|KIF3B_mm   EDLRREKDAAEMLGAKIKAMESKLLVGGKN---IVDHTNEQQKILEQKRQEIAEQKRRER 539
O93478|kif3b_xl   DDLKKEREAMEMLNSKVKAMESKLLVGGKN---IVDHTNEQQKILEQKRHEIAEQKCRER 539
                       : :       :  ::  ::  ::: *.     :    ..:     .  . *    :  .
```

Figure 1.3: An alignment of kinesin-2 sequences from different organisms shows the universality of the kink.
The kink position with residues that have a low tendency to build a coiled coil in the stalk of different kinesin-2 motors is well preserved between organisms. This shows the functional importance of the ability of the tail to fold back to the heads in these motors. The alignment was performed using Clustal Omega [45]. IDs are from UniProt [46] (cr - *c. reinhardtii*, ce - *c. elegans*, mm - *m. musculus*, xl - *x. laevis*).

statistics to assign the fast/slow head correctly. This sets a limit to the minimum limping factor that is detectable within the run-length of a motor when bound to the bead [38]. For this reason, a limp could not be detected even for heterodimeric motors [33], or it had to be enforced using hydrolysis-related mutations [40, 43]. Due to the asymmetric walking symmetry of kinesin, a limp could also be introduced by the application of a hindering load, also realized in combination with different mutations to the heads and stalks of the motors [41, 44]. A combination of ATPase assays and theoretical description of the stepping first opposed a limp in the mammalian KIF3A/C in 2016 [42], but more recent data suggested that a limping factor might actually be present [39]. Overall, all attempts to artificially introduce a limp into a motor cast doubt on the physiological relevancy of the conclusions of the regarding study. It is interesting that a limp can be enforced, but to be relevant, it would have to be shown directly in a minimally modified motor in a close to physiological setting. In order to achieve this, the steps for both heads have been observed individually and concurrently in this work. The results show a difference in the stepping behavior as supposed previously with some interesting details.

The available sequence information on the kinesin-2 motors reveals the strictly conserved "kink" region containing glycine residues in the middle of the stalk domain (Figure 1.3). Our previous work demonstrated that the replacement of these flexible glycine with glutamate residues relieves the auto-inhibition in the heterodimeric KLP11/20 kinesin-2 from *C. elegans*. The functional significance of auto-regulation has also been highlighted by the data obtained from KLP11/20 kinesin's in vivo partner OSM3 which is a homod-

imeric member of the kinesin-2 subfamily. As it is the case with KLP11/20, the OSM3 is
an auto-regulated motor and the auto-regulation is mediated by the kink position (glycine)
situated in the middle of its stalk. The replacement of the flexible glycine at the kink
with a glutamate renders the motor constitutively active in in vitro assays and this same
point mutation fails to build channel-type cilia in vivo [47, 48]. These results collectively
suggest that the auto-regulated state of ciliary kinesins is essential for their in vivo func-
tion. A special situation arises from the presence of two different heads and tails. Studies
from our lab have hinted to an asymmetric inhibition mechanism for kinesin-2 motors
[26, 49]. The inhibition could be relieved solely by switching the positions of the heads in
the heterodimer, showing the necessity for a correct setup of the head-to-tail interaction.
The inhibition is asymmetric, does this also mean, that one of the heads is influenced
more or even only by the interaction with the tail? The data presented here strongly sup-
ports the asymmetric inhibition model and shows different ways this interaction can be
tuned.

1.1.4 Intraflagellar transport

The appearance of kinesin-2 motors during evolution is thought to be linked to the emer-
gence of cilia, which suggests a specialization for intraflagellar transport [3, 4, 50–52].
Kinesin-2 has since been readopted for cytoplasmic transport, for example on melanosomes
in *X. leavis*. Still, without kinesin-2 motors there would be no cilia and vice versa. Cilia
are found on almost all eukaryotes and are especially abundant in mammalian cells. They
are organelles with a rod-like shape that extend outside the cell and is covered by a spe-
cial membrane. Motile and immotile cilia serve a wide variety of purposes from motility
of the cell and transport of fluid in the brain to the sensing of extracellular signals like
photons (photoreceptor sensory cilia) or pressures (hair-cells in the ear) [53–55]. A loss
of function in cilia is linked to diseases called ciliopathies that span the whole field from
deafness to polycystic kidney disease (PKD) [56]. For hearing, the mechanical function
of the cilium on the hair-cells is hampered. For PKD in turn, a dysregulation of intra-
cellular signaling pathways, where the cilia act as 'antennae', is assumed as cause for the
disease [57]. Irregularities in the function of kinesin-2 motors have been shown to cause
cilium dysfunction and have therefore been associated directly with polycystic kidney dis-
ease in mice [5]. In *c. elegans*, cilia are responsible for chemical sensing of the environ-
ment.
IFT is responsible for the delivery of ciliary components for the build-up and mainte-

nance of their structure and is realized differently in different species. In *C. elegans*, the organism this thesis will mainly focus on, anterograde transport to the tip of the cilium is realized by two kinesin-2 motors in cooperation (Figure 1.4). KLP11/20 and OSM3 work together to transport the IFT particles from the base of the cilium to its tip. The cargo is compiled of repeating subunits that form long trains, these in turn are compiled of many different proteins, including membrane proteins, cargo adapters and axonemal components [58]. Recently, we could show that at least one of these components is also able to fully activate the OSM3 activity [11]. Multiple motors are attached to these trains at the same time and coordinate their movement for efficient transport [59]. The retrograde transport is realized by a dynein-2 motor, that is also specialized for IFT [60, 61]. This motor is a cargo on the anterograde transport, while the kinesin motors become cargoes on the retrograde transport.
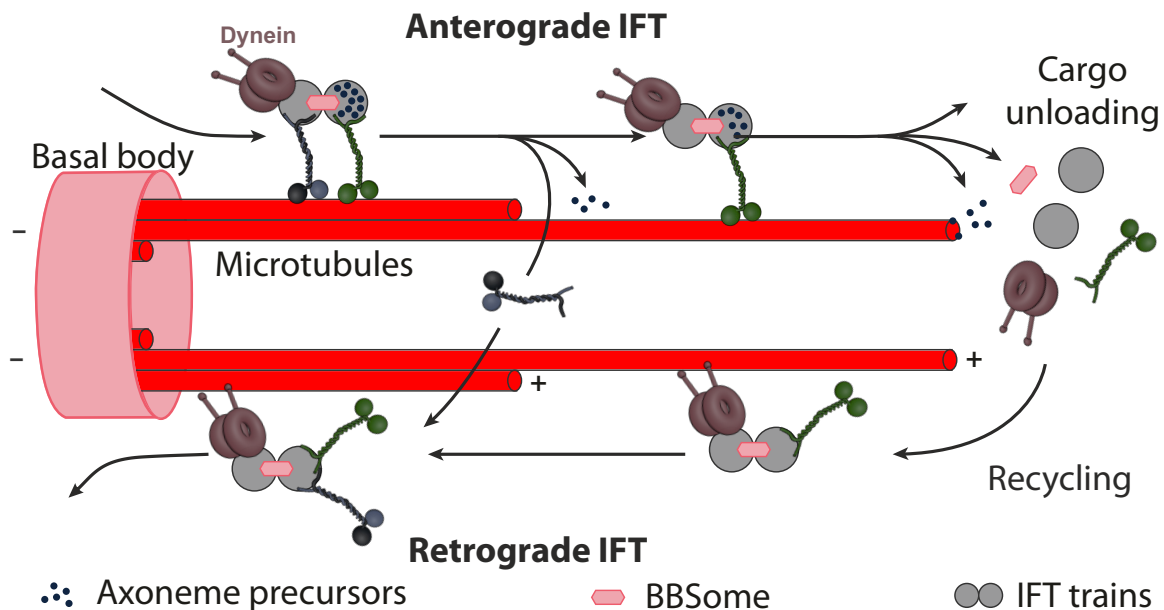
Figure 1.4: Depiction of intraflagellar transport in *C. elegans* adjusted from [30]. IFT trains containing different cargoes (only axoneme precursors depicted here) are transported to the tip by a combination of KLP11/20 and OSM3 motors. The dynein is part of the cargo and deactivated for the anterograde transport. The KLP11/20 and part of the cargo are decoupled from the trains at the ends of the doublets. After transport by OSM3 alone on singlet microtubules to the tip, the trains are remodeled. The core IFT particles form new trains with the dynein now activated as transporter and the kinesin motors as cargoes. Exactly how the trains enter and leave the cilium at the basal body is not known, just as the details of the remodeling process at the tip.

1.2   *C. elegans* as an IFT model

The remarkably diverse sensory cilia in *C. elegans* are clustered within the primary chemosensory organ (Figure 1.5). Although such morphological diversity among cilia occurs throughout eukaryotic phyla, we lack a molecular understanding of how such phenotypic variation is generated using the universally conserved IFT machinery. Recent insights gained from comparative studies in *C. elegans* have begun to shed light on how this might be accomplished via the regulated deployment of kinesin-2 motors.
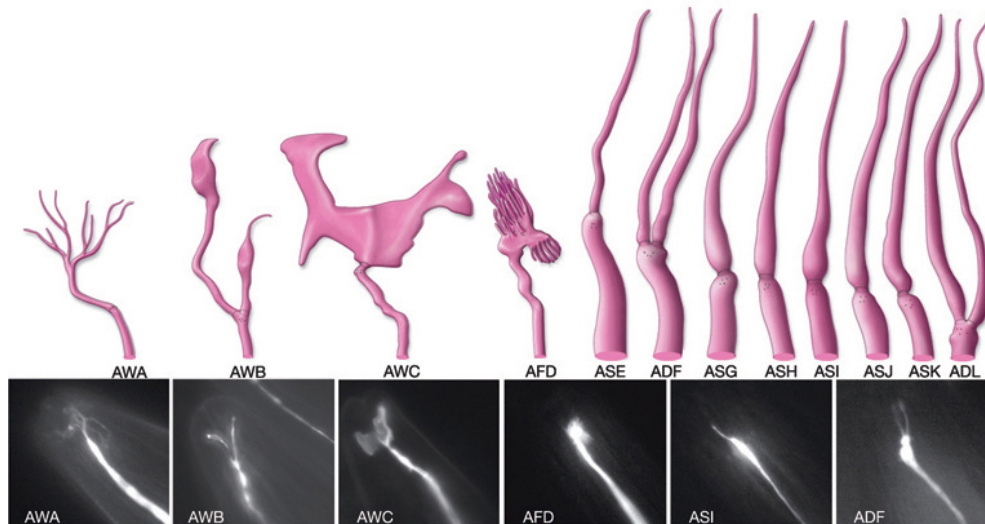
Figure 1.5: Different types of amphid cilia in C. elegans (from [62]).

Studies from the Scholey group have elucidated the functional cooperation of the KLP11/20 and the OSM3 motors to build the so-called 'canonical' rod-shaped cilia such as ASI or ASH [48, 63]. In these cilia, both motors cooperate to build the middle segment of the axoneme consisting of doublet microtubules. At the demarcation site, where the doublet microtubules end and the distal segment of singlet microtubules starts, the KLP11/20-dependent movement is terminated (Figure 1.4). Importantly, OSM3 can compensate for the loss of the KLP11/20 motor and build the middle segment on its own [48, 63]. KLP11/20 however cannot compensate for the loss of OSM3 and the distal segment of the cilia is not built. In this case, the animals are incapable of sensing osmotic pressure variations within their environment. The division of labor between the kinesin-2 motors is different in the wing-shaped cilia, such as the AWB or the AWC cilium (Figure 1.5). In these cells, either KLP11/20 or OSM3 can build both the middle and distal segments. In contrast to the rod-shaped cilia, where the loss of OSM3 invariably leads to deficient os-

motic avoidance, in AWC cilia it is the loss of the KLP11/20 motor that causes a defect in chemotaxis. Taken together, these results suggest that interfering with regulated motor coordination and transport velocities leads to severe defects in the sensory cilia function and structure [64–66].

1.3 Microtubules and Axonemes

Microtubules are tubular filaments with an outer diameter of 25 nm comprised of dimeric subunits of α- and β-tubulin. These subunits form elongated structures with a repetition every 8 nm called protofilaments. Typically 13 of these protofilaments then combine laterally to the tube-shaped structure of the microtubule, generating a lattice with 4 nm spacing in this direction. Additionally, the protofilaments are offset by 1 nm, introducing a twist into the microtubule lattice. At the position where the first and 13th protofilaments meet, this leads to the presence of the so called seam, an irregularity in the microtubule lattice where the offset between the protofilaments is different [67]. While the 13-protofilament microtubules are the most prominent in vivo, microtubules with different numbers of protofilaments can be found in nature and when polymerized under different conditions.

The specialization of kinesin-2 motors to cilia implies, that they are mainly active on the special filament of the cilium, the so called axoneme. Microtubules are modified here to build doublets by fusing an A-tubule to a B-tubule. Nine of these doublets form a ring that is connected by flagellar dyneins and nexins (Figure 1.6 and [68]). In *C. elegans* the final micrometers of the cilium contain just singlet microtubules, a speciality for this organism. The emergence of the special superstructure of axonemes seems to have different reasons. It has to supply the mechanical structure for the cilium outside of the cell. Additionally, active cilia fulfill beating motions by sliding the doublets against each other using dynein motors. The axonemal superstructure is thought to assists the regulation of this mechanism [69]. The configuration of the microtubules as doublets is discussed to be due to the mechanical stability needed in the axoneme [70, 71]. However, it also has properties that seem to be important for intraflagellar transport.

As mentioned above, after having coevolved with cilia, kinesin-2 motors have been readopted for transport also in the cytoplasm. This means that they have to be able to function on very different filaments that span a wide range of complexity and organization. The tubular microtubule essentially has a rotational symmetry along it's filament axis.
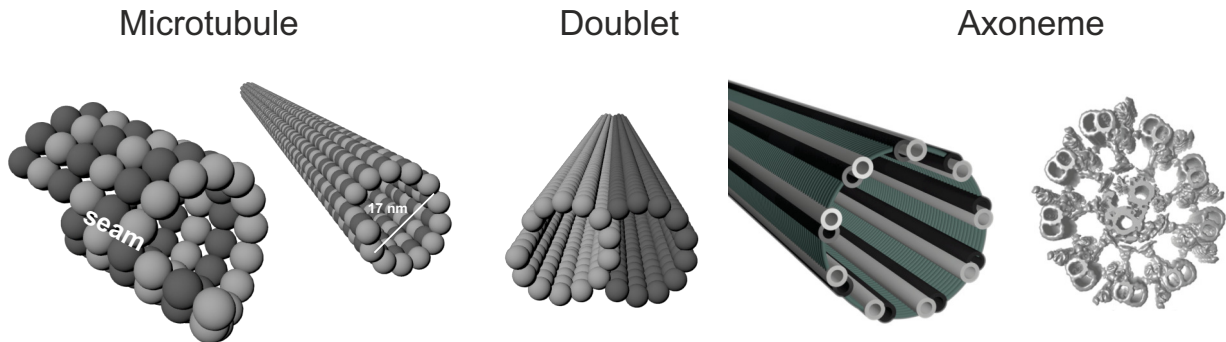
Figure 1.6: Structures increase in complexity from the microtubule to the axoneme [72].

This symmetry is broken in the doublet and especially considering its integration in the axoneme superstructure (Figure 1.6). This fact makes a recent discovery even more interesting; the anterograde transport is restricted to the B-tubule, while retrograde IFT-trains travel on the A-tubule only. Furthermore, both directions of transport occur on the same filament as shown in *C. reinhardtii* [73]. This was studied using a combination of fluorescence microscopy (to assign the direction of the train) and cryoEM (to determine the exact position of the train relative to the MT doublet). This setup allows for effective two-way traffic in the confined space between the axoneme and the membrane of the cilium. How this separation is achieved however, could not be determined yet.

1.4 Fluorescence imaging with one nanometer accuracy (FIONA)

1.4.1 A quick history of fluorescence microscopy

There are two main factors that make a microscope image a good one, resolution and contrast. Especially for biological samples, contrast often was and is the limiting factor for microscopy. The similar optical properties of biological material led to the development of techniques optimized for biological samples like polarized light microscopy and differential interference contrast (DIC). Just as any motor, molecular motors do have benchmark parameters that are characteristic for their function inside the cell. Microscopes have played a crucial role in elucidating these properties over the last decades. The first gliding assays, where a filament glides on a carpet of motors, were performed by

Ronald Vale on a DIC microscope in 1985 [74, 75]. The microtubule with its diameter of 25 nm can still be resolved by this technique at low enough concentrations. This allowed for a measurement of the speeds of motors.
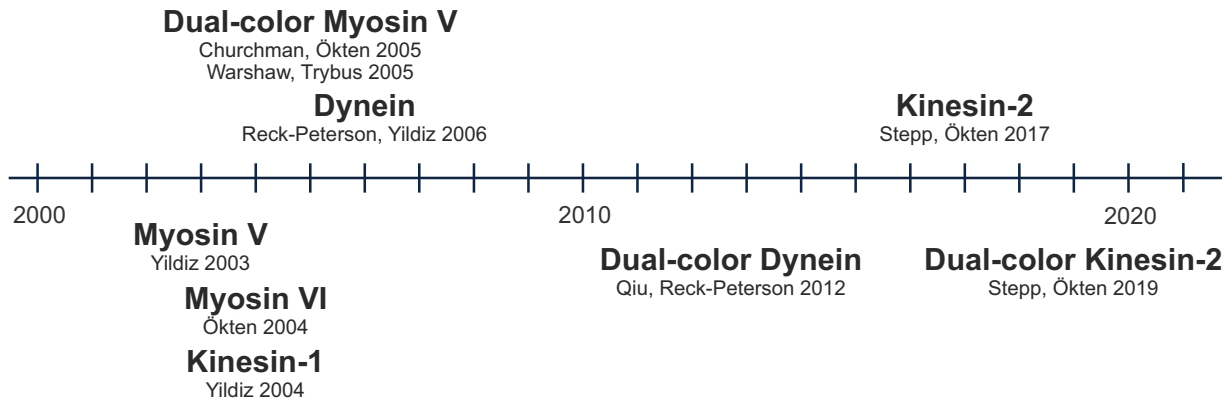
However, these techniques rely on a difference in optical properties in the sample. The real breakthrough therefore was the discovery of a possible black/white contrast agent, fluorescent probes. Light at a short wavelength stimulates the emission of light at longer wavelength in the so-called fluorophore. Due to the difference in wavelengths, the emitted light can be separated from the excitation light, which leads to a theoretically perfect bright/dark contrast at the fluorophore positions. The application to biological samples was boosted with the discovery of the green fluorescent protein, a feat that Shimomura, Chalfie and Tsien were awarded the Nobel Prize in Chemistry for in 2008. This allowed the imaging of single motors, that do not have enough contrast to be imaged by conventional microscopes if not attached to a bead or something similar. Labeled with a fluorescent probe however, single motors can be followed over an extended time walking on a filament. These experiments on single molecules have been pioneered by Funatsu et al. in 1995 for myosin and later in 1996 together with Ronald Vale for kinesin [76, 77]. The special illumination technique TIRF was used here in order to enhance the signal to noise ratio of the data [78]. By generation of an evanescent wave at the cover-slip/sample interface through total internal reflection, the excitation volume is limited to a depth of ~200 nm depending on the angle of incident. The filaments are bound to the cover-slip and only fluorescence from the motors bound to a filament will be observed, thus reducing the background fluorescence in the signal significantly. This makes it possible to follow single motors walking on the filament and hence to determine their single-motor speeds and run-lengths. Today, out of convenience, also the filament gliding experiments are performed using fluorescently labeled microtubules on fluorescence based microscopes.

1.4.2   The emergence of super-resolution techniques

The Nobel Prize in Chemistry in 2014 for the development of super-resolved fluorescence microscopy to Betzig, Hell and Moerner was an acknowledgment to an ongoing movement in microscopy. The advantages of fluorescent probes were now also used to push limits of resolution after the big impact they had on contrast in imaging. The resolution of a classic microscope is limited by the diffraction limit founded in the necessity of optics for imaging. This meant for a long time, that imaging of biological samples required a trade off. Imaging by electron microscopy would yield high resolution images (sub nm),

Dual-color Myosin V
Churchman, Ökten 2005
Warshaw, Trybus 2005

Dynein
Reck-Peterson, Yildiz 2006

Kinesin-2
Stepp, Ökten 2017

2000   2010   2020

Myosin V
Yildiz 2003

Dual-color Dynein
Qiu, Reck-Peterson 2012

Dual-color Kinesin-2
Stepp, Ökten 2019

Myosin VI
Ökten 2004

Kinesin-1
Yildiz 2004

Figure 1.7: Timeline of the application of FIONA techniques to molecular motors.

but it required the immobilization and staining the sample. Fluorescence microscopy was possible on a live sample, but was limited to ~200 nm resolution. Today, different techniques allow to 'break' the diffraction limit using fluorescence microscopy with a twist. The wide-field techniques in super-resolution all use the same principle to break the resolution barrier. By calculating the original position of a fluorophore from the peak it generates on a camera chip, the resolution can be pushed to the nanometer range. The best accuracy for this is achieved by fitting a 2D gaussian profile to the obtained peak. In order to do this, peaks from single molecules have to be separated enough to be able to analyze each one individually. Different techniques mainly vary in how they achieve this separation. From PALM (Photoactivated Localization Microscopy), that activates only a subset of molecules, to GSDM (Ground State Depletion Microscopy), where molecules are temporally bleached, many flavors exist as of today. The simplest way to achieve separation is to dilute the fluorophores enough in the sample to obtain single peaks. This is the typical approach also for molecular motors.

1.4.3 Super-resolution techniques for mobile specimens and the application to molecular motors

Super-resolution based on fluorescent techniques has evolved to be an everyday application. However, most implementations are tailored to immobile or quasi static specimens. The challenge with mobile specimens is the inherent limit to the available recording time before the object of interest re-positions. This also maximizes the demands to the experimental setup on many levels. Starting from an optimal photon efficiency of the

microscope to perfect performance of the applied fluorophores. Because of this, super-resolution techniques are a juggle between exposure time, mobility of the sample and the need for modification of the specimen.

Speeds and run-lengths are long-range properties that could be obtained using 'standard' fluorescence microscopy. However, it is necessary to learn more about the dynamics of a motor at the molecular level in order to study the mechanisms involved. Very accurate measurements of molecular motor activity have been possible using optical tweezers for a long time. But, this always implied the attachment to micron-sized beads and thus changing the behavior of the motor significantly. Using a fluorescence super-resolution technique called FIONA (Fluorescence Imaging with One Nanometer Accuracy), Ahmet Yildiz et al were able to resolve single steps on a minimally modified myosin-V in 2003 [6]. The myosin was labeled with a quantum dot at one head and slowed down by reducing the ATP-concentration. A similar achievement could be announced by Zeynep Ökten for a myosin-VI in 2004 [79]. While these steps with 74 nm were still rather close to the classical resolution limit, Yildiz et al followed just one year later with the recording of 16 nm steps of a kinesin-1 [7].

These studies were able to resolve the question about the basic walking mechanism of molecular motors to be the aforementioned 'hand-over-hand' mechanism for kinesins and myosins. This was possible by showing, that the step size was two times the distance of binding sites on the filaments and by the observation of the heads dwell-times. The double exponential distribution of dwell-times was interpreted as the convolution of the inherent dwell time of the observed head combined with the step of the second non-observed head. This also shows the intricate coordination of the two heads for alternating stepping at a molecular level, an important feature of the 'hand-over-hand' mechanism. For dyneins, the data showing a mechanism termed 'alternating shuffling' was published in 2006 by a team again including A. Yildiz [80]. Interestingly, this mechanism relies less on the direct coordination of the ATP-cycles and more on long duty-times of the catalytical units to achieve processivity. This study also extended the analysis of the stepping to a two-dimensional approach. While pure distances where measured before, the team now also observed the direction of steps (parallel/perpendicular to the filament axis). In 2005, Warshaw, Trybus et al. used two different quantum dots, to label a myosin-V motor with different colors at the heads [81]. Following both heads at the same time confirmed the alternating stepping behavior of the heads.

Recently, another super-resolution technique has been pushed mainly by the groups of

Philipp Kukura and William Hancock. Nanoscale scattering probes are attached to the motor in order to be able to use iSCAT microscopy. Good contrast and high frame rates enabled this technique to observe the stepping of myosin-V at saturating ATP-concentrations [82]. Even the occurrence of a substep could be observed between the two binding sites for kinesin [83]. While this technique pushed the limits for molecular motor imaging in the time domain, it is unfortunately limited to only one probe per motor, as the signals from two scattering probes cannot be separated.

A new technique called MINFLUX, developed in the lab of Stefan Hell, might be able to tackle all limitations mentioned so far. A doughnut-shaped excitation beam is used here to determine the position of a fluorophore with high precision using triangulation. The fluorescent signal is measured for three positions of the excitation beam and with the knowledge of the excitation shape, this data allows to determine the position of the fluorophore with very high precision. Ideally, the fluorophore is close to the center of the doughnut, where it is excited by low doses of light, minimizing photo damage and thus prolonging imaging times. Compared to the classic fitting of PSFs, the fitting procedure for triangulation is much more accurate for low photon numbers. Thus, MINFLUX can be very fast and easily be performed in multiple colors [84]. As commercial systems implementing this technique are just becoming available, it might be about to start its triumphal march in the labs around the world.

Super-resolution techniques have pushed the molecular motor field in recent years. The motors' inherent mobile nature however repeatedly reveals the limits of these techniques. Unlike PALM and STORM, FIONA and iSCAT therefore have not become 'standard' techniques used in many labs or publications. This also comes down to the necessity for specialized microscope hardware in order to obtain satisfying results.

1.5 Aims of this thesis

After the application to elucidate the basic stepping mechanisms of molecular motors, FIONA techniques have mostly lied idle. It is clear however, that there is a great chance to uncover a lot of interesting details about motor stepping using this technique. As detailed above, kinesin-2 is an essential motor for many functions in the cells and has some unique properties that also influence their functions. A custom-built FIONA microscope setup was therefore built and specifically optimized for the assays necessary to unveil unprecedented detail of kinesin-2 stepping mechanisms. This work describes the theoretical

background of this optimization and the design decisions for its practical implementation. How does the asymmetry in heterodimeric kinesin-2 influence its stepping? As FIONA is capable of observing motor steps with minimal influence on the motor, it is well suited to approach this issue. Due to the heterodimeric nature of kinesin-2 and the application of fluorescent probes, it is possible to label each head differently by assigning a color to each subunit individually. The steps of both heads can be observed on the same motor concurrently which allows investigation of the stepping behavior at an unprecedented level of detail. How does the stepping behavior of the two heads differ? And how does the asymmetric auto-inhibition mechanism influence this behavior? With dual-color FIONA data it was possible to show that the KLP20 has a different stepping behavior form KLP11 in the time domain. Also, the stronger auto-inhibition in the wild-type motor shows an effect predominantly on the KLP20 dwell times, strongly supporting the model of asymmetric auto-inhibition.

It is known, that kinesin-2 differs in its stepping behavior from the prototypical kinesin-1. But how is non-canonical stepping reflected in the FIONA data for a motor? Switching of protofilaments, backsteps etc. all have an influence on the data obtained from step detection experiments. How differences in the stepping pattern translate to features in the stepping data was studied by modeling the experimental situation. The goal was the simulation of a processive motor on a microtubule surface, with all the stepping parameters accessible for modification. The algorithm also includes events that are special for the non-canonical stepping of kinesin-2 motors and the like. On the example of data from a kinesin-14, generously provided by Allison Gicking, the algorithm is shown to be viable for recuperating the various features of the motors step size histograms from parameters that define the properties of single steps.

How has the kinesin-2 been optimized for its main role in cells for IFT? Beyond the mentioned heterodimericity, the main difference to kinesin-1 is its employment of the cilia-specific axoneme filament. Using FIONA techniques, it is possible to study the exact behavior of kinesin motors when walking on axonemes versus microtubules. The specialization to the track is best studied by comparing results on both filaments. Indeed, the step sizes and traces of the motors show that kinesin-2 is specifically optimized for transport on the axoneme. Combined with the knowledge about traffic separation and the missing symmetry in the filament, this work can explain how the organization of IFT is achieved at a molecular level.

Chapter 2

Results and Discussion

2.1 Setup for super-resolution microscopy of mobile specimens

Super-resolution microscopy depends on some key features of the imaging process in order to be able to detect individual steps of kinesin motors. Optimally, the most high-end components available are combined with custom-built solutions in one setup allowing specific design choices for the application at hand. A custom-built setup was therefore built for multi-color step detection of kinesin-2 motors and optimized primarily for high photon efficiency and stability. This chapter describes the design decisions and capabilities of the setup. Some of the components and the general setup in an earlier stage have already been described in [31].

2.1.1 The influence of localization accuracy and drift on step detection

The stepping of a molecular motor is typically visualized by a distance over time plot. In this representation, idealized steps are represented by two main characteristics. The data shows stable horizontal plateaus while the respective head is bound to the filament. The length of these plateaus characterizes the time the head stays bound to the filament in one position. This parameter is optimized for step detection in the relatively slow fluorescence assays by reducing the ATP concentration and thus elongating the times the motor stays bound. The plateaus are separated by quasi instantaneous vertical steps, almost vertical due to the movement of the heads happening on very short timescales (µs) [9].

Two parameters limit the performance of FIONA imaging, the standard deviation of the fit for localization and the stability of the setup for drift. The minimization of these parameters is important in order to optimize the performance of step detection algorithms in two ways. The localization accuracy in single frames also defines the ability of the algorithm to determine the actual position of the objective. More importantly however, the ability of the algorithm to detect steps is very dependent on horizontal plateaus with low fluctuations and steep transitions between the plateaus (Figure 2.1). The optimization of these parameters in the custom-built setup is described in the following.
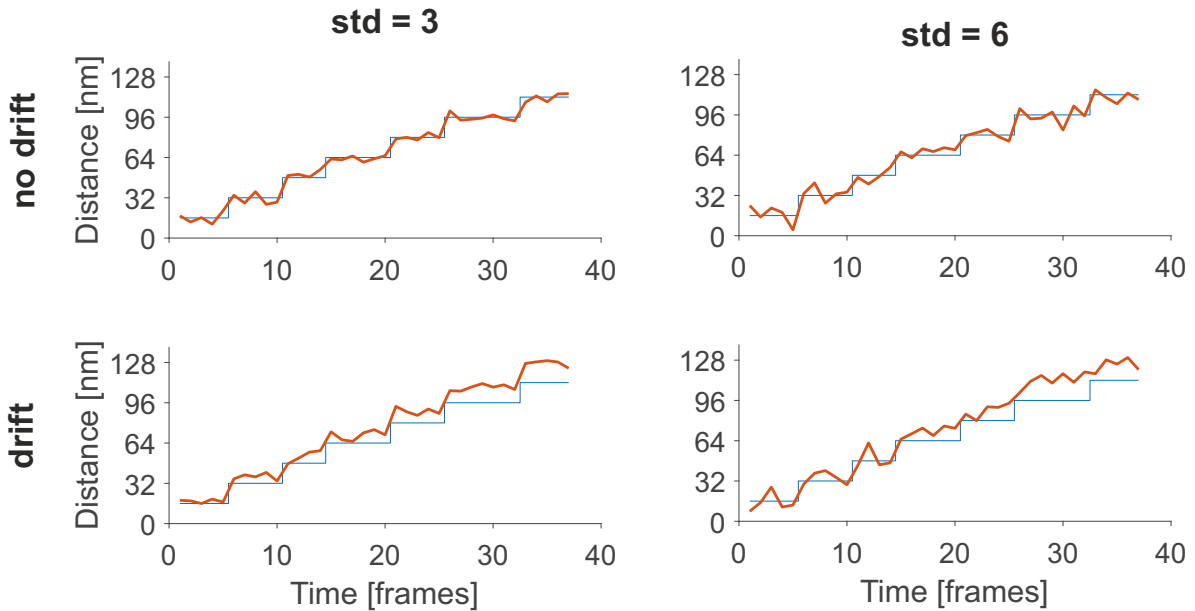
Figure 2.1: Step detection is dependent on low drift and localization accuracy
Drift and localization accuracy influence the ability to detect step-wise position changes in super-resolution microscopy. Steps in blue, observed data modified with the respective parameters in red. (top left) With a good localization accuracy and no drift, the steps can clearly be identified in the observed data and are easily detected by automatic step detection algorithms. (top right) At higher standard deviations of the localization accuracy, the plateaus of the steps are less obvious, causing step detection algorithm to misinterpret the data. Depending on the parameters, steps can be missed (false negatives) or fluctuations can be interpreted as steps (false positives). (lower panels) The addition of drift of 16 nm over 40 frames causes overestimation of the step sizes and non-horizontal plateaus, also increasing the probability for the step detection to miss steps.
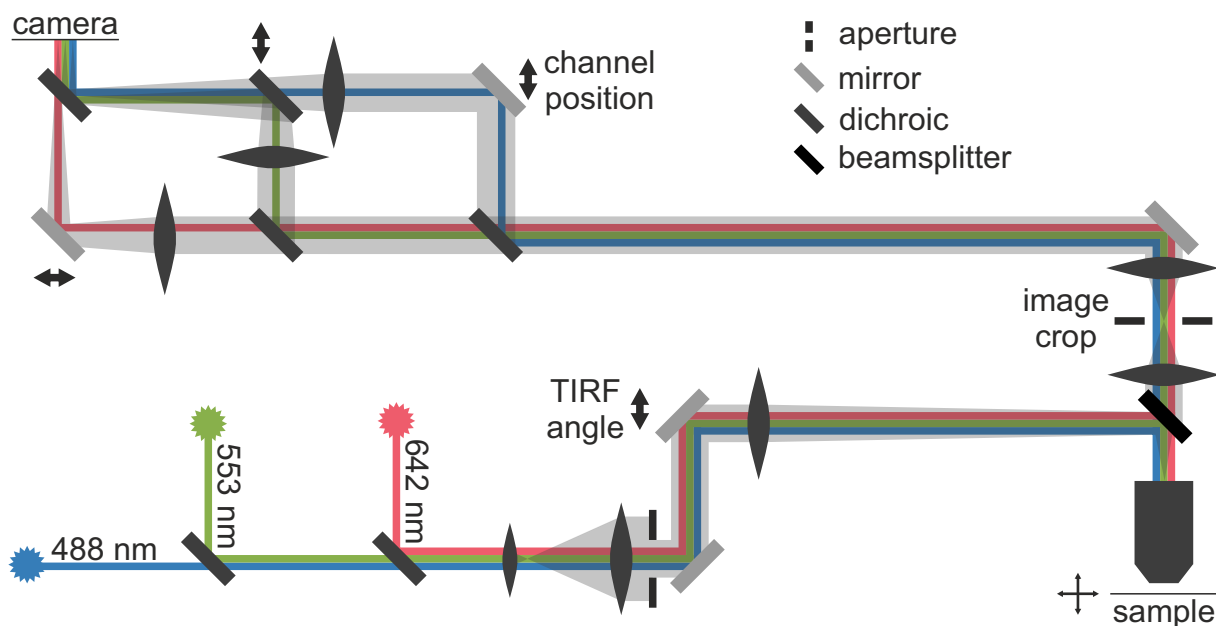
Figure 2.2: Schematics of the custom-built setup
The colors represent the laser wavelength in the excitation path and the corresponding fluorescent light in the emission path. The gray overlay shows the size of the excitation beam and the collimation of light in the imaging part. Where touching, colors are not separated spatially.

2.1.2   Overall design of the microscope setup

The design of the setup was performed with the specific applications described above in mind. It was therefore decided to build an objective-type TIRF microscope for observations close to the coverslip. In order to observe both heads of the motor at the same time and have an additional color for more flexibility, three separate channels were implemented. As the temporal relation of the stepping is important, all channels are imaged on the same camera, ensuring no temporal offset or drift between the channels occurs. This also makes an intricate setup for color-separation and recombination necessary. The overall design is presented in Figure 2.2.

The beams of three excitation lasers (488, 553 and 642 nm, 100 mW each, Oxxis S.A.) are combined by two dichroics (all Semrock Inc). The beam diameter is increased by a telescope (Thorlabs) and the profile is cropped by an adjustable aperture. Two mirrors are used for precise adjustment of the beam path onto the beamsplitter (Chroma) and into the objective lens (APON100XHOTIRF UIS2, 100x, 1.7 NA, Olympus K.K). The second mirror and the lens that focuses the beam on the back-focal plane of the objective are mounted on a translation stage, in order to allow for an adjustment of the TIRF angle.

In the imaging path, the beamsplitter separates the back-reflected laser light from the fluorescent signal. A 150 mm lens (Qioptiq Photonics GmbH) creates an image, that is cropped using an optical slit with adjustable aperture. A second 150 mm lens then recollimates the light for color separation. The light from the three different fluorophores is split using two high-pass filters. The channels are offset and focused by 250 mm lenses individually before recombination by one high-pass and one low-pass filter. One mirror or dichroic per channel is mounted on a translation stage together with the corresponding lens, allowing independent positioning of the channels on the camera chip. All channels are then recorded simultaneously on an iXon888 Ultra (Andor Technology Ltd) emCCD camera, yielding a pixel size of 93 nm. Fused silica coverslips are used with this setup (V-A Optical Labs Inc.).

2.1.3 Optimization for localization accuracy

The resolution of super-resolution techniques that depend on the localization of single fluorophore positions depends fundamentally on the number of collected photons and the background signal not originating directly from the observed fluorophore. The determination of the super-resolved position of the fluorophore is typically achieved by fitting a gaussian distribution to the observed spot from a single fluorophore. The accuracy of this fit is better for a bigger number of samples (photons), the exact relation to the number of collected photons can be derived from the characteristics of the fitting procedure [85].

Theoretical considerations for localization accuracy

The one-dimensional case will be derived here and later extended to the two-dimensional case present for the data of a widefield super-resolution microscope. In the case of low background noise, the photon shot noise describes the quantization of a point-spread-function that is inherently resolution limited due to the Abbe-limit. Each detected photon therefore gives a data point for the determination of the original position of the observed fluorophore. The best approximation of the position of the fluorophore is therefore the mean position of all detected fluorophore positions.

$$x_0 = \frac{1}{N} \sum_{i=1}^{N} x_i \tag{2.1}$$

The standard error of this approximation is given for a gaussian profile with the standard deviation of s by the statistics as

$$\langle(\Delta x)^2\rangle = \frac{s^2}{N}. \tag{2.2}$$

with the number of observations N. As photons are binned in pixels by the camera however, the individual positions x_i can only be determined to the size of the pixel. This binning into the pixel size a therefore adds another term to the standard error determined by the variance of a top-hat distribution of size a. This results in a standard error for the localization of solely shot-noise limited localization of

$$\langle(\Delta x)^2\rangle = \frac{s^2}{N} + \frac{a^2/12}{N} = \frac{s^2 + a^2/12}{N}. \tag{2.3}$$

For the presence of background noise from other sources than the fluorophore itself, the accuracy consideration becomes more intricate. The typically used least-squares fitting procedure to determine the parameters of the distribution tries to minimize the sum of squared errors given by

$$\chi^2(x) = \sum \frac{(y_i - N_i(x))^2}{\sigma_i^2}. \tag{2.4}$$

With y_i the photons counted in pixel i, $N_i(x)$ the expected number of photons counted from a particle that is located at position x and σ_i the expected uncertainties in the count. σ_i is thereby given by the sum of the uncertainties derived for photon-counting noise and the background noise b.

$$\sigma_i^2 = N_i(x) + b^2 \tag{2.5}$$

The fitting procedure then looks for the minimum by solving $d\chi^2/dx = 0$. This, the expansion of $N_i(x)$ to the first order around x_0 and assuming a relatively accurate photon count gives the equation

$$\Delta x \approx -\frac{\sum \frac{(N_i(x_0) - y_i)N_i}{\sigma_i^2}}{\sum \frac{N_i^2}{\sigma_i^2}}. \tag{2.6}$$

This results in a mean square error of

$$\langle(\Delta x)^2\rangle = \frac{1}{\sum(N_i^2/\sigma_i^2)}. \tag{2.7}$$

At the limit of a purely background noise limited acquisition this equation can be evaluated by approximating N_i with a normal distribution with the standard deviation s and

replacing the sum with an integral. It has to be noted, that this replacement results in the negligence of pixelation noise, as the pixels are assumed to be infinitesimally small. This results in a standard error for the background-limited case of

$$\langle(\Delta x)^2\rangle = \frac{4\sqrt{\pi}s^3b^2}{aN^2}. \tag{2.8}$$

Adding both limits gives an approximation for the standard error of localization that is correct to 10% for the whole range of noise conditions as tested by numerical analysis in [85].

$$\langle(\Delta x)^2\rangle = \frac{s^2 + a^2/12}{N} + \frac{4\sqrt{\pi}s^3b^2}{aN^2}. \tag{2.9}$$

For the adaptation to a two-dimensional grid of a camera chip, the corresponding integrals have to be evaluated over two dimensions resulting in a standard error for this case of

$$\langle(\Delta x)^2\rangle = \frac{s^2 + a^2/12}{N} + \frac{8\pi s^4 b^2}{a^2 N^2}. \tag{2.10}$$

This allows for an analysis of the parameters that have to be optimized in a microscope setup in order to achieve the highest localization accuracy possible. The standard deviation of the distribution is given by the Abbe limit.

$$s = \frac{\lambda}{2NA} \tag{2.11}$$

This can be minimized by maximizing the numerical aperture NA of the system and minimizing the wavelength of the captured light λ. These optimizations are subject to certain practical limitations that are discussed later in this chapter. The minimization of background noise b also minimizes its contribution to the uncertainty in the second term. The maximization of the number of collected photons N however minimizes the background term faster than the term for the photon shot noise. The localization error due to background noise is therefore small, if the number of collected photons is high. The pixel size a influences both contributions differently and is also a factor in the amount of background noise observed and the capability of the setup to collect photons. The minimum of equation 2.10 can be found to be at

$$a = s\sqrt[4]{96\pi b^2/N} \tag{2.12}$$

Practical design decisions for the realized setup

Numerical aperture NA

The numerical aperture of a microscope setup is mainly defined by the numerical aperture of the used objective lens. The numerical aperture for common oil immersion microscopes is limited to around 1.5 due to geometrical limitations that limit the angle of gathered light to below 90° and the refractive index of typical immersion oil at 1.5.

$$NA = n\sin(\alpha) = 1.5 \tag{2.13}$$

The geometrical limitations can be overcome by performing so called 4-pi microscopy, also gathering light with a second objective lens from the backside of the sample. This approach is however not suitable for the use with TIRF-microscopy and was therefore not employed here. Why TIRF microscopy is beneficial for the assays performed in this work will be discussed later. The best leverage point is therefore to optimize the refractive index in order to achieve a higher numerical aperture of the setup. A special objective that uses immersion liquid with a refractive index of 1.78 is used in order to increase the light gathering performance. As all material that is in contact with the immersion medium has to be matched to its refractive index, fused silica coverslips are used for the sample chamber and sapphire glass is used for the lens in the objective. With this, the Olympus HOTIRF 100x objective achieves a numerical aperture of 1.7, higher than any other objective lens on the market.

Wavelength λ

Minimization of the wavelength will lead to a smaller standard deviation of the initial collected peak of photons. In the extreme case of electron microscopes, the short wavelength of accelerated electrons is used to achieve very high resolutions. In fluorescence microscopy, the wavelength is also limited by the availability of dyes at certain colors. As the setup was desinged to achieve step detection in colors over a wide range of the visible spectrum, wavelength considerations for the optimization of localization accuracy were not taken into account.

Background noise b

While the contribution to the standard error of localization of the background noise is relatively small for high numbers gathered of photons from the object, it is still important to minimize its impact for high-accuracy applications. The minimization of signal from out-of-focus fluorophores is achieved by the implementation of TIRF microscopy. In

the implementation used for this setup, a laser beam enters the back focal plane of the objective off-center and is therefore transmitted to the coverslip/sample interface at an angle. As the interface from the coverslips to the water is a transition from a medium with higher refractive index (fused silica $n_1 = 1.7$) to a medium with lower refractive index (water $n_2 = 1.33$), Snells law gives a critical angle θ_C at which no more light is transmitted into the water.

$$\theta_C = \arcsin \frac{n_2}{n_1} \sin \theta_t = 51.5° \tag{2.14}$$

This is the case, when the transmission angle θ_t gets to 90°. This critical angle is considerably smaller for fused silica coverslips than the critical angle for a standard glass/water interface (~62°). At incident angles (θ_i) bigger than this angle, all light will be reflected back at the silica/water interface. The solution of the Maxwell equations in this case calls for a so-called evanescent wave inside the water at the interface that decays exponentially with the distance to the interface [78]. This decay is described by the exponential parameter d.

$$d = \frac{\lambda}{4\pi}(n_1^2 \sin^2 \theta_i - n_2^2)^{-1/2} \tag{2.15}$$

At an angle θ_i of 52° and for light of wavelength $\lambda = 500\,\text{nm}$, this gives a decay with a constant of $d = 248\,\text{nm}$ which can be reduced by increasing the angle of incident. Thus only a small volume directly at the silica/water interface is illuminated by the laser. By attaching the filaments that the motors walk on to the coverslip, it was ensured that all measurement are taken in this region. In Figure 2.20 it can be seen, that the filaments will typically be at a maximal distance from the coverslip of around 50 nm. Fluorescence from motors in the solution can therefore be avoided by setting the corresponding TIRF angle. At an incident angle of 59° the penetration depth parameter is 75 nm, sufficient to illuminate the motors attached to the filaments and small enough to optimally suppress background excitation. To optimize this setting, a translation stage was included in the laser path that allows for variable offsets of the laser beam from the center of the back focal aperture of the objective. An optimal TIRF incident angle can thus be chosen for the assay at hand.

Another source of background noise is dark noise that originates from dark current that is induced by the voltages and spontaneous free electrons on a camera chip. The most effective way to reduce dark noise is the cooling of the chip in the chosen camera to reduce

the probability of spontaneous free electrons. The CCD chip in the iXon 888 Ultra (Andor Technology Ltd, Belfast UK) used in this setup can be cooled to $-80\,°C$, minimizing the occurrence of spontaneous free electrons in the pixels. A good minimization of background noise was already observed at the $-65\,°C$ used in the experiments presented in this thesis.

Background noise in the obtained data can also be caused by inconsistencies or imprecision in the counting of electrons in the pixel by the analog-to-digital converters (ADC) in the camera readout. The iXon camera therefore uses an electron multiplying gain register to enhance the signal before the readout and thus minimize the influence of readout noise [86]. The electrons in each pixel pass this register before readout. The application of a special voltage pattern for electron transfer induces electron avalanches that multiply the number of electrons before they reach the ADCs. With this technique it is possible to reduce the readout noise to $< 1e^-$.

Pixel size a

As described above, there is an optimal pixel size for super-resolution imaging, that is dependent on the amount of background noise, the amount of collected photons in the peak and the point spread function of the peak. For the imaging problem at hand a set of parameters will be assumed to estimate the optimal pixel size for the setup ($\lambda = 560\,\text{nm}$, $NA = 1.7$, $b = 0.7$, $N = 2000$).

$$a = s\sqrt[4]{96\pi b^2/N} = \frac{\lambda}{2NA}\sqrt[4]{96\pi b^2/N} = 86\,\text{nm} \tag{2.16}$$

The physical size of the pixels in the camera used is $A = 13.3\,\mu\text{m}$. With the magnification of the objective $m = 100$ and the ratio of focal lengths used in the 4f setup of $f = 150/250$ this results in a theoretical pixel size of

$$a = \frac{A}{m}f = 80\,\text{nm}. \tag{2.17}$$

In practice, a pixel size of $93\,\text{nm}$ was measured for the setup.

Number of collected photons N

The number of collected photons is the most important and most discussed parameter for the optimization of localization accuracy in super-resolution microscopy. Different stages in the imaging procedure define how many photons can actually be collected by the camera. The main three are, how many photons are actually emitted at the object of interest, how many of those photons can be collected by the objective lens and how many of
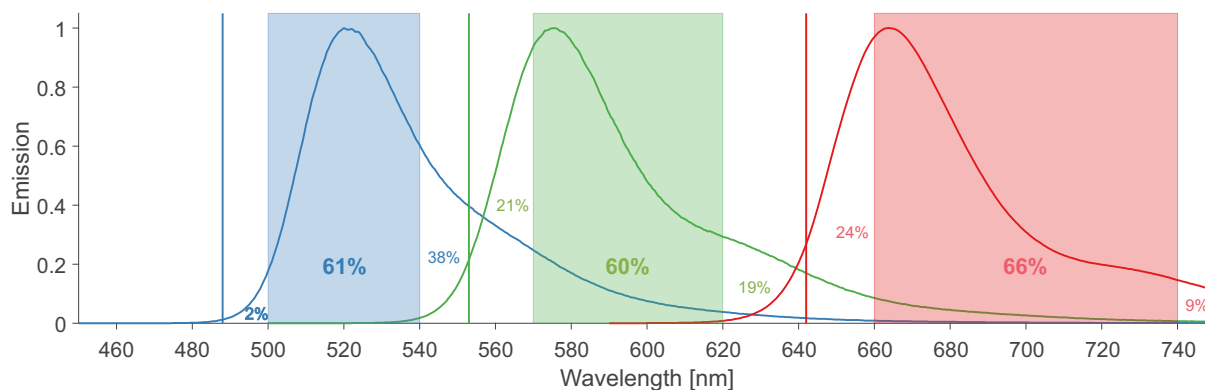
Figure 2.3: Analysis of the photon efficiency of the beamsplitter
Emission spectra of Atto 488,550 and 647N and approximate transmission bands of the 89016bs beamsplitter (Chroma, Bellows Falls USA). Numbers indicate the percentage of light in the regions below and above the transmission bands (small font) and the percentage of transmitted light (bold big font) in corresponding colors. Due to the spectral design of the setup alone, around 40 % of the light captured by the objective lens is lost.

these pass the optical components of the microscope to induce electrons in the CCD chip of the camera.

The amount of emitted photons is predominantly defined by the employed fluorophores. The experimental constrains on this choice for this thesis were the tendency of kinesin-2 to unspecific binding and the choice of SNAP- and Halo-tags for fluorophore attachment. The highest amount of photons would be expected by using quantum dots as fluorescent dyes for the labeling. Figure 2.5 shows, that kinesin-2 binds unspecifically to quantum dots, the heads could therefore not be labeled specifically with this technique. Fluorescent molecules that are directly fused to SNAP- and Halo-tag ligands were therefore used here. The amount of dyes that are commercially available for SNAP- and Halo-tag attachment is very limited. Fortunately, it was possible to ensure support from Luke Lavis and Jonathan Grimm and use their Janelia Fluor dyes modified with SNAP- and Halo-tag ligands. A non-radiative decay via rotation is inhibited in these dyes by the addition of ring structures to the corresponding bond and thus achieve an increase in both brightness and photostability of a factor of around 2. Figure 2.5 shows the specificity of the dyes for their respective tag.

The capability of the objective lens to collect photons is directly described by its numerical aperture. This parameter was optimized as described above.

Many parameters define how much light passes the optical components of the system.

The biggest compromises have to be made due to the necessity to image three colors. The excitation and emission spectra of the dyes used will overlap in the relatively small span of wavelengths suitable for fluorescent imaging. The most light is therefore lost at the filter called beamsplitter that sets the excitation and emission bands for the whole setup. The Chroma 89016bs beamsplitter was chosen due to its good fit to the lasers and dyes used with the system. Figure 2.3 shows the emission paths of three Atto fluorophores and the transmission bands of the filter used. The amount of transmitted light from the whole emission was calculated from the area inside the emission band over the total area of an emission peak. This resulted in transmission values between 60 and 66 % depending on the channel.

Additionally, light is reflected at each interface of materials of different refractive indexes, as is the case at lenses for example. The amount of reflected light can be reduced by anti-reflective (AR) coatings to transmission values of ~99.7 %. While reflectance of lenses has to be minimized, the contrary is true for mirrors in the light path. The mirrors used here have reflectance ratings of 99.7 %. While the loses are relatively small, this still suggests the minimization of optical components employed in the optical setup. As the design decisions for this setup are to image all colors at the same time and on the same chip, it had to be compromised in this regard. The collected light therefore has to pass a number of dichroic filters that are responsible for color separation and offset. The quality of these filters determines the reflectance/transmission capabilities that in turn determine the photon efficiency. The dichroic mirrors have an average transmission/reflectance deficiency of around 3 %. The notch filters used for the extraction of any residual laser light have very good transmission ratings outside the notches, for this analysis a 100 % transmission efficiency will be assumed. In each channel, the light passes three lenses, one or two mirrors, two notch filters and three or four dichroic filters. This results in a total loss of photons due to reflectance of

$$r_{loss} = 1 - t_{loss} = 1 - (r_{lense}^3 t_{mirrors}^2 r_{notch}^2 r_{dichroic}^4) = 13\,\% \tag{2.18}$$

In order to be detected, a photon that passed all optical components then has to cause a free electron in the pixel of the CCD chip. The iXon camera therefore employs a back-illuminated chip that optimizes the exposure of the CCDs silicon layer to the incoming photons. For this particular camera the quantum efficiency (qe) is $> 95\,\%$ for the spectral range of the used dyes.

In conclusion, the amount of photons collected by the objective lens that cause a signal

on the camera can be estimated to be

$$T_{setup} = (1 - r_{loss}) * t_{beamsplitter} * qe = 52\,\%. \tag{2.19}$$

The number of collected photons can be increased by longer exposure times. This in turn decreases the number of data points in a given plateau of the stepping data, decreasing the reliability of step detection algorithms. In practice, exposure times of 500 ms using the atto dyes and 400 ms using the Janelia Fluor dyes have proven to be a good compromise for optimal step detection performance.

### 2.1.4 Optimization for low drift and optical stability

As detailed above, it is important to minimize any drift in the imaging setup in order to allow for optimal detection and analysis of steps. This would be best achieved by the minimization of moving parts throughout the imaging path. However, the microscope was designed to be able to image three colors at the same time and still have the possibility to also image only one color with a full field-of-view without manual adjustments. This results in the necessity to position each channel individually on the camera chip, introducing three translation stages into the setup. Despite these compromises, the setup achieves good stability due to some other optimizations in the design.

Where possible, stable optical mounts have been chosen for all optical components to minimize drift due to differences in temperature that lead to elongation in the materials. As the 4f system includes two projections, the order of the resulting drift in the final imaging plane is on the order of the initial drift of the respective component.

The positioning of the sample is most prone to drift. Instead of the typical vertical position in inverse microscopes, the objective is therefore oriented horizontally in this setup. This allows the sample stage to approach the objective from the front. The sample chamber is therefore stabilized by the stage from one side and the objective lens from the other. This also allows also for an adjustment of the focus by directly moving the sample and thus the objective lens can be mounted statically. For nanometer adjustments, the common approach would be to use a piezo-actuated stage that is mounted to another stage actuated by standard stepper motors. By implementing a stage that uses piezo-stepper motors it was possible to minimize the amount of moving parts in this section. These motors apply a piezo crystal that is attached in an angle onto a rail and connects to a second mobile rail in its extended conformation. By applying a frequency to this crystal,

it will change its position of interaction with the mobile rail by a slip-and-catch mechanism for each cycle, thus the name piezo-stepper. The position of the stage can then be adjusted with nanometer precision by applying a variable voltage to the piezo while it connects to the mobile rail.

2.1.5   Proof of step detection capability in three channels
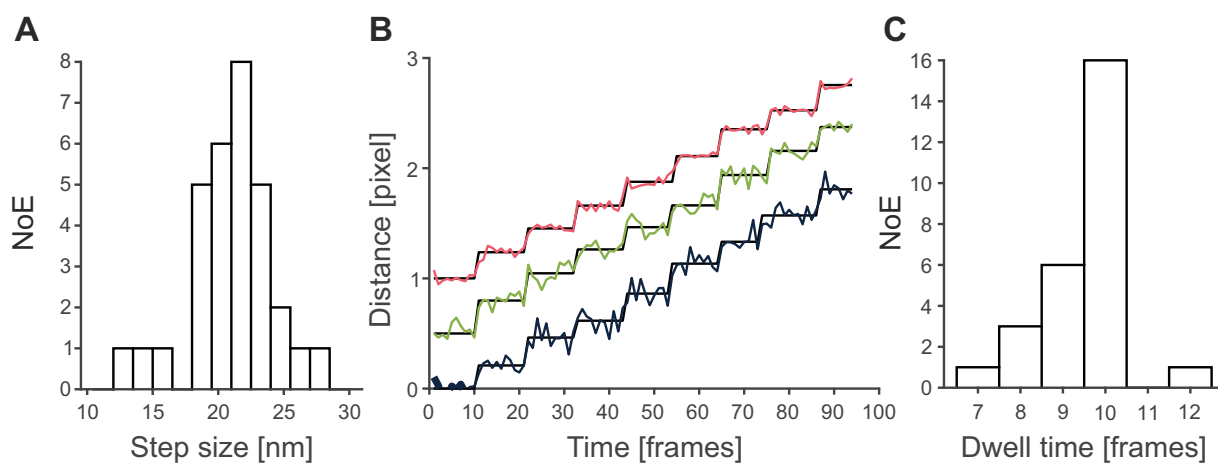
Figure 2.4: Analysis and experiment of piezo-stage driven steps
A The step size distribution shows a peak close to the expected 20 nm that was set as displacement.
B Step data as recorded in colors offset for visibility. Steps where set to occur every 10 frames with a displacement of ~20 nm. Black lines are the steps as detected by a gliding t-value algorithm.
C The dwell time distribution shows a peak at 10 frames, the set time between displacements.

With all the optimizations mentioned above, the setup can achieve the design goals with good fidelity. The performance was tested by checking the ability to track sub 20 nm steps in three channels at the same time. Temporal relation between the channels is ensured by imaging on the same emCCD chip concurrently. Using the piezo-driven stage, ~20 nm steps similar to the displacements expected from kinesin steps were emulated. The stage was set to perform a quasi discrete displacement every 5 seconds, which corresponds to around 10 frames at the set cycle time of 505 ms. Fluorescent Janelia Fluor dyes (JF488, JF549 and JF646) were attached to a cover-slip via non-specific binding in a dilution that led to single fluorophore peaks [87, 88]. The comparison of images from the different channels showed no visible cross talk from one channel to the other. Differences in the photon efficiency between the channels in the setup and different performance lev-

els of the fluorophores lead to differences in the localization accuracy (noise-levels in the step data). These peaks were followed over time and it was possible to show concurrent step detection using a gliding t-value algorithm in all the channels and stable plateaus (Figure 2.4B).

The two most important step parameters for a motor were thus simulated by the displacement of the stage (step size) and the times between stage displacements (dwell times). The analysis of this data enabled a test of both the setup and the algorithms used. Both parameters are recapitulated from the data after automatic step detection and analysis (Figure 2.4A & C). This shows the superior capabilities of the implemented setup for kinesin step detection experiments.

2.1.6 Summary

The theoretical background of accuracy in super-resolution microscopy was introduced in this chapter. Discussing the individual leverage points for optimal localization accuracy, the design decisions for the setup were motivated and the practical implementation explained. The setup is shown to be capable of detecting sub 20 nm steps using standard fluorophores in three channels.

2.2 Multi-color super-resolution microscopy of mobile specimens
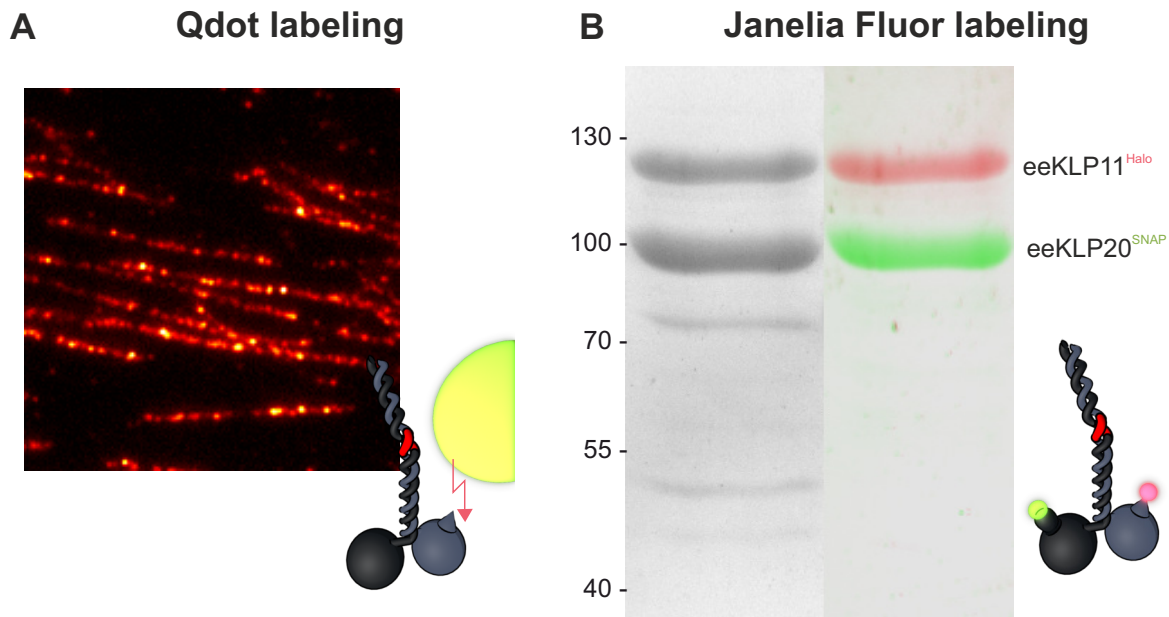
**Figure 2.5: Specific and efficient labeling was possible with Janelia dyes, but not with Qdots**

A Incubation of the motors with Qdots but without the linking biotin-Halo still showed efficient colocalization with microtubules. A direct incubation of the Qdots with the microtubules showed no interaction however. This indicates an unspecific interaction of the quantum dots with the microtubules.

B The Halo- and Snap-tag was labeled with the respective JaneliaFluor dye respectively. (Left) Coomassie stain of the proteins. (Right) Overlay of two images color coded for the respective channel. Taken on Biostep Celvin S in channels with 525 nm (blue) and 625 nm (red) excitation. The dyes are only detected on the targeted motor domain.

The heterodimericity of kinesin-2 offers the unique opportunity to label the motor with two colors identifying the respective motor domain. We designed constructs based on the KLP11 and KLP20 subdomains of *c. elegans* kinesin-2. Fusing SNAP- or Halo-tags to the n-terminal end of the sequences enabled labeling with the respective dyes. It was first attempted to use a biotin-Halo ligand and a streptavidin coated quantum dot to label a Halo-tag on the motor. This would have allowed for superior photon counts and observation times compared to fluorescent molecules. However, kinesin-2 motors are very susceptible to unspecific binding. A negative control without the biotin-Halo ligand, the supposed connection between the quantum dot and the kinesin, still showed a high dec-

oration efficiency on microtubules (Figure 2.5). Using only the quantum dots on the microtubules showed quasi no attachment. This indicates, that kinesin-2 binds unspecifically to the quantum dots, rendering this approach unsuitable for step detection. Fluorescent dyes that attach directly to the respective tags were therefore used instead. The commercially available dyes were used for the single-color tracking and Janelia Fluor dyes that were a generous gift from Luke Lavis and Jonathan Grimm for the dual-color applications [87, 88]. The dyes are modified with SNAP- and Halo-tag binding motives directly on the fluorescent molecule. As the binding to the tags is very specific, each head can be labeled with one specific color and only at the head. These labeled constructs behaved nominally at saturating ATP concentrations (Supplementary Figure 5.1).

With this labeling technique in place it was possible to track both heads of the motors at the same time and obtain stepping traces for both channels (Figure 2.6). The two main features of the steps, sizes and dwell times, can be extracted from these traces. Dwell times are the lengths of the plateaus between steps. As described above, step sizes are the distances between positions from one plateau to the next, i.e. the displacement distance of the head. Steps can be detected automatically using a gliding t-value approach or an implementation of the Potts algorithm. The Potts algorithm was used for the dual-color experiments, while the gliding t-value algorithm was used for the rest of the data (see [89] and Materials and Methods for details).
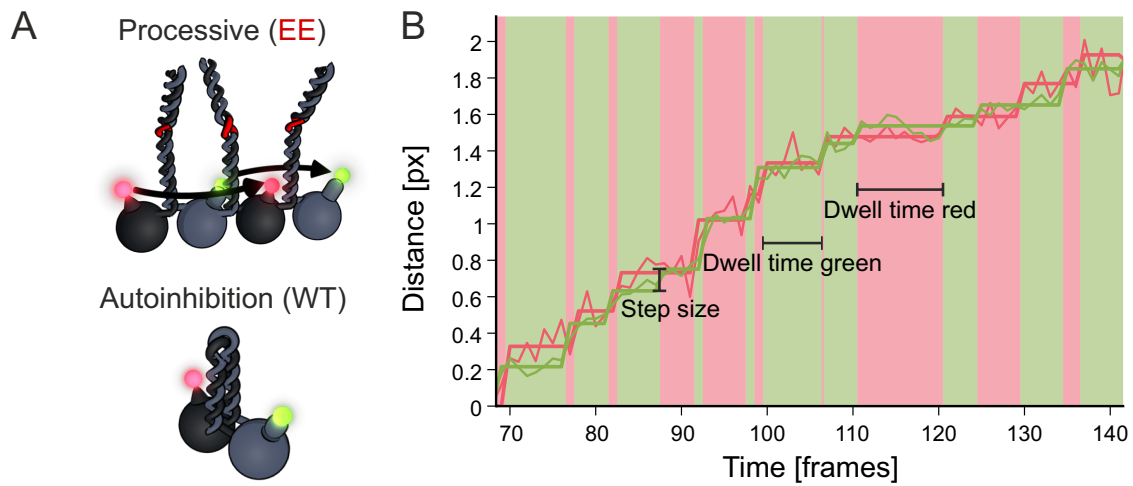
Figure 2.6: Dual color FIONA measurement of KLP11/20 at rate-limiting ATP concentrations

A Depiction of the tail conformation in the eeKLP versus the wtKLP and fluorophore repositioning during a processive hand-over-hand walk.

B eeKLP11[Halo] data in green and eeKLP20[SNAP] in red, with respective detected steps overlaid. Data was collected during stepping on microtubules. Alternating movement of the motor domains can be seen with corresponding dwell times highlighted in the background. The data was recorded at an ATP concentration of $0.4\,\mu$M.

2.3   Kinesin-2 stepping reflects its heterodimeric nature

The heterodimeric nature of many kinesin-2 motors has sparked discussion about a possible difference in stepping behavior between the distinct heads, an effect commonly called limping. The fact that commonly used kinesin motors are homodimers has limited these experiments to 'artificial' heterodimers and complicated the labeling process. Thus, FIONA experiments on kinesin motors have stopped at revealing the basic stepping mechanism only so far. With the unprecedented accuracy of the dcFIONA data it was possible to analyze the stepping of kinesin-2 closer than ever before. Most of these results were published in [90] and parts of the paper are quoted here literally.

2.3.1   Individual step sizes do not show conclusive differences
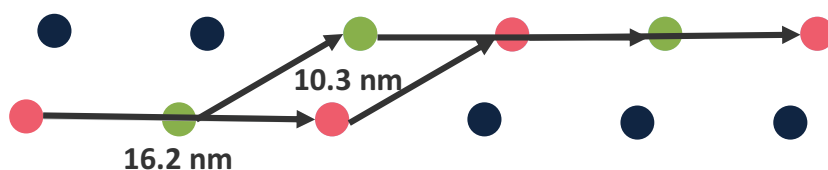
Figure 2.7: A difference in step sizes is not expected, even for only one sidestepping subunit
A theoretical stepping sequence with only the green motor initiating a switch of protofilaments. If the red head always steps in front of the green head, as expected for a protofilament-tracking behavior, it will also follow it to the new protofilament. This results in the same step size for this event than a step that would initiate the switch of protofilaments. Overall, even though the red head always steps in front of the green head, the step size distributions for both heads will show the same distribution of step sizes.

The first thing looked at in the dual-color FIONA data were the individual step sizes of the subunits. The different heads might be optimized for walking on the axoneme and thus show different step sizes as detailed in chapter 2.5. However, for eeKLP11[Halo]/20[SNAP], the step size is equal for the two heads (p = 0.93). For eeKLP11[Halo]/20[SNAP] and eeKLP11[SNAP]/20[Halo], the p-value is small ($<1^{-4}$), but no head shows consistently the bigger or smaller step size (Supplementary Figure 5.2). Overall, no conclusive trend for one or the other head having a bigger step size became apparent. The same is true for the directions of stepping, both heads show a rather balanced direction histogram. If one has a closer look at the hand-over-hand mechanism however, it becomes obvious, that dif-

ferences in the stepping regarding sizes and directions can hardly be observed this way (Figure 2.7). Consider a starting position with both heads bound to the same protofilament. The trailing head (1) steps in front of the other head (2) and switches protofilament, leading to a step size <16 nm. The second head is protofilament tracking, it therefore steps in front of head (1). To do so, however, it will also switch protofilament following head (1), again resulting in a small step size. Both heads would therefore follow the same (just offset) path and thus show the same step size distribution.

This observation suggests a closer analysis of the stepping sequence. The most intuitive way to look at the data would be to check which motor is initiating the side step. This would mean that after a long step in one head the other head would sometimes show a short step, but not the other way around. No such behavior was found in the data obtained (Supplementary Figure 5.3). Again, closer reflection on the stepping sequence shows that this assumption would not be true, once the probability for a sidestep is close to 50 %, which is shown to be the case in chapter 2.5. A difference in the step sizes for the different heads of KLP11/20 can therefore not be excluded. These issues in separating the step sizes fortunately do not apply for the analysis of dwell times, which allowed me to study the differences in the timing of the two head domains.

2.3.2 The two heads of the KLP11/20 motor display distinct timing of stepping

The dwell times for a construct with only one labeled head have been shown to be distributed according to a double exponential distribution [7]. Only the steps of the labeled head can be observed in these experiments, while the step of the other head is 'hidden'. As the hidden step has to occur before the next observed step is possible, two rate-limiting events are necessary for each observed step. This leads to a convolution of two exponentials for the dwell time distributions in these experiments [7, 28]. This is also true for the kinesin-2 if labeled at only one head (Figure 2.15).

In the dcFIONA measurements, the dwell times in the step primed position can be extracted, i.e. only the time a head spends in the trailing position. The individual dwell times of the two heads in the eeKLP11$^{\text{Halo}}$/20$^{\text{SNAP}}$ motor were measured (Figure 2.6B). For these dual color measurements, the double exponential is expected to split into one single exponential distribution for each head [91]. Intriguingly however, two different distributions were observed. While the dwell times obtained from the KLP20 subunit displayed a single exponential as expected, the dwell time from the KLP11 subunit clearly
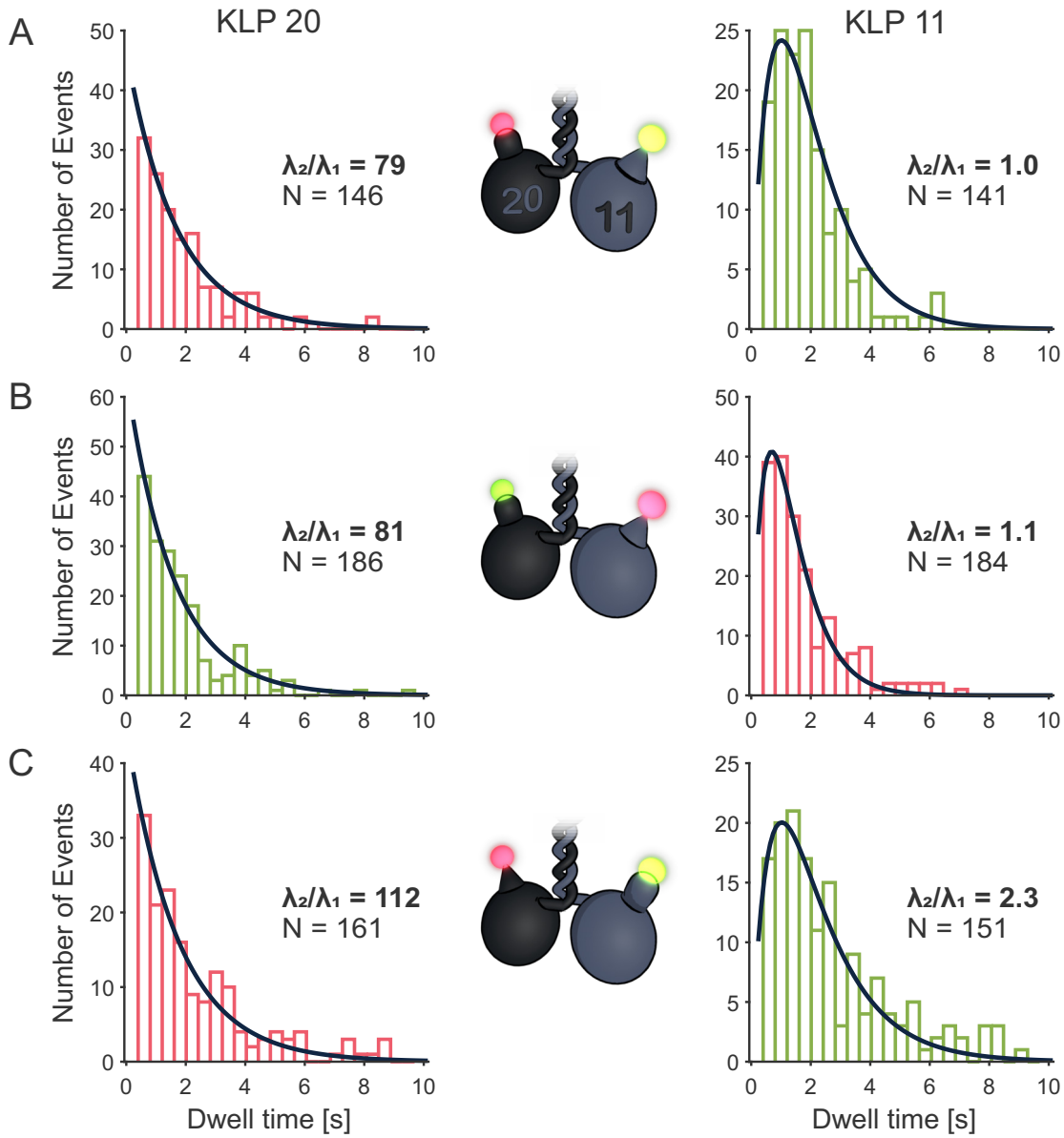
Figure 2.8: The Dwell time distributions for KLP11 and KLP20 are different
Dwell time distributions of KLP20 and KLP11 with bars colored in the respective color the data was measured in (green for JF549, red for JF646). KLP20 dwell times show a distribution close to a single exponential. KLP11 dwell times are fitted well by the double exponential model with similar values for both parameters (black line). If the KLP20 data is fitted with the same model, the ratio of the two parameters is about two orders of magnitude higher, resulting in a quasi single exponential fit. All fits resulted in r-squared values $> 90\%$
A eeKLP11[Halo]/20[SNAP] (20: $\lambda_1 = 0.6\,\text{s}^{-1}$, $\lambda_2 = 47.2\,\text{s}^{-1}$; 11: $\lambda_1 = \lambda_2 = 1.0\,\text{s}^{-1}$)
B eeKLP11[Halo]/20[SNAP] (20: $\lambda_1 = 0.6\,\text{s}^{-1}$, $\lambda_2 = 48.5\,\text{s}^{-1}$; 11: $\lambda_1 = 1.4\,\text{s}^{-1}$, $\lambda_2 = 1.5\,\text{s}^{-1}$)
C wtKLP11[SNAP]/20[Halo] (20: $\lambda_1 = 0.6\,\text{s}^{-1}$, $\lambda_2 = 67.2\,\text{s}^{-1}$; 11: $\lambda_1 = 0.6\,\text{s}^{-1}$, $\lambda_2 = 1.4\,\text{s}^{-1}$)
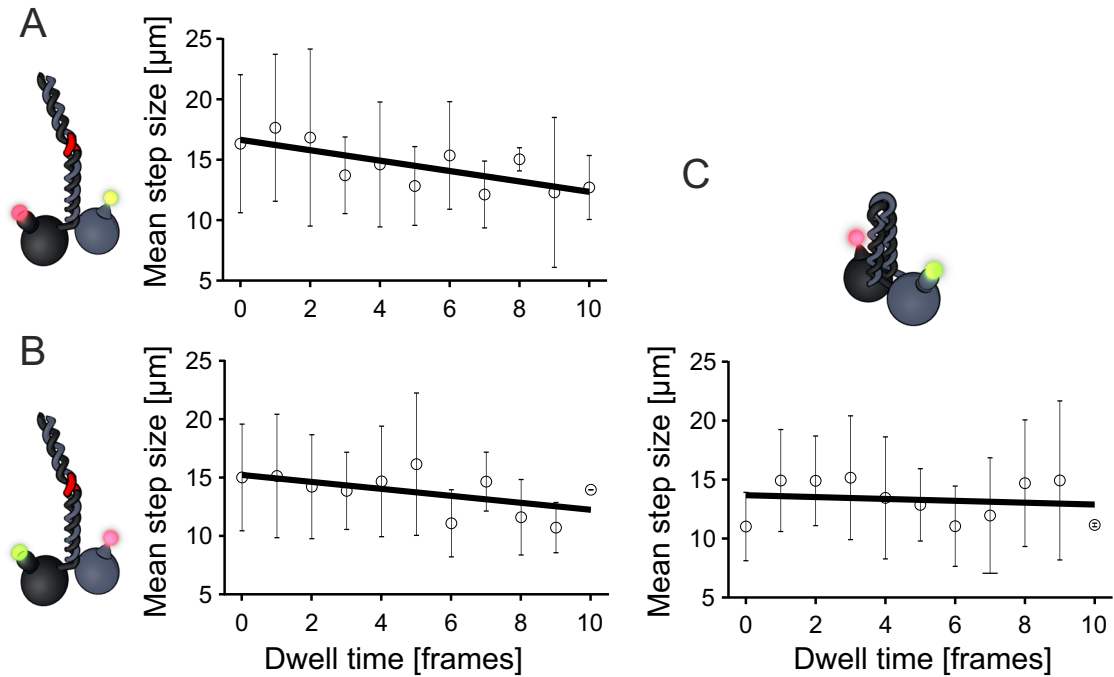
Figure 2.9: The step size is slightly dependent on the dwell time for eeKLP, but not wtKLP.
A & B A slight tendency for the step size to decrease with increasing dwell times can be seen. **C** The tendency visible for eeKLP is missing in wtKLP. Interestingly, the steps happening very fast (0 frames) are much shorter. This might hint to a different stepping mechanism for the short steps in the wild-type motor. However, the small number of events per dwell time should be noted. Thus, the statistics of the results does not allow for conclusive interpretations. **A** eeKLP11$^{\text{Halo}}$/20$^{\text{SNAP}}$, **B** eeKLP11$^{\text{Halo}}$/20$^{\text{SNAP}}$, **C** wtKLP11$^{\text{SNAP}}$/20$^{\text{Halo}}$

deviated from a single exponential but was instead consistent with a double exponential distribution (Figure 2.8 right).

To exclude any influence of the dyes or their relative optical paths in the setup, the dyes were switched (eeKLP11$^{\text{Halo}}$/20$^{\text{SNAP}}$ vs eeKLP11$^{\text{Halo}}$/20$^{\text{SNAP}}$) on the respective subunits. In addition, the position of the tags themselves were also switched (eeKLP11$^{\text{Halo}}$/20$^{\text{SNAP}}$ vs wtKLP11$^{\text{SNAP}}$/20$^{\text{Halo}}$) to exclude any influence of the specific tags on the behavior of the motor per se. In both cases, the double exponential dwell time distribution for the KLP11 subunit was confirmed, while the KLP20 subunit consistently displayed a single exponential distribution (Figure 2.8).

To further test the consistency of this observation, both data sets were fit using the same double exponential model (see Suppl Information). For the KLP11 subunit, the ratio of the two involved parameters was close to 1, indicating a similar influence of both values

on the stepping behavior. For the KLP20 subunit, in contrast, the ratio was about 100-fold higher, ultimately resulting in a near single exponential fit (Figure 2.8).

Together, these findings suggest that the steps taken by the KLP11 subunit include a second rate-limiting event in addition to the waiting time for ATP binding [7]. Ultimately confirming the presumed limp for heterodimeric motors. This behavior of the KLP11 subunit could so far not be resolved by tracking the net movement of the motor due to the similar mean dwell times of the two heads [38].

The obvious question is, if this difference in the dwell times coincides with a different mode of stepping. Regarding the step size as a readout for different stepping mechanisms, the step size was analyzed in relation to the dwell time spent before relocation. However, the data show no clear correlation of these two parameters that would be consistent for all tested contructs. There is a slight tendency for steps to be shorter for longer dwell times in the eeKLP, for wtKLP however, this tendency is not observed (Figure 2.9). An intriguing feature of the wtKLP graph is the small step size for the very fast steps (0 frames). This might hint to a slightly different pathway for these steps in the wtKLP. Notably, the KLP11 subunit also plays a central role in the auto-inhibition of the heterodimeric KLP11/20 motor (Figure 2.6A, bottom panel) [26], the study therefore turned to the wtKLP11/20 and asked whether the presence of the wild type stalk interferes with the dwell time distribution of the motor per se and if so whether it impacts one or both head domains during stepping.

2.3.3 Difference in stepping gives insight into the auto-inhibition of kinesin-2

The tail-mediated auto-inhibition is proposed to be brought about by suppressing the release of ADP from the binding pocket either directly or through interference with the inter-head communication by 'crosslinking' the heads [16, 20, 22, 23, 37]. As detailed above, this interaction can be prevented by introducing mutations in the stalk as our group previously demonstrated also with the heterodimeric KLP11/20 motor (Figure 2.6A) [12, 14–16, 18, 22]. Intriguingly however, it was also possible to relieve auto-inhibition by replacing the KLP11 with the KLP20 head domain or simply by switching the relative positions of the respective head domains in the wild type KLP11/20 [26]. Thus, not only the presence of the KLP11 head domain but also its correct positioning was essential to mediate auto-inhibition in the heterodimeric KLP11/20 motor.

Given the capability to now distinguish between the stepping cycles of the KLP11 and
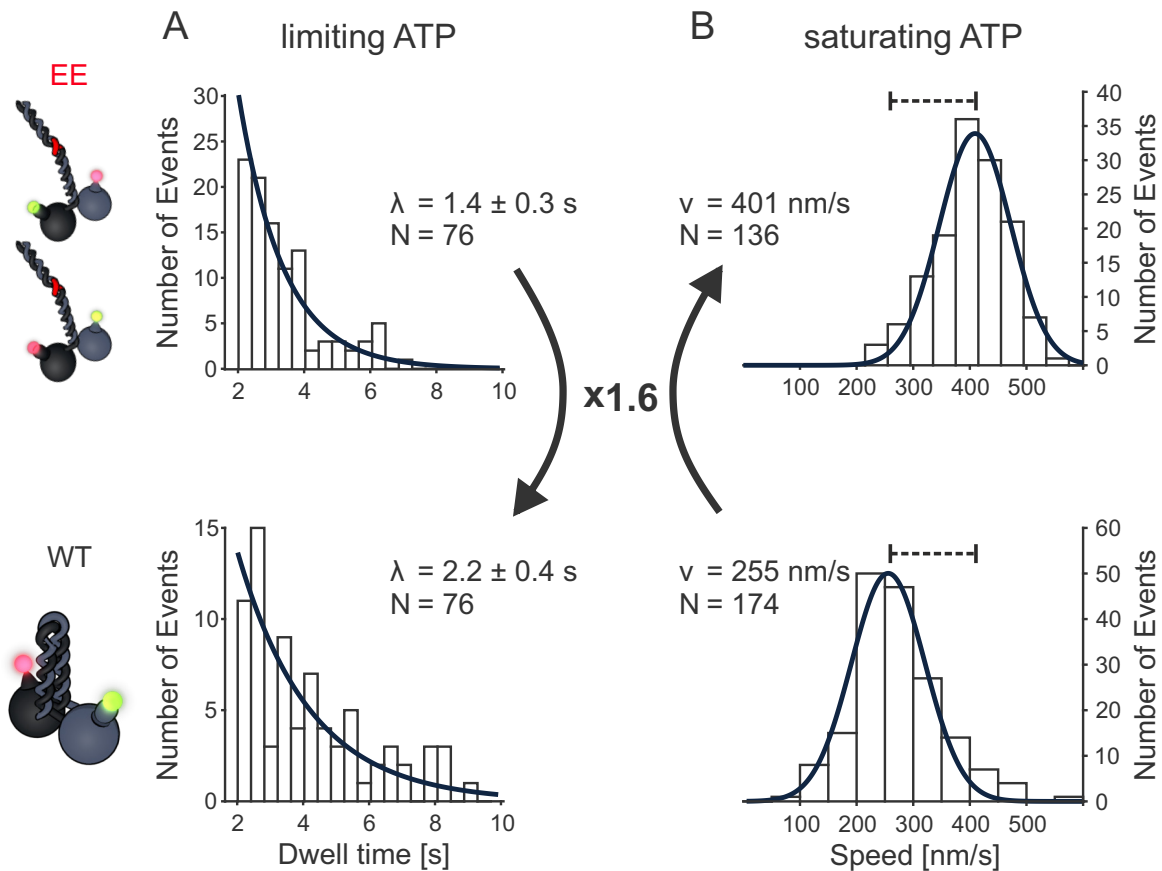
Figure 2.10: Stepping of KLP11 is more suppressed in the full-length wild type motor

A Truncated dwell times longer than 2 s of KLP11 fitted with a single exponential model (data from Figure 2.8). The ratio of the dwell times from wtKLP11 (bottom, 2.2 s) to the eeKLP11 mutation (top, 1.4 s) is 1.6.
B Speeds of eeKLP11/20 ($\mu = 90\,\mathrm{nm\,s^{-1}}$) and wtKLP11/20 ($\mu = 64\,\mathrm{nm\,s^{-1}}$) at saturating ATP concentrations. The ratio of speeds (eeKLP11/20 $401\,\mathrm{nm\,s^{-1}}$ vs wtKLP11/20 $255\,\mathrm{nm\,s^{-1}}$) is the reversed value of the ratio of dwell times. As the ADP release rate is the rate-limiting step at saturating ATP concentrations, the difference in speeds can be explained by the difference in KLP11 dwell times alone.

KLP20 subunits, long dwell times were extracted ($> 2\,\mathrm{s}$) from the KLP11 distributions from Figure 2.8 and refitted them with a single exponential model (Figure 2.10A). For the wtKLP11/20 motor, the resulting dwell time parameter is increased 1.6-fold when compared to the eeKLP11/20 that contains the ATPase activating mutations in the stalk. This difference is in fact consistent with the decreased speed of the wild type motor at saturating ATP concentrations (Figure 2.10B) [19].
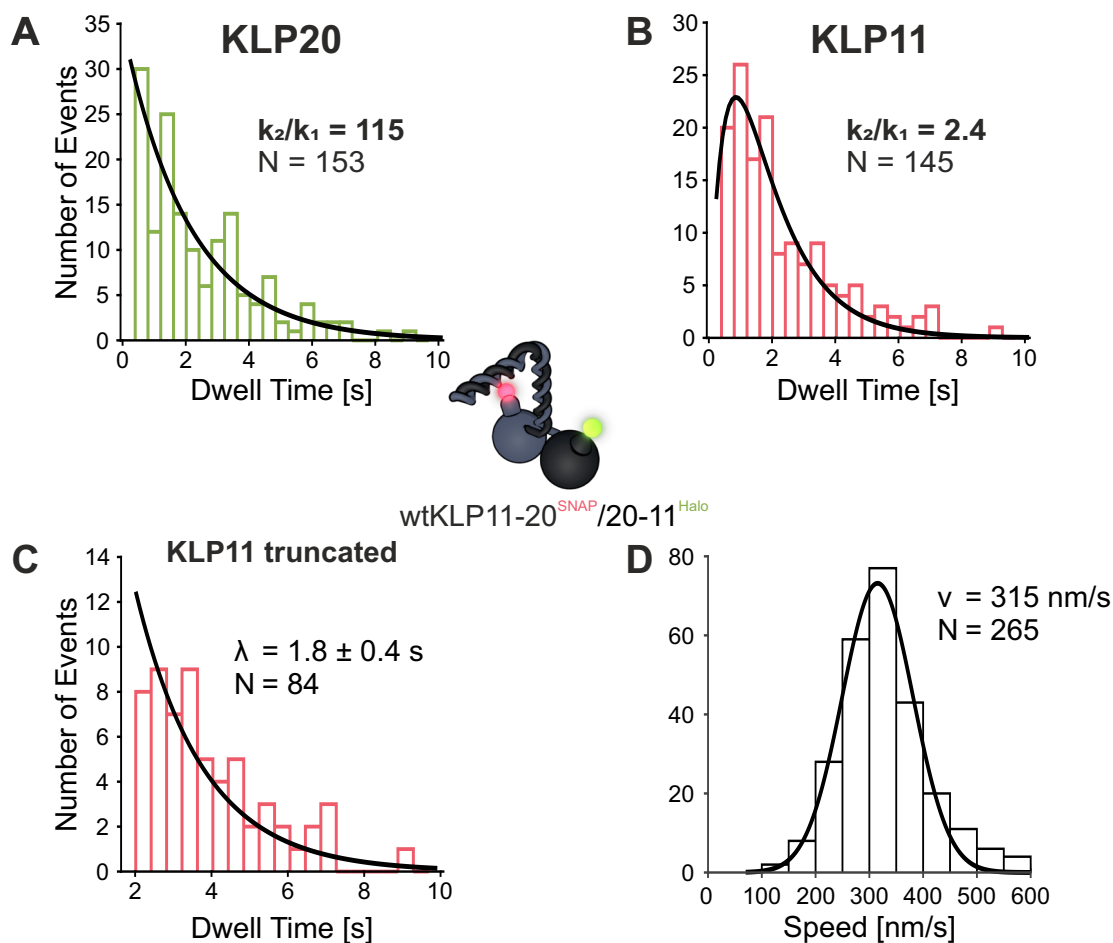
Figure 2.11: Data for a construct with switched head positions confirms the asymmetric nature of the inhibition mechanism by selectively shortening the dwell times of the KLP11 head domain

A & B The KLP20 dwell time distribution is fit well by a single exponential distribution, while the distribution for KLP11 is improved by a second rate-constant in a convolution of two exponentials (see also Suppl. Figure 5).

C & D Our lab previously showed that the auto-inhibition of this motor is dependent on the position of the heads. This now can directly be observed in comparison to the wild-type in both the shorter dwell time of the KLP11 head (C) at limiting ATP conditions and the faster speed (D) at saturating ATP conditions. These values ($\lambda = 1.77\,\mathrm{s}$ and $v = 315\,\mathrm{nm\,s^{-1}}$) scale with the same factor of 1.24 to the wild-type ($\lambda_{\mathrm{wt}} = 2.2\,\mathrm{s}$ and $v_{\mathrm{wt}} = 255\,\mathrm{nm\,s^{-1}}$) showing the enhanced activity of the construct at different ATP concentrations. This also confirms the asymmetric mechanism of the auto-inhibition. As all components for the auto-inhibition are present and the stalk can fold, but the inhibition can be partly relieved just by switching the positions of the heads.

If the increased dwell time of the KLP11 head domain indeed results from an asymmetric inhibition by the stalk/tail, switching the position of the KLP11 head with the KLP20

alone would be expected to also shorten the dwell times of the KLP11. Strikingly, despite the presence of the wild-type stalk/tail, swapping the positions of the KLP11 and KLP20 heads indeed sufficed to reduce the dwell time of the KLP11 head domain (Figure 2.12) [26, 49]. Specifically, previous ATPase and filament gliding experiments showed the activity of the wtKLP11-20/20-11 construct to be roughly between the wtKLP11/20 and the eeKLP11/20. Dwell times and velocities of wtKLP11-20/20-11 and wtKLP11/20 were compared as previously for the eeKLP11/20. Consistent with the finding that it shows intermediate activity in ATPase assays, the activity ratios compared to the wtKLP11/20 for both speed and KLP11 dwell time are 1.24, higher than the wtKLP11/20 but below the values for the eeKLP11/20 (Figure 2.10 and Figure 2.12).

We think that the same modulation in the head-tail interaction is responsible for the observed differences at both limiting and saturating ATP concentrations. This manifests in shorter dwell times and higher speeds for the mutated motors (eeKLP11/20 and wtKLP11-20/20-11) compared to the wtKLP11/20. An influence of the head-tail interaction on the ADP release time in the ATP-hydrolysis cycle could explain both effects. The rate constant present in both distributions is attributed to the ATP-waiting time at low ATP concentrations [7]. Speculating based on previous data, the other rate constant in the dwell time distribution of the KLP11 subunit could result from the tail-suppressed ADP release [20, 22, 23]. This effect is strong in the wild type motor, in which the flexible hinge in the stalk enables auto-inhibitory folding and consequently enhances the head-tail interaction (Figure 2.6A, bottom panel). When the stalk is mutated to prevent auto-inhibitory folding (Figure 2.6A, top panel) or the heads are switched (Supplementary Figure 2.12), the head-tail interaction is hampered, thus shortening the dwell times. My results thus directly show the influence of the tail on the head and the asymmetric nature of auto-inhibition in a physiological kinesin-2 motor. At saturating ATP concentrations, i.e. ATP-waiting time is negligible, the ADP release is the rate-limiting step in the ATPase cycle [92]. The difference in stepping of the constructs alone would then explain the observed speed differences (Figure 2.10 and 2.12).

The asymmetric impact of the tail on the KLP11 but not on the KLP20 head is consistent with our previous findings in bulk ATPase assays. Specifically, the presence of the KLP11 head domain and its relative position within the heterodimeric KLP11/20 was crucial to achieve the auto-inhibited state suggesting an "asymmetric" inhibition model [26]. The response of the KLP11 subunit to the presumed differences in the distinct stalk conformations as unmasked here at the single molecule level would indeed be consistent
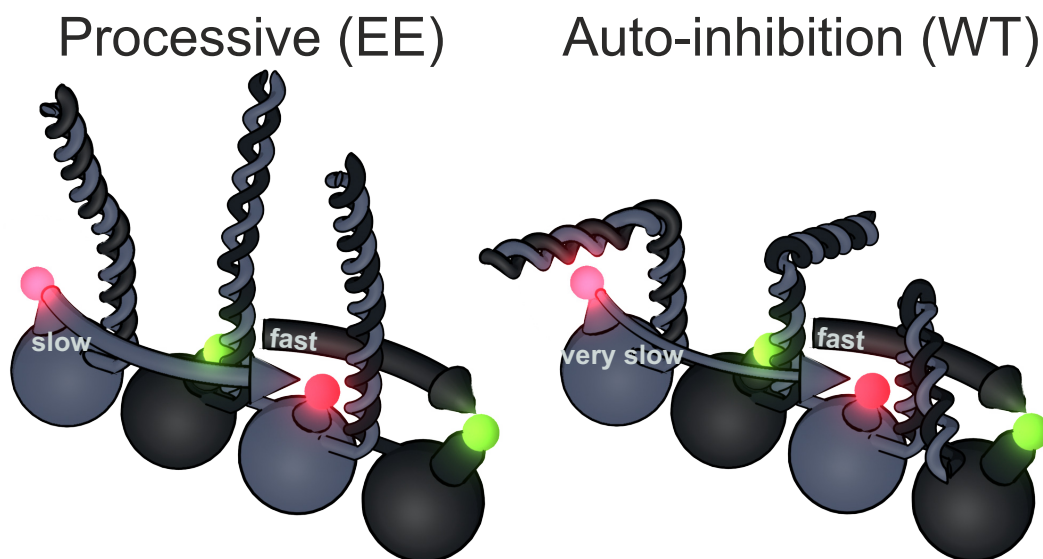
Figure 2.12: The different heads in KLP11/20 step with different dwell times. The auto-inhibition mechanism is asymmetric and influences the KLP11 head predominently.

with this "asymmetric" inhibition. It will be interesting to see whether the conceptual design of kinesin-2 motors underlies such inhibition, or whether this is a specific property of the *C. elegans* KLP11/20.

2.3.4 Summary

This chapter shows the first dual-color super-resolution tracking data for a kinesin motor. By separating the dwell times for the two different heads, it could be shown, that one motor shows an intrinsically different timing of its steps. The observation of modulation of the stepping parameters in proteins with different tails speaks for a direct influence of the tail on the KLP11 head. This is the most direct proof of both an asymmetric auto-inhibition mechanism and limping in a physiologically relevant heterodimeric motor to date.

2.4 Theoretical stepping model for sidestepping kinesin motors

It is well established that kinesin-1 moves on microtubules according to the hand-over-hand stepping mechanism by swinging the trailing head domain forward, ahead of the other, by ~16 nm [7, 93]. These steps occur exclusively along one protofilament, restricting the kinesin-1 motor to a straight path on the microtubule lattice in vitro [93, 94]. In stark contrast to kinesin-1, beads coated with multiple kinesin-2 motors spiraled around microtubules with a characteristic, left-handed pitch, suggesting that single kinesin-2 motors may possess an intrinsic propensity to switch protofilaments [33]. Indeed, a single, truncated kinesin-2 motor from mouse was shown to take sidesteps on the microtubule lattice when it encountered road blocks in vitro [28, 35].

2.4.1 The influence of protofilament switching on FIONA stepping data

FIONA as performed here gives only two-dimensional data in the plane of the cover-slip. However, especially the microtubule offers binding sites that are arranged on a three-dimensional cylinder. In order to understand how these steps in 3D translate to the two-dimensional FIONA data, a MATLAB script that translates kinesin head positions on a microtubule to data that would be obtained from a FIONA experiment was developed here. This work was inspired by the model used by our lab in [33] and described in more detail in [95]. Interesting data, that is now published in part in [96], was provided by Allison Gicking (Figure 2.13A & 2.14A) for the motor PAKRP2. As this kinesin can not be assigned to one of the specified kinesin families it is called a 'orphan' kinesin. It is thought to be employed in vesicle transport in *Arabidopsis thaliana* for cell plate formation. The data was measured using high-resolution nanoparticle tracking that yields similar data as the FIONA technique. In her study, A. Gicking shows that the motor exhibits a non-canonical stepping behavior including protofilament switches, backsteps and waiting positions during a step. This results in a step size distribution with some distinct features. The goal of the development was to reproduce these features with a stepping mechanism based on heuristic stepping probabilities. An early version of this algorithm has been used in chapter 2.5 and [28], but the final version that has not been described in detail so far is featured in this chapter.
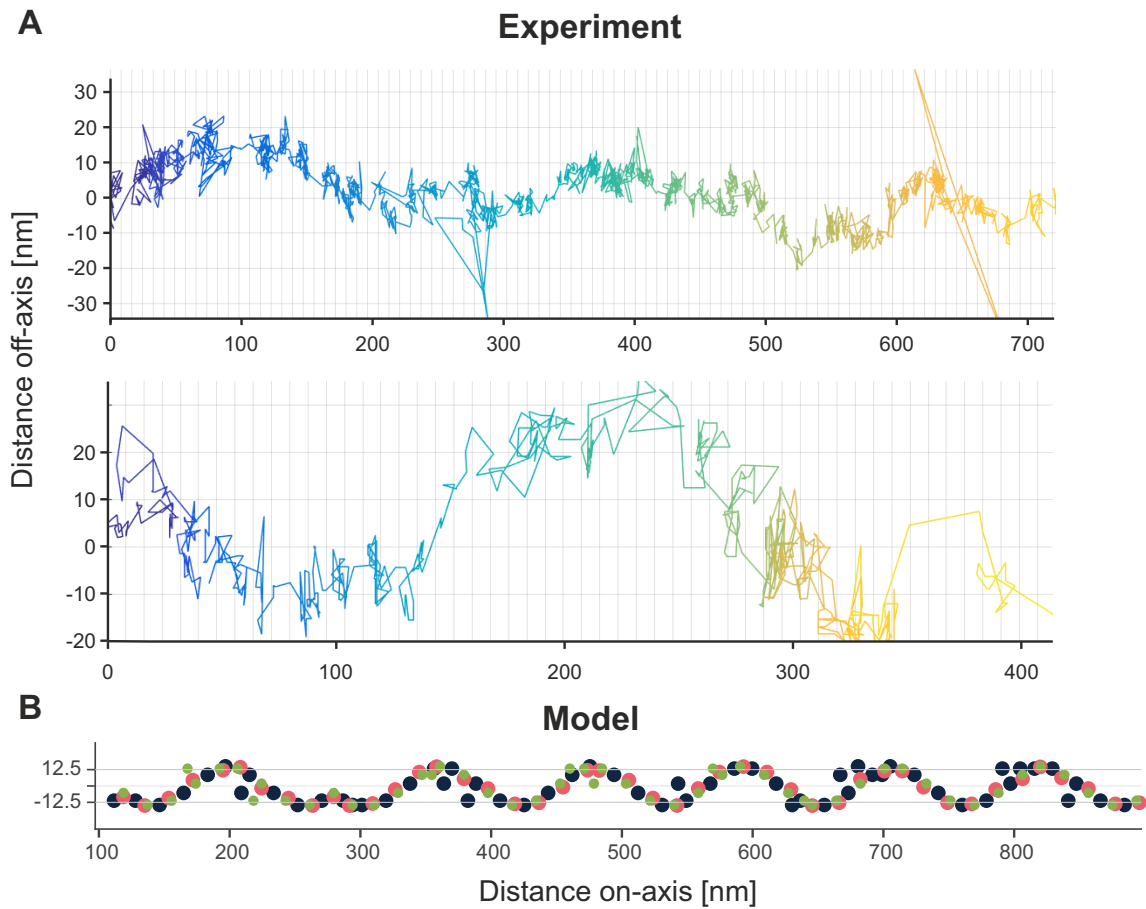
Figure 2.13: Measured traces are recapitulated closely by the performed simulations
A Positions from the nanoparticle tracking experiment plotted in two dimensions and color-coded for time. Apparent curvature hints to several successive steps into the same direction [96].
B Trace that results from 3D positions during a run of the algorithm that have been collapsed in one of the coordinates perpendicular to the filament axis. The shape of the experimental data is reproduced in both the pitch and the amplitude of the sinusoid-like curve. Features like the short inconsistency of the sinusoid at position 280 in the simulated lower trace (a short sequence of differently oriented steps that lead to a 'bump') can also be seen in the upper experimental trace at position 550

2.4.2 From an alternating stepping mechanism to the recapitulation of 2D data

The algorithm is based on an array that describes 3D positions of binding sites on a microtubule lattice according to [67]. Always two of these binding sites are registered as

occupied by the two heads of a motor. The coordinates of these positions are described in two dimensions with one coordinate (0 to 12) describing the respective protofilament and thus basically an angle on the cylinder of the microtubule. The protofilament parameter is therefore calculated as modulo 12, quasi wrapping around the tubular shape of the microtubule. The second coordinate describes the distance along the filament in tubulin doublets. The position is offset by ~1 nm per protofilament in order to reproduce the 'skewed' lattice.

Starting from a position for the two heads and according to the alternating stepping mechanism, the trailing head will re-position. The new binding site for the head is determined from a probability distribution in both dimensions. The protofilament can be switched left (1), right (−1) or kept (0) and the filament direction can be either forward (1) or backward (−2). With the reference point always being the static head position. A probability distribution is chosen for each coordinate separately. An additional parameter 'locks' the protofilament direction with a certain probability from step to step. All values are in respect to the static head. For kinesins with long necklinkers, bigger displacements might be possible.

After a forward step, the formerly static head becomes the trailing head and will perform the next step (Figure 2.6A). This procedure is repeated for a predefined number of steps and all positions of the heads are recorded. The coordinates of protofilament and filament-axis positions can then be translated to coordinates in the three dimensional space by transformation to the 3D positions on the respective microtubule lattice.

The super-resolved positions from the FIONA and nanoparticle measurements are only available in the cover-slip plane, not in 3D. In order to translate the positions from the algorithm to microscope-like data, one of the coordinates perpendicular to the filament axis is projected to the plane of the other one. This results in data that is similar to perfectly resolved super resolution positions from stepping motors. To obtain step sizes, the same algorithm can be performed on the simulated data as would be on the fitted positions from experiments. There are some important effects of this projection on the results of the step detection. A step that happens on the top of the microtubule will retain its characteristics. A step on the 'side' of the microtubule however, will lose part of its component perpendicular to the microtubule axis. As steps to the side can happen both on top and on the bottom of the microtubule, the direction of the step (left/right) can't be concluded from its direction in the FIONA data. A step to the right on top of the microtubule will go in the opposite direction if observed at the bottom of the microtubule.

As the algorithm has limited sensitivity for steps in noisy data, an empirical detection probability function 2.20 is introduced that limits the detection of small steps. Parameters are the measured step size x and the probability p to transfer the step size to the step size histogram.

$$p_{detection} = 1 - \frac{1}{0.6\sqrt{2\pi}}e^{-\frac{x^2}{8}} \tag{2.20}$$

In order to account for experimental inaccuracies, the step size distributions are broadened with a gaussian profile with exponential parameter of 1.8 nm.

2.4.3 A set of starting parameters that result from the PAKRP2 step size data

The orphan kinesin PAKRP2 shows some distinct features in its step size distribution (Figure 2.13A & 2.14A). A special feature that was detected in the 2D data was the existence of a short-lived position that was interpreted as a 'waiting position' during the step of a head [96]. This feature was included in the algorithm by calculating a waiting position between the pre- an post-step positions with a minimum distance to the static head. With these adjustments, a set of probability parameters for the algorithm was chosen heuristically in order to fit the experimental data. The negative step sizes are reflected in a filament-axis probability distribution of 0.8 forward and 0.2 backward. The main peak of the positive step sizes that is at closer to 8 nm than the protofilament-tracking 16 nm is reflected in a high probability for sidesteps (right: 0.1, straight: 0.2, left: 0.7). The special form of the traces that resembles a projected helix is obtained by a direction repetition parameter of 0.8. With these parameters, the algorithm yields data that recapitulates the experimental data in great detail (Figure 2.13B & 2.14B).

2.4.4 Summary

A framework is developed in this chapter to link details of the stepping mechanism of molecular motors to their stepping parameters measured by step detection experiments. It was shown, that more complex stepping mechanisms have to be implemented in order to explain the data obtained for non-canonical motors like kinesin-2 or PAKRP2. Step sizes, their distributions and the corresponding paths could be linked to the stepping mechanism for these motors for the first time.
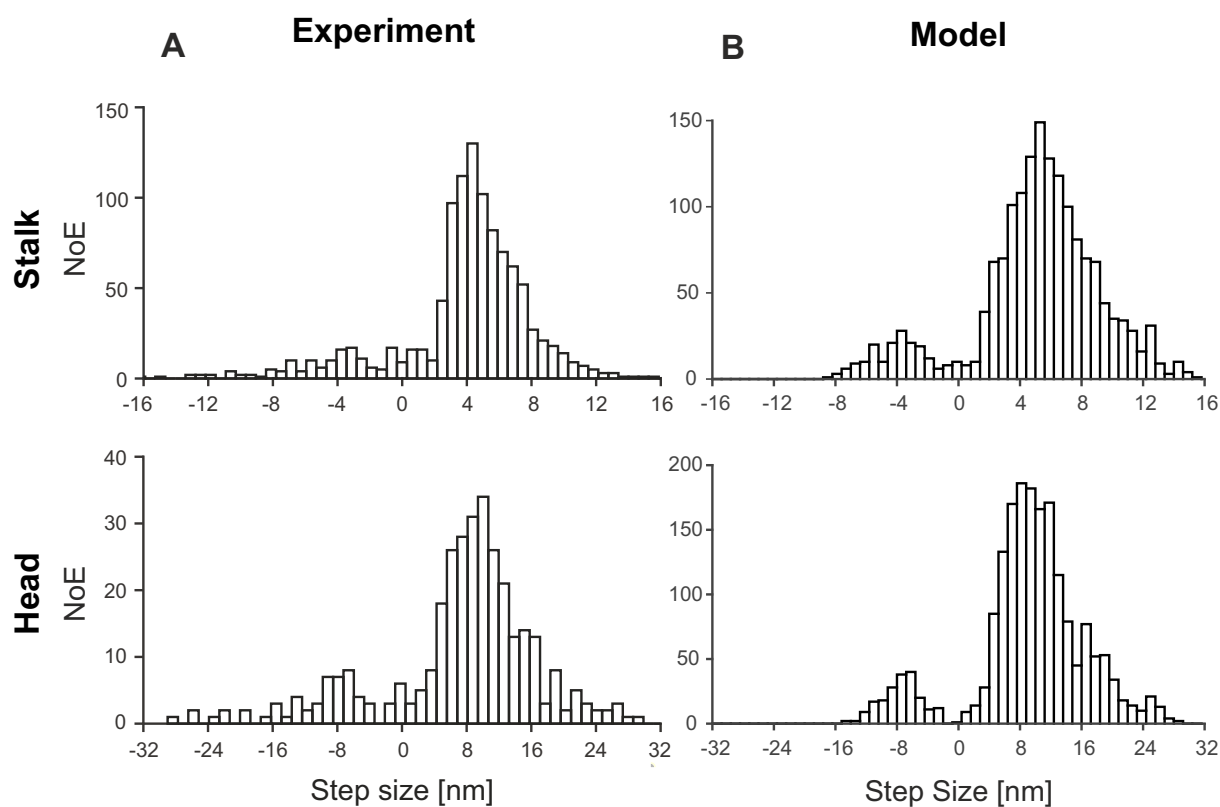
Figure 2.14: With the chosen parameters, the algorithm recapitulates the experimental data well

**A** Step size distributions from the nanoparticle tracking experiment [96].

B Step size distributions for on-axis movement of theoretical stalk- and head-labeled constructs. All the features of the experimental distributions are present in quality and relative quantity in the data produced by the algorithm.

Parameters:

left 0.7, straight 0.2, right 0.1 | direction repetition 0.8 | forward 0.8, backward 0.2

2.5 Kinesin-2 motors adapt their stepping on microtubules and axonemes

Kinesin-2 motors have another intriguing specialty, apart from their heteromeric family members and their propensity to take sidesteps. Most kinesin-2 motors are employed in intraflagellar transport and are thus active on the special ciliary filament called axoneme. The stepping behavior and traces of kinesin-2 motors when walking on microtubules versus axonemes were compared using data obtained from FIONA experiments. In doing so, interesting differences that explain how kinesin-2 motors are organized for optimal efficiency of IFT were discovered. Most of this work has been published in [28] and parts of the publication are cited here literally.
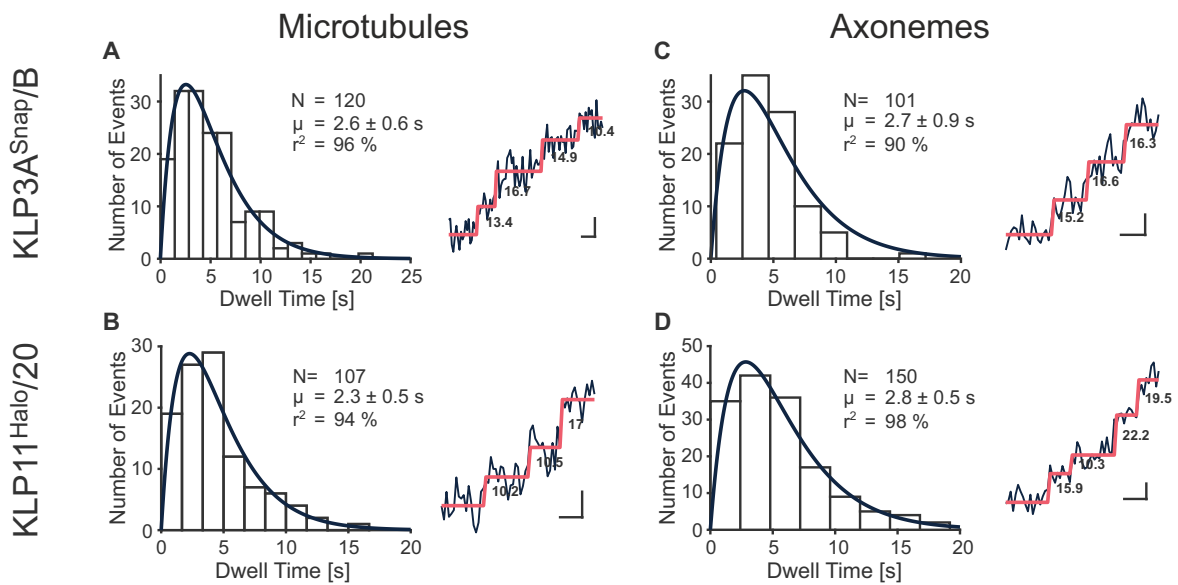
Figure 2.15: Dwell time distributions for one-head-labeled motors are distributed according to a double exponential distribution
Double-exponential decay of the dwell times and raw stepping data with detected steps.
Double-exponential decay of the dwell times again argues for a hand-over-hand stepping mechanism on axonemes.
Steps are shown with the detected stepping pattern in red and the calculated step size in nm.
Scale bars are 5.04 s (10 frames) wide and 10 nm high.

2.5.1 Single kinesin-2 motors show different step sizes on microtubules and axonemes

The motor KLP3A/B is an exception among kinesin-2 motors, as it is active on microtubules for melanosome transport in *X. laevis*. It was used here alongside the already introduced KLP11/20 in order to test the behavior of motors that are employed in different settings in vivo. As mentioned in 2.4, kinesin-2 motors are both known to take sidesteps as single motors and to spiral around microtubules when active in groups. Whether single motors also spiral around their filament and how this changes for the special geometry of axonemes was not known.

In order to test this, N-terminally fluorophore-labeled KLP11 and KLP3A subunits in the heterodimeric motors were tracked with nanometer resolution. Again, using Halo- and SNAP-tags, labeling of the head domains succeeded with good specificity (Supplementary Figure 5.4).

Bleaching analysis confirmed, that only single motor molecules were observed. Therefore, extended time series (>5 min) of surface attached motors were recorded. The fluorescent signal of one peak was checked for bleaching steps and the number of steps was plotted in a histogram. The strong predominance of only one bleaching step that is detected shows that the data was measured on single molecules (Supplementary Figure 2.16). As detailed in 2.3.2, a double exponential distribution is expected for the dwell times of a molecular motor labeled at only one head. The step of the second head has to occur before the first head can step again, thus resulting in a convolution of exponentials. This is what was observed in all geometries used (Figure 2.15).
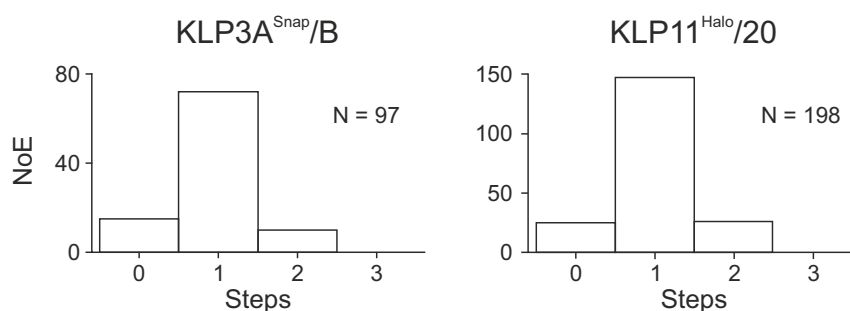
**Figure 2.16: Photo-bleaching confirms measurements on single molecules**
Photo-bleaching analysis displayed predominantly single bleaching steps. The fluorescent spots for analysis were chosen by intensity and the intensity values for a 3x3 pixel window were summarized. Performing a gliding-t-value test with a corresponding threshold identified the bleaching steps.

The respective step sizes of the KLP11/20 and KLP3A/B motors centered around ~13 nm
(KLP3A/B: 13.5 nm, KLP11/20: 13.4 nm) on microtubules and thus significantly devi-
ated from kinesin-1's ~16 nm on-axis steps (Figures 2.17A & B and 2.18) [7, 93]. The
step sizes of ~13 nm of KLP11/20 were also confirmed by dual-color experiments (Sup-
plementary Figure 5.6).

A ~13 nm displacement is inconsistent with protofilament tracking because it does not
reflect the ~8 nm periodicity of the microtubule. Instead, these results implicate that the
two kinesin-2 motors take sidesteps to the neighboring protofilaments (Figure 2.18).
The respective step sizes are consistent with a hand-over-hand mechanism, as is the double-
exponential decay of the observed dwell times. The dwell time distribution indicates the
existence of two substeps, one from the fluorescently labeled and the other from the unla-
beled and thus "hidden" head (Figure 2.15A & B) [6, 7].
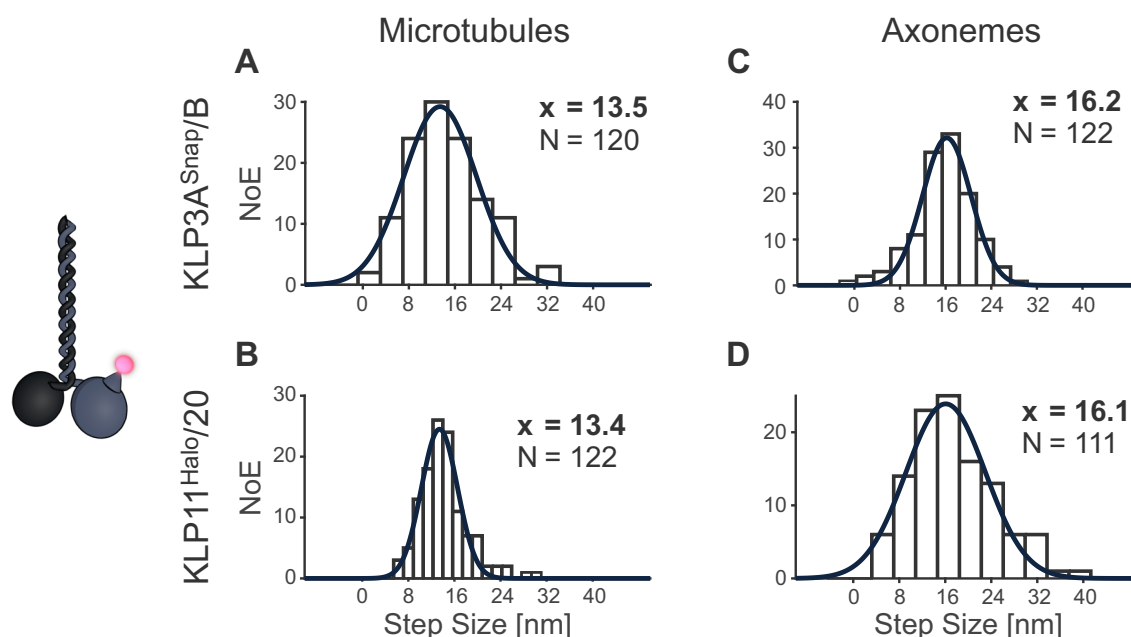
**Figure 2.17: Kinesin-2 motors differentiate between the microtubule and axoneme
surface to take processive steps**
A & B The step size distribution centered around ~13 nm when walking on microtubules. This
hints to the occurrence of steps to neighboring protofilaments that are expected to be ~10 nm in
size. A combination of protofilament-tracking and switching steps would result in the observed
step size distribution.
C & D Tracking on axonemes increased step size distribution to ~16 nm which is consistent
with protofilament tracking.
The respective step sizes distributions are fit to a normal distribution (x is mean, widths are A:
9 nm, B: 4.4 nm, C: 6 nm, D: 9.8 nm) See Supplementary Figure 5.5 for example traces.
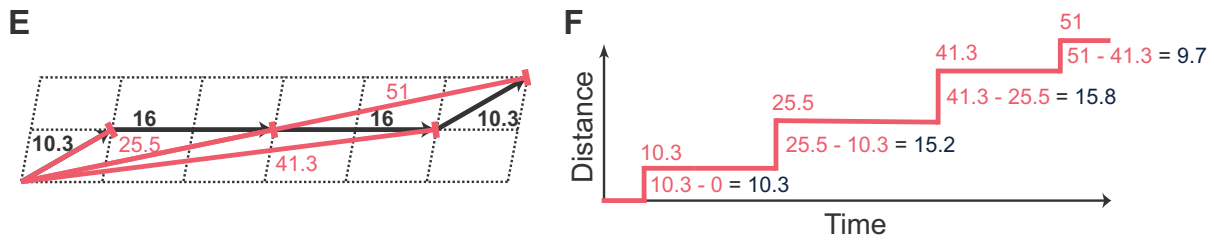
Figure 2.18: Overview of the tracking procedure of a single kinesin-2 head taking steps and switching the protofilament on the microtubule
A The displacements of the kinesin head are depicted as black arrows with the corresponding distances in black (all distances are given in nm). The red bars show the distance measured to the original head position with the step tracking algorithm.
B Resulting step detection from A. Step sizes are calculated from the distances of plateaus in the stepping data. This leads to a measured step size that is smaller than the real displacement (blue numbers). This contributes to the spread of measured step sizes in the data.

This leads to the conclusion that individual KLP11/20 and KLP3A/B kinesin-2 motors possess an inherent propensity to take sidesteps to the neighboring protofilament as previously suggested from multiple-motor assays [33]. Next, it was assessed whether KLP11/20 and KLP3A/B motors walk differently on axonemes than on single microtubules. Remarkably, the mean displacements of individual motors increased from ~13 to ~16 nm when allowed to walk on axonemes (Figure 2.17C & D). This step size is consistent with efficient on-axis protofilament tracking and a hand-over-hand stepping mechanism. The dwell time distribution again displayed a double-exponential decay for both motors on axonemes further supporting a hand-over-hand stepping mechanism (Figure 2.15C & D).

2.5.2 Large scale dynamics confirm adaptation to filament

The observed stepping behavior implicates that single kinesin-2 molecules have an intrinsic propensity to take sidesteps by switching protofilaments on singlet microtubules; on axonemes, however, they faithfully track one protofilament following a straight path. If true, these respective stepping modes should be reflected in the trajectories of the motors moving on microtubules versus axonemes. Following KLP11/20 over time on axonemes indeed resulted in straight trajectories consistent with the 16 nm on-axis displacements (Figure 2.19B). In contrast, on singlet microtubules with rotational symmetry, the motors followed sinusoid-like paths consistent with sidestepping (Figure 2.19A). These correspond to the projection of a helical motion of an individual motor around the tube-

shaped microtubule lattice.
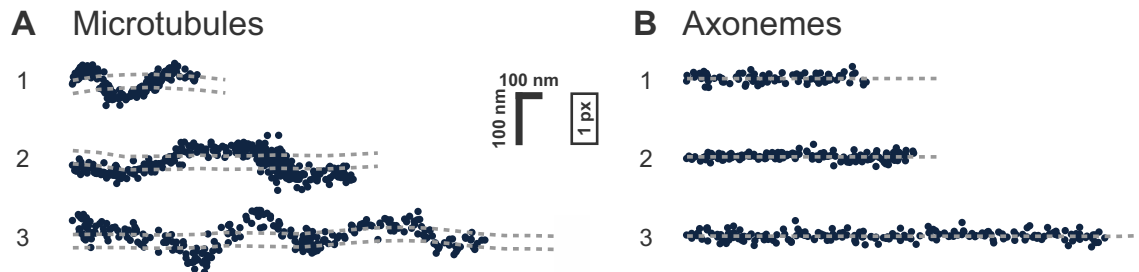
Figure 2.19: Large scale traces confirm the motors adaption to filament
Tracking of the fluorescently labeled head domains KLP3A and KLP11 of the heterodimeric kinesin-2 motors for several micrometers at low ATP concentrations.
A On the rotationally symmetric microtubule filaments, the motors show a sinusoidal trajectory, corresponding to a periodic helical path around the symmetry axis of the filament.
**B** The axoneme is lacking this symmetry due to the combination of the A- and B-tubules into a doublet microtubule along with the interconnection between the respective doublet tubules. Without a symmetry axis, the periodic path is lost and the motor is restricted to a straight path.
The dashed lines underlining the respective trajectories have been obtained from a sub-pixel detection of filament positions.

While it might not be intuitive, how the motors can spiral around a surface-attached microtubule, a look at the attachment setup provides clarity (Figure 2.20). The biotinylated microtubule is attached to the cover-slip using a biotin-BSA/streptavidin setup. As the streptavidin is ~10 nm in size, the motor heads and the elongated tail can pass between the microtubule and the BSA surface. The stiffness of the microtubule also ensures a relatively stable separation between the microtubule and the cover-slip. At a closer look, the traces for microtubules might show instances, where the passage below the microtubule is hindered by its closeness to the cover-slip and the motor walks some straight steps instead of spiraling (Figure 2.19B). This observation also matches with the observation, that kinesin normally lifts its cargo ~17 nm above the microtubule [97].
An early version of the algorithm described in 2.4 was used to test the connection between the step sizes and the traces. In fact, the sole assumption of a 50 % probability of sidestepping was sufficient to recapitulate the experimentally determined step size of the motor (Figures 2.21, and 2.17A & B). Remarkably, this assumption alone sufficed to also recapitulate the motors characteristic trajectories observed above (Figures 2.21 and 2.19A). Taken together, these results strongly argue for an adaption of the motor's trajectory dependent on the respective track employed.
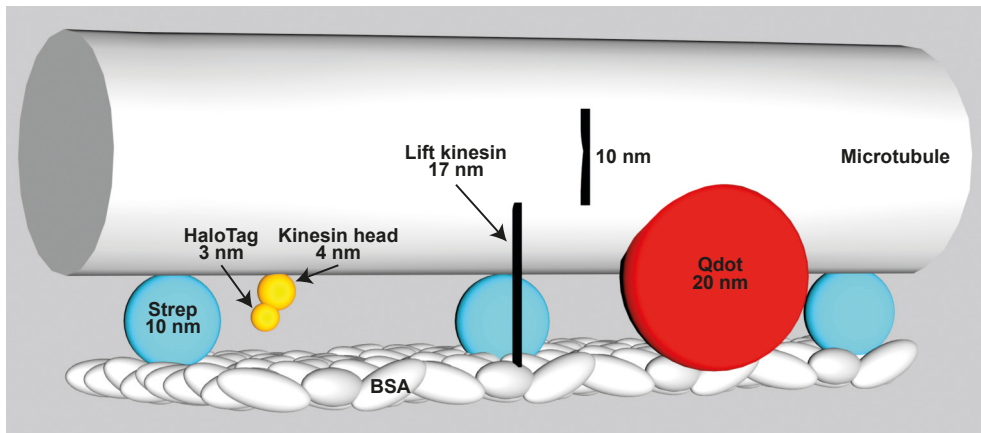
Figure 2.20: Geometry of Biotin/Streptavidin bound microtubules to the cover-slip surface. The kinesin head together with the HaloTag fit well between the microtubule and the cover-slip. With the wild-type tail, kinesin-1 lifts cargo 17 nm from the filament [97]. Considering a flexible tail, kinesin does have the space to follow a helical motion around the microtubule. For previous experiments that used microspheres or Qdots for labeling, a possibility of passage is not expected due to the size of the tags [7].

2.5.3   Kinesin-2 behavior on axonemes and microtubules explains IFT organization

Why do the motor's stepping patterns differ on the two respective tracks? The nine peripheral microtubule doublets of the axoneme are connected among others via densely packed nexin and dynein arms [68, 71, 72, 98, 99]. This suggests that kinesin-2's inherent ability to side-track on the microtubule lattice (Figure 2.21) in a left-handed manner [33] will eventually restrict the motor next to these impenetrable structural demarcations on the axoneme surface forcing the motor to take on-axis ~16 nm steps (Figure 2.22). This process ensures that all kinesin-2-powered intraflagellar trains segregate to one side of the doublet microtubule, the B-tubule, during anterograde transport, clearing the A-tubule for retrograde dynein transport [73]. Kinesin-1, in contrast, would fail to segregate to one of the two tubules and 50 % of the motors would populate the A-tubule, hindering retrograde transport due to its inability to directionally switch protofilaments [7, 33, 36, 94]. Instead, it would walk straight ahead and eventually collide with dynein-powered trains coming from the tip of the cilium. My results therefore offer a simple mechanistic explanation for how step adaptation of kinesin-2 motors enables collision-free bi-directional transport on axonemes in the cilium [73]. Dynein-2, like kinesin-2, may also exhibit an intrinsic left-handed bias during retrograde transport toward the base of the cilium (Figure 2.22). In doing so, it would efficiently avoid collisions with kinesin-2 powered trains
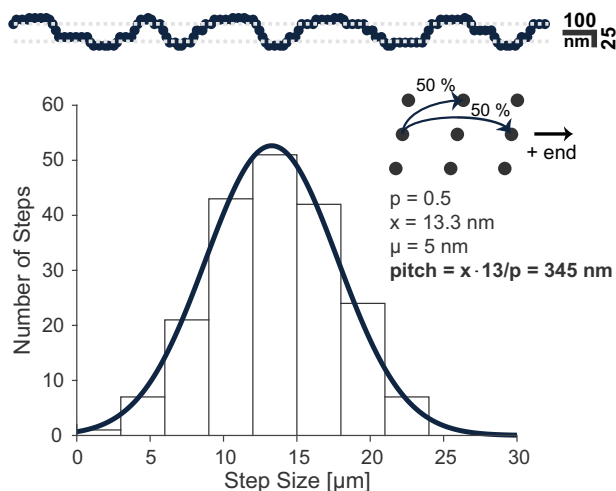
Figure 2.21: Trajectory and step size distribution both result from sidestepping
The stepping of a motor was modeled on a cylinder-shaped microtubule lattice [67]. A sidestepping probability of 50 % was assumed and 200 steps were simulated. The data was projected onto a plane to simulate a microscope image. For the histogram, step sizes were blurred by a Gaussian distribution of width 3 nm corresponding to the estimated detection accuracy. The pitch for a 13 protofilament microtubule is calculated from the mean step size (x) and the probability for sidesteps (p).

by spatially partitioning them to the opposite side of the doublet microtubule. Taken together, this work provides first mechanistic insights into why heterodimeric kinesin-2 has specifically co-evolved with the IFT machinery to work on axonemes [4, 100, 101].

2.5.4 Summary

Using FIONA to detect the steps of kinesin-2 for the first time, this chapter shows that this motor steps in a hand-over-hand mechanism. A difference in the stepping parameters shows a difference of the mechanism for microtubules and axonemes. This difference could also be shown in the paths taken on the difference filaments. By translation of these observations to the physiological situation, it was possible to explain the mechanism of traffic organization in IFT for the first time.
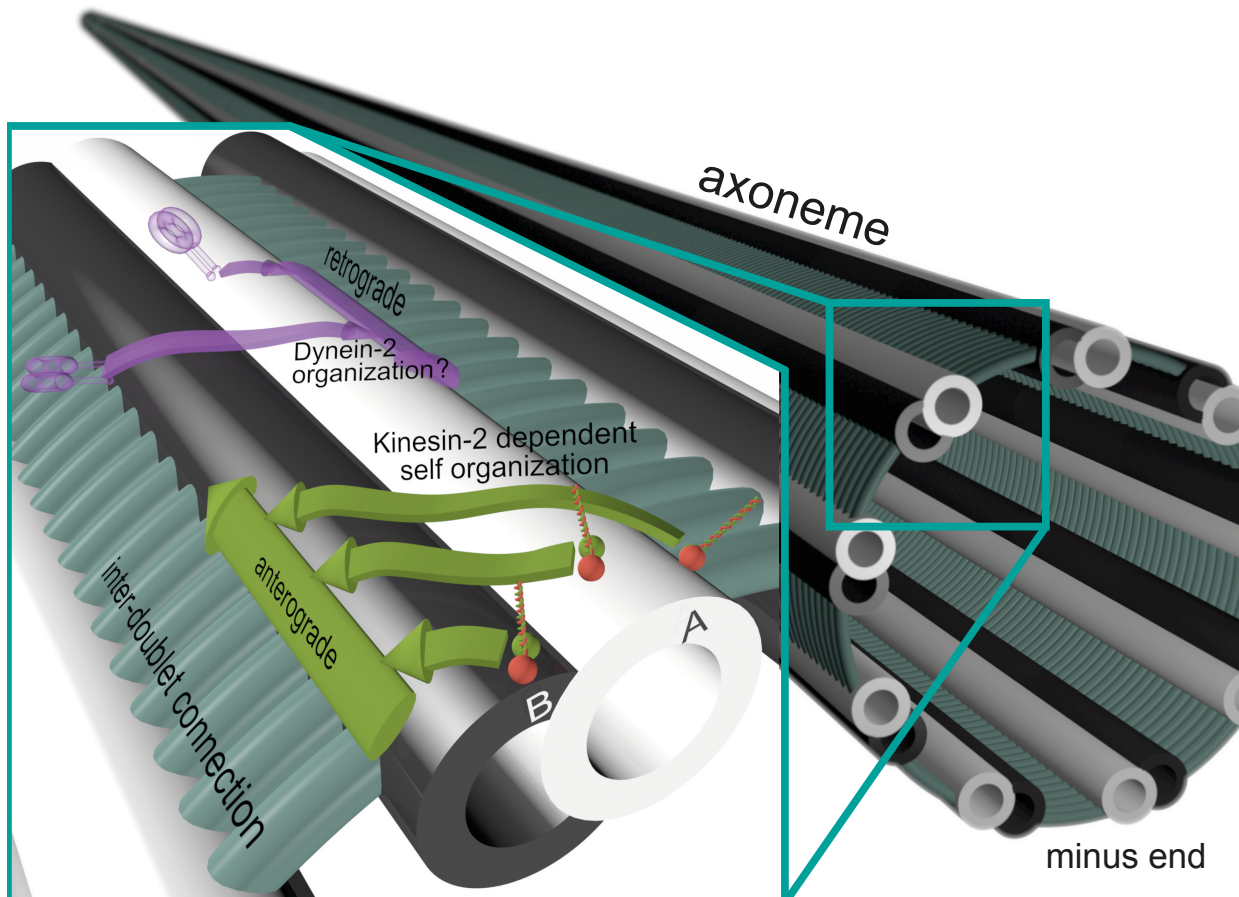
Figure 2.22: Proposed model for two-way traffic on a single microtubule doublet
The organization of large intraflagellar trains for a collision-free bi-directional transport on a single microtubule doublet within such a spatially restricted environment as seen in vivo poses a remarkable challenge. With the inter-doublet connections acting as a structural barrier, the motors' intrinsic ability to switch protofilaments to the left [33, 34] would allow a collision-free two-way traffic by separating the large intraflagellar trains to either side of the doublet microtubule. This model may explain why nature has not recycled any other efficient transporter as kinesin-1 but opted to co-evolve heterodimeric kinesin-2 motors with an intrinsic left-handedness. Whether dynein-2 displays an exclusive left-handedness is, however, not yet known.

Chapter 3

Prospects and Outlook

In this thesis, the dual-color FIONA technique for kinesin-2 motors was introduced and established. A custom built setup was implemented for multi-color high resolution tracking of molecular motors. The setup was shown to be able to track kinesin steps in three colors at the same time. Both FIONA tracking of a wild-type motor and dual-color tracking of a kinesin motor were shown for the first time.

Tracking the ciliary kinesin-2 motor offered insights into the adaptation of molecular motors to their specific environments. From detailed stepping mechanics to the overall organization of IFT. The capability of the setup to also perform triple color FIONA is already shown here. A lot of valuable information can now be obtained, thanks to these established FIONA techniques for heterodimeric kinesin motors. Over the last years we have gathered a lot of information on different kinesin-2s and their cooperation. How this knowledge can be advanced using the now established FIONA techniques for heterodimeric kinesin motors will be discussed here.

The dual color data on KLP11/20 already showed interesting effects of the heteromericity of kinesin-2 motors. However, the exact mechanism of the auto-inhibition that is more effective on the KLP11 could not be shown. This could be achieved by altering the ATP concentration for these experiments. Certainly, the ATP concentration was optimized for step detection at reasonable cycle times for imaging. Achieving reliable step detection at a considerable range of ATP concentrations might therefore prove difficult. For lower ATP concentrations, the motors like to stop moving and limitation arise regarding the stability of the setup. For higher ATP concentrations, the frame rate of the recording would have to be increased, sacrificing some of the accuracy of step detection. Doing this with the wild-type motor might be an even bigger feat, due to its more random activity

behavior that was already observed at the optimized ATP concentrations. But, with the foundations established and the experience from the last experiments, it might still be possible. It could link the effect seen here to a specific event in the ATP hydrolysis cycle of the motor and thus inform about the detailed mechanism of auto-inhibition in a walking motor which has never been possible before.

With data from our lab on the FLA8/10 motor from *C. reinhardtii* showing speeds up to $2\,\mu\mathrm{m\,s^{-1}}$ it is obvious, that the kinesin-2 speeds show a wide variety. As Jon Scholey mentions in [30], this is likely due to differences in the basic stepping mechanism. Analyzing the stepping of different kinesin-2 motors, especially with the dual-color experiment, could unveil these differences. We already know that the motors when working in teams actually support different pitches when spiraling around a microtubule [33]. If it is indeed the case that kinesin-2 motors show different stepping behaviors and maybe also sizes, some of the questions could eventually be answered that could not be solved here. It might be possible to link features in the dwell time and step size distributions to one another in a conclusive way, with the pitch data for the respective motor in the background. The exceptionally fast motors might also employ a slightly different basic walking mechanism to achieve such velocities. One could imagine them to skip binding sites in order to achieve bigger step sizes. This should become apparent in the step size distributions with reliable step detection. To find conditions where these motors show a stepping behavior that is close to their mechanism at saturating ATP conditions could however prove difficult. The implementation of ATP derivatives or the modulation of the viscosity of the essay buffer might have to be adapted here. Also the employment of these motors on different tracks might have an influence on the stepping mechanism. While it was shown that the cytoplasmic KLP3A/B walks with the same step size as the ciliary KLP11/20, it was not possible to assess the dwell times for the individual heads in these experiments. Do the dwell times for the heads differ depending on if they walk on microtubules or axonemes?

The triple-color ability of the setup will come into play when analyzing cooperation of motors. With a lot of work in the last years on how to couple motors to see how they work together, the foundations for these experiments are there. With the possibility to check the stepping of one of the motors in great detail, the third color can be used to observe one of the heads of the second motor concurrently. Using different combinations of motors could reveal a lot of new information not only on the interaction of motors but also on the motors' mechanics themselves.

Do motors coordinate their stepping if linked together? If this is the case, there are different ways it might be achieved. Either via a force-feedback over the link used for combining the motors or via a direct communication of the heads. Using FIONA techniques and variations in the linker, it will be possible to see which mechanism is employed predominantly.

How would this cooperation happen for a combination of a fast and a slow motor? This is the question with the most immediate interest around it. Recent observations from us, William Hancock's lab and others show that two cooperating motors actually walk at an intermediate speed. Theoretical considerations expect mainly an alternating activity model to be at play here. Using FIONA techniques this question could be answered at the experimental level and supply important information and parameters for the theoretical modeling.

Our lab has recently been observing filament switching from actin to microtubules and vice versa on myosin-V. How do these switches happen on the molecular level? Observing a motor at the intersection of two filaments with FIONA precision could reveal some important details about this mechanism.

How does the long discussed bidirectional counter-play of opposite polarity motors work? The very different walking mechanisms of kinesin and dynein have been studied in quite some detail. It is also known, that these two motors can stall movement if put up against each other. With high-resolution data it might be interesting to see, how each motor behaves in a stalled situation due to their different processive stepping behavior.

Chapter 4

Materials and Methods

Parts of this chapter are literal quotes from [28] and [90]. The goal for this chaper is to supply a concise but complete description of the methods used during the work, all in one place.

4.1 DNA constructs and design

The protein studied in this thesis is the heteromeric kinesin-2 KLP11/20 active in the intraflagellar transport in *C. elegans*. Mutations were performed as described previously [33]. Halo- and Snap-tags were fused to the n-terminus of the respective sequences where applicable [102, 103]. Constructs used where

- eeKLP11$^{\text{Halo}}$
- wtKLP11$^{\text{SNAP}}$
- wtKLP11-20$^{\text{SNAP}}$
- eeKLP20
- eeKLP20$^{\text{SNAP}}$
- wtKLP20$^{\text{Halo}}$
- wtKLP20-11$^{\text{Halo}}$

4.2 Protein expression, purification and fluorescent labeling

All proteins were expressed using the Baculovirus Expression System (Thermofisher) in insect cells [Spodoptera frugiperda (Sf9)] according to the manufacturer's instructions.

Heterodimeric motor proteins were Flag-tagged (DYKDDDDK) at one of the C-terminal ends to facilitate purification. The following protocol refers to 50 ml suspension culture at $2 \cdot 10^6$ cells ml^{-1}. For protein purification, virus-infected insect cells were pelleted after 48 h incubation at 28 °C by centrifuging for 10 min at 3500 rpm. Cells were carefully lysed in Lysis Buffer. Lysed cells were pelleted by centrifugation for 10 min at 30 000 rpm. The supernatant was incubated with 50 μl ANTI-Flag M2 Affinity Agarose gel (Sigma) for 90 min. The beads were washed three times with each 1 ml wash buffer 1 and 2. Subsequently, the beads were incubated on a rotator for 40 min at 4 °C with 100 μl wash buffer 2 with 1 mM of the specified SNAP- and Halo-tag ligands. For dual color experiments, the incubation time was increased to 90 min and a mix of the specified dyes in the same amount of buffer was used for labeling both tags simultaneously. The protein was eluted in 100 μl elution buffer for 1 h. This protocol leads to a typical range of protein yields of 0.1 mg ml^{-1} to 0.2 mg ml^{-1}.

4.3   Table of buffers

	Lysis	WB1	WB2	EB	BRB 80	Motility
Pipes	50	80	80	80	80	80
KAc	300	500	200	200		100
MgCl$_2$	1	1	1	1	2	2
EGTA		1	1	1	1	1
ATP	0.1	0.1	0.1	0.1		variable
DTT	1	1	1	1	1	1
Triton-X	0.5%					
Tween20		0.1%				
Flag Peptide				10%		
Glucose						0.4%
Glucoseoxidase						0.15 mg ml^{-1}
Catalase						0.05 mg ml^{-1}
Creatinphosphate						1
CP-kinase						0.1 mg ml^{-1}

All values in mM unless stated otherwise

4.4   Single molecule assays

All experiments were performed on the custom-built setup described in chapter 2.1.

Photobleaching experiments

In order to verify that single molecules were measured in the microscopic assays, bleaching step analysis was performed on all constructs. Kinesin was adsorbed to coverslips via non-specific interactions and fluorescence was observed in TIRF illumination. Spots for analysis were chosen for all constructs by intensity and the intensity values for a 3x3 pixel window were summarized. Performing a gliding-t-value test with a corresponding threshold identified the bleaching steps [104].

Chamber preparation

A flow chamber (5 µl volume) was created by fusing a parafilm cut-out between a slide and a cover slip. The chamber was coated with $1\,mg\,ml^{-1}$ biotinylated BSA, $1\,mg\,ml^{-1}$ streptavidin (Sigma), and biotinylated, fluorescently (Alexa Fluor dyes, Thermofisher) labeled microtubules, with intervening $2\,min$ long incubation and subsequent washing steps using BRB 80 buffer containing $7\,mg\,ml^{-1}$ BSA or Casein. For experiments on axonemes, the filaments were incubated and bound directly to the cover slip, followed by a passivation step using BRB 80 buffer containing BSA or Casein. Finally, a motility buffer containing a desired concentration of motor proteins were perfused into the flow chamber.

Transport parameters at saturating ATP concentrations

Speeds and run length were measured at an ATP concentration of $2\,mM$. Movies were recorded with an exposure time of $200\,ms$ and 500 frames were recorded before changing the position in the sample. The electron-magnifying gain was set to 118 from the first register and data was digitalized at $30\,MHz$ with the 16 bit analogue to digital converter.

Step detection at limiting ATP concentrations

For step detection experiments, the ATP concentration was reduced to $0.4\,µM$, the creatin phosphate/creatin phsopho kinase system guaranteed stable ATP concentrations over the duration of data collection. Movies were recorded with an exposure time of $500\,ms$

for single color and 400 ms for dual color experiments, resulting in cycle times of 505 ms and 405 ms respectively.

4.5 Data analysis

All data analysis was performed using ImageJ and custom routines implemented in Matlab (Mathworks Inc.). The procedure is detailed in 5.9 and I will summerize the most important steps here. Traces for speed and run length measurements were extracted by identifiying and following peaks depending on their brightness. A position with subpixel accuracy for these traces was assigned using a radial center approach [105]. Runs over several frames were connected by following peaks according to their distance to a peak in the previous frame. Overall distances were calculated with respect to the first detected position in a run. Speeds where then calculated by performing a linear regression on the distance over time data and extracting sequences, that fitted with an r-squared value higher than 95%. Run lengths were determined from the maximum distance from the starting point for each run. A closer introduction of this software can be found in chapter 5.9.

For step detection experiments, a least-squares fit procedure was used to fit a Gaussian profile to the peak data with a starting point deduced from the initial detection of the brightest pixel. This fit provided a higher accuracy subpixel position for each frame, compared to the radial center approach. Due to the lower speeds, the distance over time traces show distinct relocation events. The gliding-t value approach was used in order to detect steps for the single color experiments [104]. For the dual color experiments, an implementation of the Potts algorithm was used for step detection [89]. Single position spikes in the distance traces were filtered out. The individual sizes of steps were calculated from the mean distances before and after each step. Dwell times were calculated by calculating the distances between the occurrences of steps.

For dual color experiments, an algorithm was used to extract sequences of alternating steps in both channels. Dwell times were then calculated from the time of a step in one color to the next step in the other color. For the extraction of step directions, the axis of the filament was approximated manually from the position trace of the motor. Directions were then calculated from the angle of the line between two mean x,y-positions before and after a step and the axis of the filament.

Chapter 5
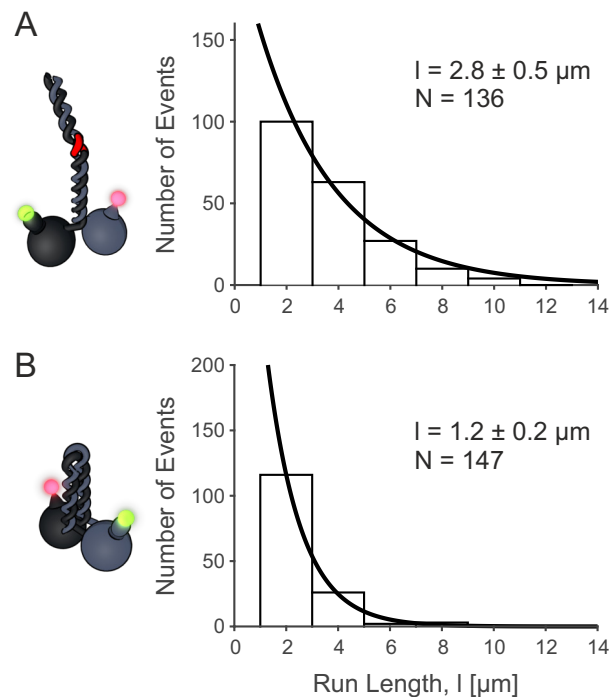
Appendix

Appendix I: Supplementary Figures

5.1 Run lengths of the used constructs at saturating ATP concentrations

Figure 5.1: SNAP- and Halo-tagged motors show typical run-lengths
Run length data for (**A**) eeKLP11^{Halo}/20^{SNAP} at 2.8 µm and (**B**) wtKLP11^{SNAP}/20^{Halo} at 1.2 µm. Exponential fit parameter ± 95 % confidence interval.

5.2 Dual color step sizes and stepping directions
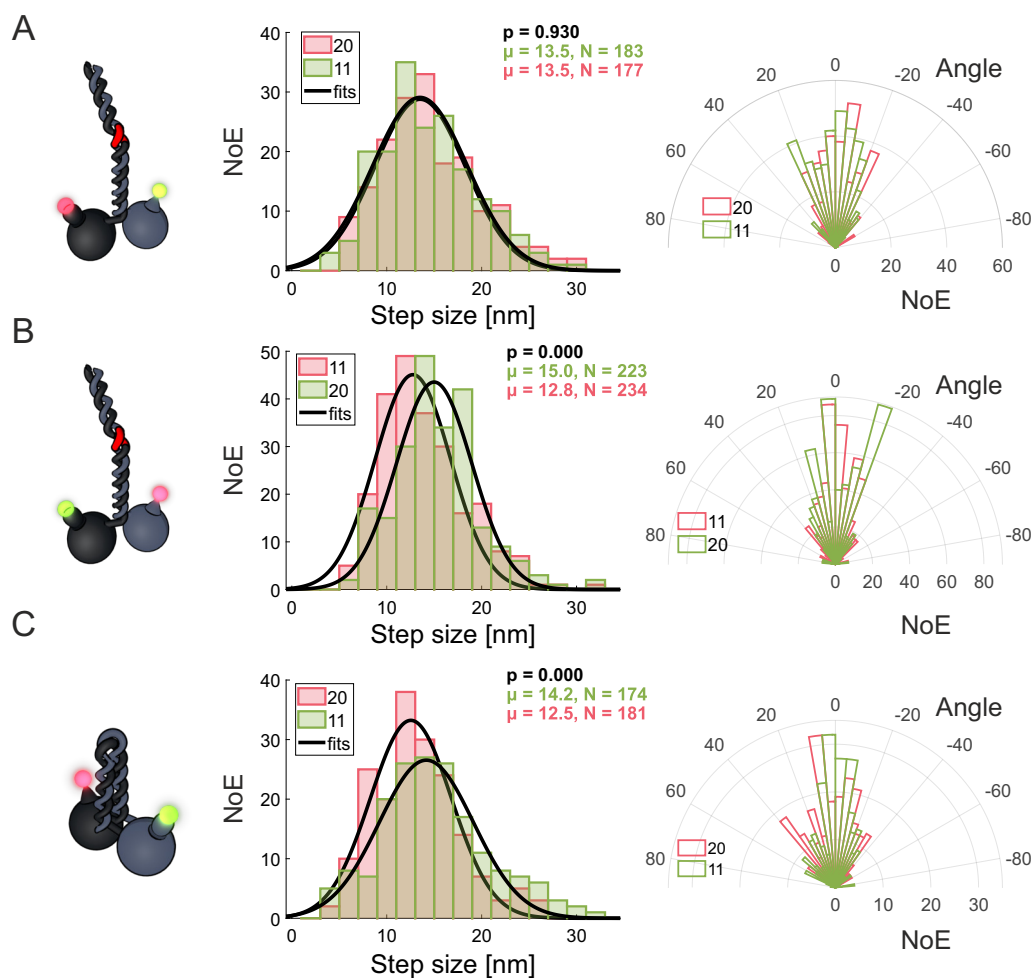
Figure 5.2: The individual step sizes and directions don't allow for any compelling conclusions.
(Middle) Step size distributions for each channel individually. Colored for the respective channel the stepping was measured in and fitted with gaussian profiles. The step size distributions show no consistent difference between the subunits. (Right) Step directions for each subunit individually. Again, there is no prominent difference in the data.
A eeKLP11$^{\text{Halo}}$/20$^{\text{SNAP}}$, **B** eeKLP11$^{\text{Halo}}$/20$^{\text{SNAP}}$, **C** wtKLP11$^{\text{SNAP}}$/20$^{\text{Halo}}$

5.3   Dual color step sizes by size of previous step
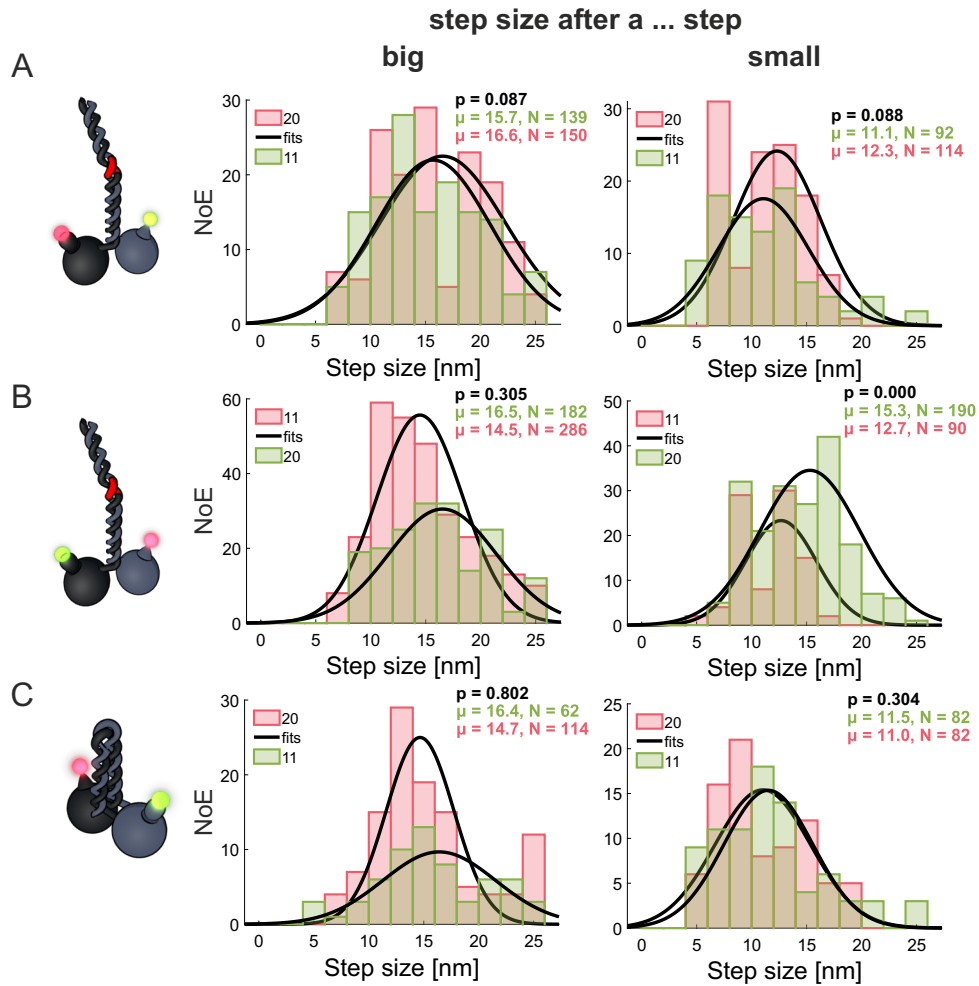
Figure 5.3: There is no apparent pattern in the step sizes sorted by previous step size.
(Middle) Step sizes that occurred after a big step (>15 nm). (Right) Step sizes that occurred after a small step (<11 nm). There is no apparent pattern in these distributions that would allow for a compelling conclusion.
A eeKLP11^Halo/20^SNAP, **B** eeKLP11^Halo/20^SNAP, **C** wtKLP11^SNAP/20^Halo

5.4 Labeling for single color FIONA experiments

Figure 5.4: Heterodimeric kinesin-2 motors were fluorescently labeled specifically.
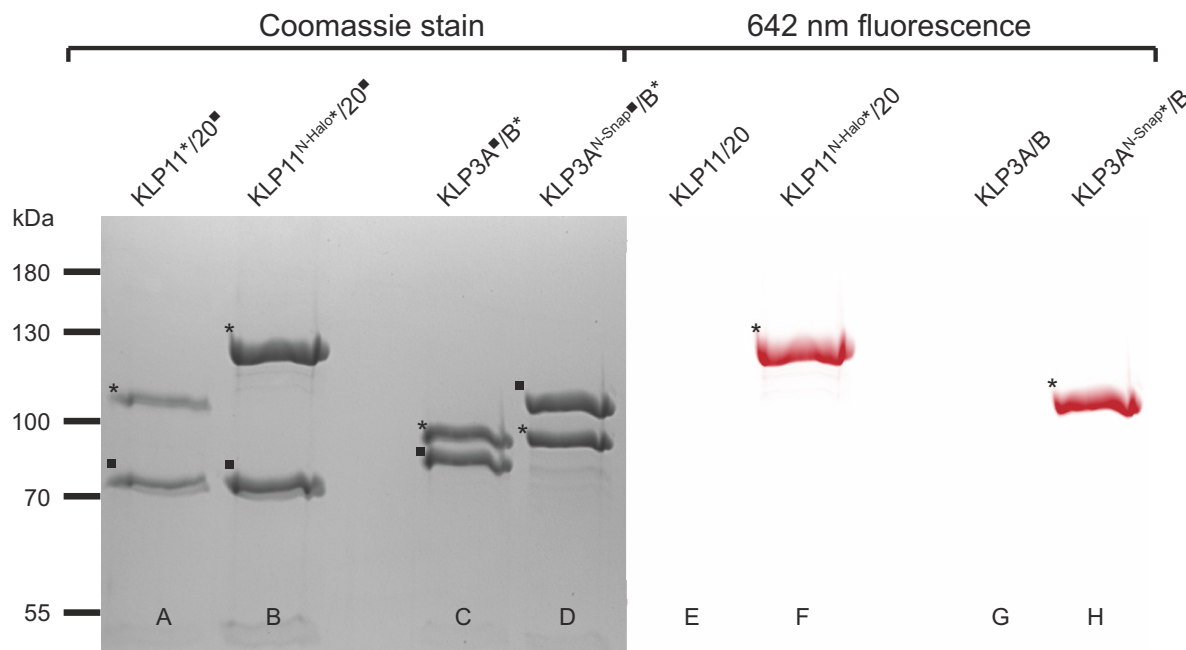**A & B** FLAGAffinity-Tag purification of the full length KLP11/20 heterodimer via the KLP20 subunit with (**B**) and without (**A**) the Halotag at the KLP11 subunit. Both proteins have been incubated with the fluorescently labeled peptide for labeling at the Halo-tag. Scanning of the SDS-PAGE at 642 nm showed that the only labeled protein band is the Halo-tagged KLP11 subunit (**E** vs. **F**).
C & D FLAG-Affinity-Tag purification of the full length KLP3A/B heterodimer via the KLP3A subunit with (**D**) and without (**C**) the SNAP-tag at the KLP3A subunit. Both proteins have been incubated with the fluorescently labeled peptide for labeling at the SNAP-tag. Scanning of the SDS-PAGE at 642 nm showed that the only labeled protein band is the SNAP-tagged KLP3A subunit (**G** vs. **H**). The figure was originally prepared by Georg Merck.

5.5 Example stepping traces of single color FIONA experiments
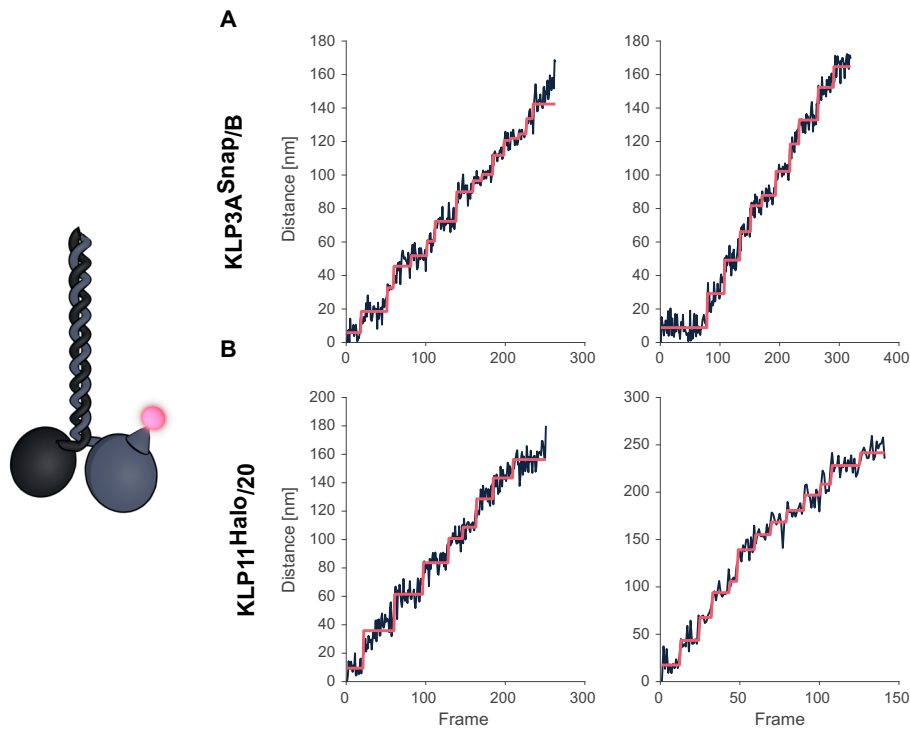
Figure 5.5: Single fluorophore tracking of KLP11/20 and KLP3A/B motors at limiting ATP concentrations.
Photons from a single fluorophore detected on the CCD are localized and tracked over time. Localization is achieved by fitting a two-dimensional Gaussian profile to the spot. The Euclidean distance of each location to the position in the first frame is calculated and plotted in blue. Steps in the data are detected by a gliding t-value algorithm and plotted in red. Frames have a cycle time of 505 ms.

5.6 Step sizes from dual color FIONA experiments
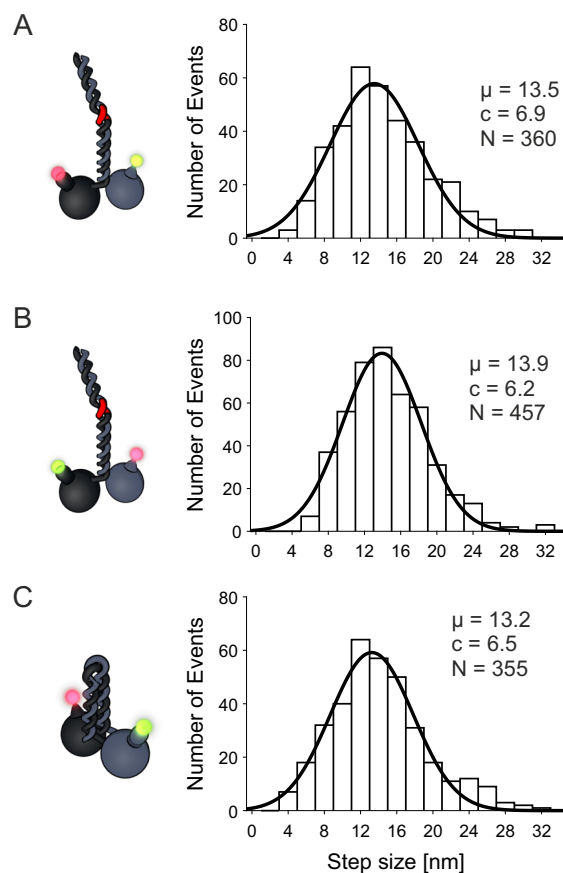
Figure 5.6: Step sizes of different KLP11/KLP20 constructs are close to what has been measured previously.
Step sizes of all runs were combined and pooled from both channels. Step size distributions for the single color experiments are confirmed on microtubules.
A eeKLP11[Halo]/20[SNAP]
B eeKLP11[Halo]/20[SNAP]
C wtKLP11[SNAP]/20[Halo]

5.7 Run-length exponential fits are not sensitive to truncation
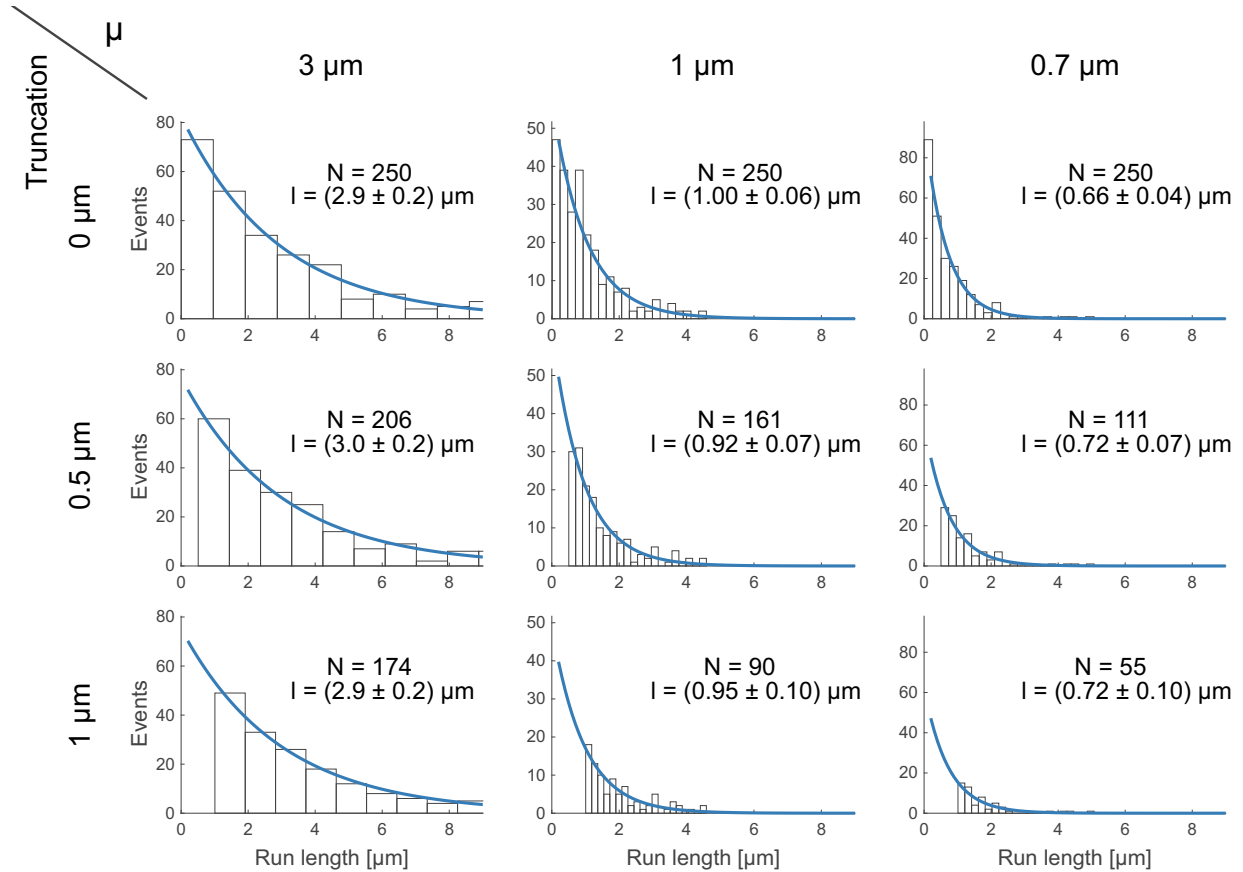
Figure 5.7: Truncation of the run length data does not influence the results of the exponential fits. The algorithm for exponential fits was tested for its performance on truncated data. Columns have the same parameter μfor the exponential distribution and rows have the same truncation parameter. For truncation, all values lower than the indicated threshold are disregarded. The algorithm was used to estimate the parameter μ of the distribution. The result is given ± the 95 % confidence intervals. N-numbers were chosen to be close to the lowest ones obtained for the motors described in the study. See also chapter 5.9

Appendix II

5.8 Dual exponential fit

In our first impression, the two dwell time distributions for KLP11 and KLP20 were distributed according to a double and single exponential model respectively. To support this assumption, we fitted both distributions with a double exponential model and show, that one of the parameters vanishes for the KLP20 dwell times. The model used was:

$$p = A(e^{-\lambda_1 x} - e^{-\lambda_2 x}) \tag{5.1}$$

We used the same settings and starting point for the fit:

$$A = 150; \lambda_1 = 0.3; \lambda_2 = 10; \tag{5.2}$$

In order to focus on the shorter dwell times, where the effect of the double exponential distribution can be seen best, we introduced a weight function:

$$1 - \frac{1}{1.2(1 + e^{-2x+5})} \tag{5.3}$$

5.9 Description of the main functions of the single molecule analysis software
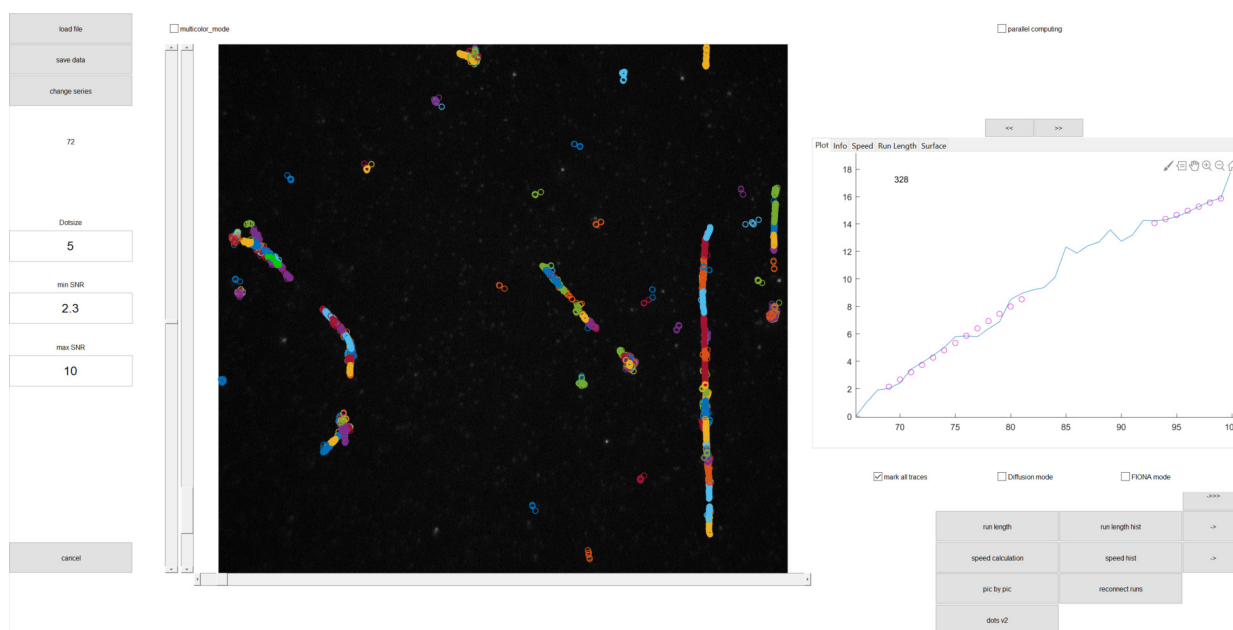
Figure 5.8: Overview of the user interface of the tracking algorithm.

This chapter will summarize the function of 2126 lines of code developed over a couple of years. A working version of this software and the respective files will be available at `github.com/wl-stepp/tracking_GUI`. This version was last tested under Matlab R2018b and used for [11, 28, 90, 106] and at least two more papers from our lab that are close to or already submitted by July 2019. As the algorithm we use is described only very briefly in the publications, I will describe the software and the interface in some more detail here.

The core of the program is meant for the analysis of single-molecule assays of molecular motors walking on surface attached filaments. The two main parameters that can be extracted are the speed and run-length of the motors. The detected runs however are also used for co-localization, step detection and diffusion analysis. It is optimized for minimum input of user-defined parameters aiming to reduce the experiment conductors bias into the data. Also, the shear amount of data analyzed in the last years in our lab would not have been possible by analyzing the data 'by hand'.

Basic capabilities and file compatibility

The software has been used in our lab for processive kinesin and myosin motors. The speed range it was tested in is ~$50\,\mathrm{nm\,s^{-1}}$ to ~$2\,\mathrm{\mu m\,s^{-1}}$. The fits for run-lengths are realized in a way, that allows the fitting below the cut-off at $1\,\mathrm{\mu m}$ (Supplementary Figure 5.7). Nevertheless, run-length that have been tested lie between $0.7\,\mathrm{\mu m}$ and $4\,\mathrm{\mu m}$. There is a main limitation to the minimum run-length being at least 5 frames of movement and thus depending on the speed of the motor due to the algorithm for speed calculation explained later. A lot of files could potentially be programmed for input, as the bio-formats package is used for this [107]. In the current state import is implemented for .sif (Andor), .lif (Leica) and .tif files. Meta data (cycle time and pixel to distance conversion) is imported from .sif and .lif files according to the respective companies guidelines. I also implemented a meta data environment for the tif files that is used by the FIONA-setup software described below. Specifics can be found in the get_meta_data.m file. Files should always be stacks of images. One out of multiple series inside one lif file can be chosen upon file choice. If multiple channels are present in a .lif file they can be separated using the multi_color mode.

Data import and user-set parameters

The data is imported into a Matlab 3D matrix and can be 'played' using the slider under the image (Figure 5.8 middle). A simple contrast algorithm based on percentage of brightest/darkest pixel sets the contrast and brightness of the image without user input. This allows a first unbiased assessment of the signal to noise ratio of the data. The first user input is then the 'dotsize', meaning the size of the square around a bright pixel that is used to interpret the motors position. This also has implications for the minimum distance between peaks, detailed later. The second user input is the signal-to-noise ratio of the peaks that should be evaluated. This can also be set by the vertical sliders. The simple 'as high as necessary, as low as possible' rule applies for the minimal signal-to-noise ratio setting. It should be high enough to not include any bright pixels in the noise but low enough to also accommodate fluctuations in the peak brightness from frame to frame. Overall, the better the signal-to-noise ratio in the data, the easier it is to find good settings for these parameters. If using a file without meta data, the pixel conversion (in $\mathrm{\mu m\,px^{-1}}$) and cycle time (in s) has to be set in the 'Info' tab on the right.

Detection of relevant peaks and sub-pixel position

The procedure for analysis is split into three stages, which allows assessment of intermediate results before further steps. The 'dots' button starts the search for relevant peaks in the field of view using the choose_noise_factor_tracking_v3.m function. A list of the pixels is ordered from the brightest pixel to the darkest. The noise level in the image is approximated by the mean intensity in the image. All peaks that have a higher ratio of brightest pixel over noise level than the set 'signal-to-noise ratio' (snr) are analyzed. A for loop starts at the brightest pixel and extracts a square the size of 'dotsize' from the frame. This prevents the repeated analysis of peaks that have many bright pixels. In this square, a test ensures, that the peak is still a bright spot in its immediate surrounding by comparing the mean brightness in the square with the mean brightness in a $2\,\mathrm{px}$ wide halo around the square. Next, the distances to the next already analyzed peak and the borders of the frame are measured. If these parameters fit a list of requirements (surrounding-factor $> 0.1 * (snr - 1) + 1$, next-peak distance $>$ dotsize, border distance $> 2\,\mathrm{px}$) a sub-pixel accuracy position of the peak is determined. In the normal mode, a radial center approach is used to do this due to its superior calculation time [105]. If the 'FIONA mode' is activated, this step is done by fitting a 2D gaussian profile to the data in the specified square. This yields the more accurate data for stepping analysis but is very time consuming and not necessary for speed and run-length analysis. If the sub-pixel position of the motor is determined successfully, the acquired data is written into the peakvalues cell type variable:

peakvalues{frame}(i,peak_number)

i:

1 signal-to-noise ratio

2 sub-pixel x position

3 sub-pixel y position

4 peak_ID used for later sorting

5 used for later proximity data

6 later for distance to first peak in run

7 frame

8 total brightness

This leads to a list of all relevant peaks and their properties for each frame of the stack. These are indicated by open circles in the user interface. The user should now assess the result by checking if the desired peaks are actually tracked and adjust the input parame-

ters if necessary.

This procedure is run for each frame independently and can therefore be parallelized. Even though Matlab is good at allocating CPU threads, even better performance was observed when using a parfor loop. A performance increase of ~0.7 times the number of cores is typically observed. The parfor integration also allows running the code on a external cluster, a function not tested thoroughly so far.

Construction of runs by frame-to-frame analysis

Peaks have to be followed now from frame to frame (pic_by_pic button and pic_by_pic.m function). This procedure is actually vectorized in the code in order to enhance the performance, but I will describe the classic approach here, as vectorized code is very non-intuitive (see `www.mathworks.com/help/matlab/matlab_prog/vectorization.html` for more details). The pairwise distance of peaks is calculated frame-to-frame. A cycle through all the peaks detects the closest peak in the next frame to the reference peak. It is also checked, that this peak is not closer to any other peak in the current frame by first calculating all the distances. If this peak is closer than the dotsize, it is appended to the current run and excluded from further analysis. If a peak is not close enough to any peak in the previous frame, it gets a new run ID and can initiate a new run. This leads to a cell structure of runs, with each run being a list of data from the peakvalues cell with the data specified above. With the 'mark all traces' option selected the user can now assess if all desired runs are detected. If runs are interrupted, the snr can be lowered and the data should be checked for blinking of the fluorophores.

As each instance of the for loop needs the data from two frames, the performance benefit of parallelization depends on the capability of the system to handle overhead in the memory.

Calculation of speeds and run-lengths

For speed calculation, the distance of all peaks in a run to the initial position are calculated. The run-length of the run is the maximal distance to the start position in this data. Speed calculation is performed on the distance-time data by fitting lines to parts of the data as follows. Starting from the first 6 data points, a linear regression is performed. Additional data points are added to the fit as long as the fit achieves the minimum r-squared value of 95 %. If this criterion is not met, the current speed measurement

is terminated and the last good fit parameters are saved. The next speed measurement is initiated as before from the next point after the previous measurement. If a speed was calculated for more than one part of the run, the overall speed is calculated as the mean of all fits. The obtained data can be plotted from the software directly into histograms or exported into a comma-separated values format and .mat files. This procedure runs independently for each run and could therefore be parallelized with high efficiency.

Further analysis of the runs

The runs obtained from tracking can also be used for further analysis. At limiting ATP-concentrations and using the 'FIONA mode', the function kinesin_step_detection_v2 pulls the data from a current run in the tracking software directly and performs step detection and analysis. The functions colocalize_runs_vX work on exported .mat files that contain all runs in two channels. The algorithm detects runs that are very close in the space and time domain and allows to estimate the percentage of runs that are observed in both channels. If the motors show diffusive behavior and the 'Diffusion mode' is used, the function batch_msd_from_traces calculates the mean square displacement of the diffusion behavior and additional parameters.

5.10 Description of the user interface of the microscope software
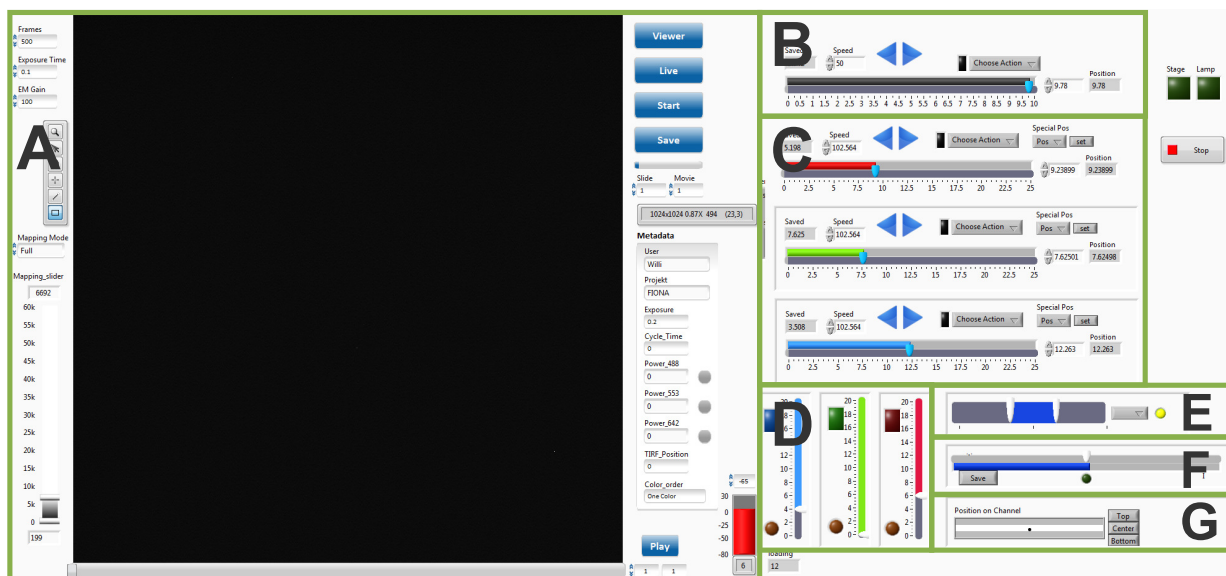
Figure 5.9: Overview of the general user interface of the microscope.

Main design

The software is implemented in LabView with some calls to Matlab functions. LabView has the main advantage of being inherently multi-threaded, making it optimal for applications where many in- and outputs have to be handled simultaneously at any moment. With very few exceptions, there is some kind of implementation for LabView programming for scientific devices and equipment. Many companies supply function .VIs that relay commands to the device in a very convenient way. For others, serial commands can be sent using the RS-232 protocol. Finally any device with a USB driver can be controlled or read out using a VISA interface.

The implementation for some of the VIs is rather intricate, especially the camera module and the readout of the the 3D mouse for the stage control. I will therefore explain only the user interface of each module here. The code is commented on the first subVI level in a manner, that should allow a LabView experienced programmer a basic understanding of the implemented functions. There is an introduction to the API (application programming interface) for most of the devices in the setup that is a good start to understand the

VIs. Many times I used the example VIs of the suppliers as inspiration for the implementation of the modules.

The main user interface is comprised of several so-called subpanels (LabView information). These allow to display the front panel of a subVI in the main VI window. The advantage of this approach is the modular nature. That means each subVI starts in a separate thread and can be disabled if maintenance is necessary. Also the individual subVIs work independently, can be tested individually and could be used in other applications. The disadvantage is, that communication between the VIs is somewhat complicated. This communication is realized mostly by 'flow field variables' that can store and output data dynamically (more Info).

The design of the GUI is inspired by both the Leica LAS X software (Leica link) that runs on our other TIRF systems and the Andor Solis software (Andor link) that I used previously on this setup. It is also optimized for the wide screen used on the setup, so more information and controls can be on-screen at the same time.

A: Camera module

All important functions of the camera can be controlled in this part of the GUI. The main parameters like number of frames for the recording of a series and the exposure time are set on the left. The main window either shows the live image of the camera or the last recorded series. The range and brightness of the LUT can be set using a dual slider on the lower left, or it is set to one of the automatic modes in the 'mapping mode' box. For an integrated way to show recorded series, a 'viewer' also based on a LabView VI is included with the software. It also outputs the metadata that is saved together with recorded series automatically. This includes values from the camera itself (cycle time and exposure), user set variables (user and project name), TIRF parameters and laser settings (power and on/off). The data is saved into the description of the tif file in the standard json format used for extended meta data. If a recorded file is saved, the information is used to automatically organize the files to SSD/User/reversedate_project/reversedate _slide_movie.tif. The movie counter is automatically incremented after each save which allows for a very efficient work flow of data collection. The temperature of the chip cooler is controlled on the lower right. The integration of the camera controls into the software also allows to control the lasers depending on the state of the camera. This reduces exposure of the sample to laser light during phases where the shutter of the camera is closed anyways.

B: TIRF angle adjustment

The TIRF angle is adjusted by positioning the beam of the lasers at different offsets from the center of the objective. This is achieved by a motor-controlled stage that can be controlled in this section. A position can be saved and restored later for repeatable experiments.

C: Channel positioning

The positions of the channels are controlled in a similar way as the TIRF angle. In order to make a switch between single- and multi-color mode of the microscope easy, each color has different saved positions. A center position for imaging in only that channel, a half position (left and right for the green channel) and a one third position. For adjusting these positions, they can be selected, then fine-tuned and the new position can be saved using the 'set' button. Parameters like these are saved in a text file, for easy access and reliability.

D: Laser controls

All three lasers are controlled in this section. The squared LEDs are both power switches and indicators for the lasers. For blue and red, the lasers are controlled directly and the power output is regulated by the laser unit itself. As the green laser is a diode pumped solid state laser, a direct modulation of the output power is not possible and it requires a startup sequence. For this, an additional pair of polarizers is installed here. The power slider controls the angle of the second polarizer to adjust the power output reaching the objective.

E: Cropping slit

In order to position the channels next to each other on the camera chip, the individual images are cropped to different widths. An optical slit that is driven by a linear motor is used for this. The control allows a manual input or preset positions for full/half/third frame positions. For adjustment of one of the presets, the preset is chosen, then adjusted and the new position is saved using the 'set' option in the drop-down menu. The closed positions is used to calculate the second slider that is just a visual aid to estimate the momentary aperture of the slit.

F: Focus position

This part of the interface shows the position of the focus axis of the piezo-stepper stage of the sample stage. If the cover-slip surface is found, that position can be saved and is set to the middle of the scale. This allows for a rough estimation of the focus position for the next slide. An LED indicates the fast/slow status of the stage control by the controller.

G: Flow chamber position

An estimation of the position of the objective on the flow chamber is displayed here. The typical channel size is shown in the white bar. If the stage is moved in x/y, the dot moves the respective distance and shows the approximate position of the field of view on the channel. This can be used to avoid the edges of the channel and to see possible differences in the beginning/end of the channel. Adjustments can be realized if the top/bottom edges of the channel is encountered. The display will then readjust the y-position to reflect the real position better.

Bibliography

[1] Edward Humes. *Door to Door: The Magnificent, Maddening, Mysterious World of Transportation*. HarperCollins, 2016. ISBN: 0062372092.

[2] Toshihide Nariko Yuko Kimura Arimura Fukata et al. "Tubulin and CRMP-2 complex is transported via Kinesin-1". In: *Journal of Neurochemistry* 93.6 (May 2005), pp. 1371–1382. ISSN: 00223042. DOI: 10.1111/j.1471-4159.2005.03063.x.

[3] Ronald D Vale. "The molecular motor toolbox for intracellular transport". In: *Cell* 112.4 (Feb. 2003), pp. 467–480. ISSN: 0092-8674 (Print) 0092-8674 (Linking). DOI: 10.1016/S0092-8674(03)00111-9.

[4] Jonathan M Scholey. "Intraflagellar transport". In: *Annu. Rev. Cell Dev. Biol* 19 (2003), pp. 423–466. DOI: 10.1146/annurev.cellbio.19.111401.091318.

[5] F Lin et al. "Kidney-specific inactivation of the KIF3A subunit of kinesin-II inhibits renal ciliogenesis and produces polycystic kidney disease". In: *Proc Natl Acad Sci U S A* 100.9 (2003), pp. 5286–5291. ISSN: 0027-8424 (Print) 0027-8424 (Linking). DOI: 10.1073/pnas.0836980100.

[6] Ahmet Yildiz et al. "Myosin V walks hand-over-hand: single fluorophore imaging with 1.5-nm localization". In: *Science* 300.5628 (June 2003), pp. 2061–2065. ISSN: 1095-9203 (Electronic) 0036-8075 (Linking). DOI: 10.1126/science.1084398.

[7] A Yildiz et al. "Kinesin walks hand-over-hand". In: *Science* 303.5658 (2004), pp. 676–678. ISSN: 1095-9203 (Electronic) 0036-8075 (Linking). DOI: 10.1126/science.1093753.

[8] S P Gilbert et al. "Pathway of processive ATP hydrolysis by kinesin." In: *Nature* 373.6516 (Feb. 1995), pp. 671–6. ISSN: 0028-0836. DOI: 10.1038/373671a0.

[9]   Keith J. Mickolajczyk and William O. Hancock. "Kinesin Processivity Is Determined by a Kinetic Race from a Vulnerable One-Head-Bound State". In: *Biophysical Journal* 112.12 (June 2017), pp. 2615–2623. ISSN: 0006-3495. DOI: `10.1016/J.BPJ.2017.05.007`.

[10]   Sander Verbrugge, Siet M.J.L. van den Wildenberg, and Erwin J.G. Peterman. "Novel Ways to Determine Kinesin-1's Run Length and Randomness Using Fluorescence Microscopy". In: *Biophysical Journal* 97.8 (2009), p. 2287. DOI: `10.1016/J.BPJ.2009.08.001`.

[11]   Mohamed A.A. A. Mohamed, Willi L. Stepp, and Zeynep Ökten. "Reconstitution reveals motor activation for intraflagellar transport". In: *Nature* 557.7705 (May 2018), pp. 387–391. ISSN: 14764687. DOI: `10.1038/s41586-018-0105-3`.

[12]   Dawen Cai et al. "Kinesin-1 structural organization and conformational changes revealed by FRET stoichiometry in live cells". In: *The Journal of Cell Biology* 176.1 (Jan. 2007), pp. 51–63. ISSN: 0021-9525. DOI: `10.1083/JCB.200605097`.

[13]   Dara S. Friedman and Ronald D. Vale. "Single-molecule analysis of kinesin motility reveals regulation by the cargo-binding tail domain". In: *Nature Cell Biology* 1.5 (Sept. 1999), pp. 293–297. ISSN: 1465-7392. DOI: `10.1038/13008`.

[14]   David L. Coy et al. "Kinesin's tail domain is an inhibitory regulator of the motor domain". In: *Nature Cell Biology* 1.5 (Sept. 1999), pp. 288–292. ISSN: 1465-7392. DOI: `10.1038/13001`.

[15]   David D. Hackney, Nahyeon Baek, and Avin C. Snyder. "Half-site inhibition of dimeric kinesin head domains by monomeric tail domains". In: *Biochemistry* 48.15 (Apr. 2009), pp. 3448–3456. ISSN: 00062960. DOI: `10.1021/bi8022575`.

[16]   Hung Yi Kristal Kaan, David D Hackney, and Frank Kozielski. "The structure of the kinesin-1 motor-tail complex reveals the mechanism of autoinhibition." In: *Science (New York, N.Y.)* 333.6044 (Aug. 2011), pp. 883–5. ISSN: 1095-9203. DOI: `10.1126/science.1204824`.

[17]   Julien Espeut et al. "Phosphorylation Relieves Autoinhibition of the Kinetochore Motor Cenp-E". In: *Molecular Cell* 29.5 (Mar. 2008), pp. 637–643. ISSN: 1097-2765. DOI: `10.1016/J.MOLCEL.2008.01.004`.

[18]   Kunning Chen et al. "Phosphorylation regulates auto-inhibition of kinesin KIF3A". In: *bioRxiv* (Dec. 2018), p. 503680. DOI: `10.1101/503680`.

[19] Toni McHugh et al. "Kif15 functions as an active mechanical ratchet". In: *Molecular Biology of the Cell* 29.13 (July 2018). Ed. by Thomas D. Pollard, pp. 1743–1752. ISSN: 1059-1524. DOI: `10.1091/mbc.E18-03-0151`.

[20] D. D. Hackney and M. F. Stock. "Kinesin's IAK tail domain inhibits initial microtubule-stimulated ADP release". In: *Nature Cell Biology* 2.5 (May 2000), pp. 257–260. ISSN: 1465-7392. DOI: `10.1038/35010525`.

[21] David D. Hackney and Maryanne F. Stock. "Kinesin Tail Domains and Mg 2+ Directly Inhibit Release of ADP from Head Domains in the Absence of Microtubules †". In: *Biochemistry* 47.29 (July 2008), p. 33. ISSN: 0006-2960. DOI: `10.1021/bi8006687`.

[22] Kristen A. Dietrich et al. "The kinesin-1 motor protein is regulated by a direct interaction of its head and tail". In: *Proc Natl Acad Sci U S A* 105.26 (July 2008), p. 8938. ISSN: 0027-8424. DOI: `10.1073/PNAS.0803575105`.

[23] Yao Liang Wong et al. "The Kinesin-1 Tail Conformationally Restricts the Nucleotide Pocket". In: *Biophysical Journal* 96.7 (Apr. 2009), p. 2799. ISSN: 1542-0086. DOI: `10.1016/J.BPJ.2008.11.069`.

[24] D. G. Cole et al. "Novel heterotrimeric kinesin-related protein purified from sea urchin eggs". In: *Nature* 366.6452 (Nov. 1993), pp. 268–270. ISSN: 0028-0836. DOI: `10.1038/366268a0`.

[25] Xiaoyu Pan et al. "Mechanism of transport of IFT particles in C. elegans cilia by the concerted action of kinesin-II and OSM-3 motors". In: *Journal of Cell Biology* 174.7 (Sept. 2006), pp. 1035–1045. ISSN: 00219525. DOI: `10.1083/jcb.200606003`.

[26] Melanie Brunnbauer et al. "Regulation of a heterodimeric kinesin-2 through an unprocessive motor domain that is turned processive by its partner". In: *Proceedings of the National Academy of Sciences* 107.23 (June 2010), pp. 10460–10465. ISSN: 0027-8424. DOI: `10.1073/pnas.1005177107`.

[27] Gayatri Muthukrishnan et al. "The processivity of kinesin-2 motors suggests diminished front-head gating". In: *Curr Biol* 19.5 (2009), pp. 442–447. ISSN: 1879-0445 (Electronic) 0960-9822 (Linking). DOI: `10.1016/j.cub.2009.01.058`.

[28] Willi L Stepp et al. "Kinesin-2 motors adapt their stepping behavior for processive transport on axonemes and microtubules". In: *EMBO Rep* 18.11 (Nov. 2017), pp. 1947–1956. ISSN: 1469-3178 (Electronic) 1469-221X (Linking). DOI: `10.15252/embr.201744097`.

[29] Stephanie Guzik-Lendrum et al. "Kinesin-2 KIF3AC and KIF3AB Can Drive Long-Range Transport along Microtubules". In: *Biophys J* 109.7 (Oct. 2015), pp. 1472–1482. ISSN: 1542-0086 (Electronic) 0006-3495 (Linking). DOI: `10.1016/j.bpj.2015.08.004`.

[30] Jonathan M. Scholey. "Kinesin-2: A Family of Heterotrimeric and Homodimeric Motors with Diverse Intracellular Transport Functions". In: *Annual Review of Cell and Developmental Biology* 29.1 (Oct. 2013), pp. 443–469. ISSN: 1081-0706. DOI: `10.1146/annurev-cellbio-101512-122335`.

[31] Willi L Stepp. "The Kinesin-2 Walking Mechanism". Master Thesis. Technical University Munich, 2016, p. 44.

[32] Richard A. Walker, Edward D. Salmon, and Sharyn A. Endow. "The Drosophila claret segregation protein is a minus-end directed motor molecule". In: *Nature* 347.6295 (Oct. 1990), pp. 780–782. ISSN: 0028-0836. DOI: `10.1038/347780a0`.

[33] Melanie Brunnbauer et al. "Torque Generation of Kinesin Motors Is Governed by the Stability of the Neck Domain". In: *Molecular Cell* 46.2 (2012), pp. 147–158. ISSN: 10972765. DOI: `10.1016/j.molcel.2012.04.005`.

[34] Sinan Can, Mark A Dewitt, and Ahmet Yildiz. "Bidirectional helical motility of cytoplasmic dynein around microtubules". In: *Elife* 3 (2014), p. 3205. DOI: `10.7554/eLife.03205`.

[35] Gregory J. Hoeprich et al. "The axonal transport motor kinesin-2 navigates microtubule obstacles via protofilament switching". In: *Traffic* 18.5 (May 2017), pp. 304–314. ISSN: 13989219. DOI: `10.1111/tra.12478`.

[36] René Schneider et al. "Kinesin-1 Motors Can Circumvent Permanent Roadblocks by Side-Shifting to Neighboring Protofilaments". In: *Biophysical Journal* 108.9 (May 2015), pp. 2249–2257. ISSN: 0006-3495. DOI: `10.1016/J.BPJ.2015.03.048`.

[37] Jinqi Ren et al. "Coiled-coil 1-mediated fastening of the neck and motor domains for kinesin-3 autoinhibition." In: *Proceedings of the National Academy of Sciences of the United States of America* 115.51 (Dec. 2018), E11933–E11942. ISSN: 1091-6490. DOI: 10.1073/pnas.1811209115.

[38] Yunxin Zhang and Michael E Fisher. "Measuring the Limping of Processive Motor Proteins". In: *J Stat Phys* 142 (2011), pp. 1218–1251. DOI: 10.1007/s10955-011-0118-x.

[39] Sean M Quinn et al. "Kinesin-2 heterodimerization alters entry into a processive run along the microtubule but not stepping within the run." In: *The Journal of biological chemistry* 293.35 (July 2018), jbc.RA118.002767. ISSN: 1083-351X. DOI: 10.1074/jbc.RA118.002767.

[40] Kuniyoshi Kaseda, Hideo Higuchi, and Keiko Hirose. "Alternate fast and slow stepping of a heterodimeric kinesin molecule". In: *Nat Cell Biol* 5.12 (Dec. 2003), pp. 1079–1082. ISSN: 1465-7392 (Print) 1465-7392 (Linking). DOI: 10.1038/ncb1067.

[41] Hideo Higuchi et al. "Rapid double 8-nm steps by a kinesin mutant". In: *The EMBO Journal* 23.15 (Aug. 2004), pp. 2993–2999. ISSN: 0261-4189. DOI: 10.1038/sj.emboj.7600306.

[42] Pengwei Zhang, Ivan Rayment, and Susan P Gilbert. "Fast or Slow, Either Head Can Start the Processive Run of Kinesin-2 KIF3AC." In: *The Journal of biological chemistry* 291.9 (Feb. 2016), pp. 4407–16. ISSN: 1083-351X. DOI: 10.1074/jbc.M115.705970.

[43] Todd Thoresen and Jeff Gelles. "Processive Movement by a Kinesin Heterodimer with an Inactivating Mutation in One Head †". In: *Biochemistry* 47.36 (Sept. 2008), pp. 9514–9521. ISSN: 0006-2960. DOI: 10.1021/bi800747e.

[44] Charles L. Asbury, Adrian N. Fehr, and Steven M. Block. "Kinesin moves by an asymmetric hand-over-hand mechanism". In: *Science* 302.5653 (Dec. 2003), pp. 2130–2134. ISSN: 1095-9203 (Electronic) 0036-8075 (Linking). DOI: 10.1126/science.1092985.

[45] Fabian Sievers et al. "Fast, scalable generation of high-quality protein multiple sequence alignments using Clustal Omega". In: *Molecular Systems Biology* 7 (2011). ISSN: 17444292. DOI: 10.1038/msb.2011.75.

[46] "UniProt: a worldwide hub of protein knowledge". In: *Nucleic Acids Research* 47.D1 (Jan. 2019), pp. D506–D515. ISSN: 0305-1048. DOI: 10.1093/nar/gky1049.

[47] Miki Imanishi et al. "Autoinhibition regulates the motility of the C. elegans intraflagellar transport motor OSM-3". In: *Journal of Cell Biology* 174.7 (Sept. 2006), pp. 931–937. ISSN: 00219525. DOI: 10.1083/jcb.200605179.

[48] Joshua J. Snow et al. "Two anterograde intraflagellar transport motors cooperate to build sensory cilia on C. elegans neurons". In: *Nature Cell Biology* 6.11 (Nov. 2004), pp. 1109–1113. ISSN: 14657392. DOI: 10.1038/ncb1186.

[49] Süleyman Kösem. "Kinetic properties of heteromeric kinesin-2 from Caenorhabditis elegans". PhD thesis. 2014, p. 101.

[50] Chengtian Zhao et al. "Kinesin-2 family in vertebrate ciliogenesis." In: *Proceedings of the National Academy of Sciences of the United States of America* 109.7 (Feb. 2012), pp. 2388–93. ISSN: 1091-6490. DOI: 10.1073/pnas.1116035109.

[51] Lotte B. Pedersen and Joel L. Rosenbaum. "Chapter Two Intraflagellar Transport (IFT): Role in Ciliary Assembly, Resorption and Signalling". In: *Current Topics in Developmental Biology* 85 (Jan. 2008), pp. 23–61. ISSN: 0070-2153. DOI: 10.1016/S0070-2153(08)00802-8.

[52] Jonathan M Scholey. "Intraflagellar transport motors in cilia: moving along the cell's antenna." In: *The Journal of cell biology* 180.1 (Jan. 2008), pp. 23–9. ISSN: 1540-8140. DOI: 10.1083/jcb.200709133.

[53] Regina Faubel et al. "Cilia-based flow network in the brain ventricles." In: *Science (New York, N.Y.)* 353.6295 (July 2016), pp. 176–8. ISSN: 1095-9203. DOI: 10.1126/science.aae0450.

[54] James R. Davenport and Bradley K. Yoder. "An incredible decade for the primary cilium: a look at a once-forgotten organelle". In: *American Journal of Physiology-Renal Physiology* 289.6 (Dec. 2005), F1159–F1169. ISSN: 1931-857X. DOI: 10.1152/ajprenal.00118.2005.

[55] Helen May-Simera, Kerstin Nagel-Wolfrum, and Uwe Wolfrum. "Cilia - The sensory antennae in the eye". In: *Progress in Retinal and Eye Research* 60 (Sept. 2017), pp. 144–180. ISSN: 1350-9462. DOI: 10.1016/J.PRETEYERES.2017.05.001.

[56] Friedhelm Hildebrandt, Thomas Benzing, and Nicholas Katsanis. "Ciliopathies".
In: *New England Journal of Medicine* 364.16 (Apr. 2011). Ed. by Robert S. Schwartz,
pp. 1533–1543. ISSN: 0028-4793. DOI: `10.1056/NEJMra1010172`.

[57] Sandra Habbig and Max Christoph Liebau. "Ciliopathies - from rare inherited cys-
tic kidney diseases to basic cellular function." In: *Molecular and cellular pediatrics*
2.1 (Dec. 2015), p. 8. ISSN: 2194-7791. DOI: `10.1186/s40348-015-0019-1`.

[58] Michael Taschner, Sagar Bhogaraju, and Esben Lorentzen. "Architecture and
function of IFT complex proteins in ciliogenesis". In: *Differentiation* 83.2 (Feb.
2012), S12–S22. ISSN: 0301-4681. DOI: `10.1016/J.DIFF.2011.11.001`.

[59] Bojan Milic et al. "Intraflagellar transport velocity is governed by the number of
active KIF17 and KIF3AB motors and their motility properties under load". In:
Proceedings of the National Academy of Sciences 114.33 (2017), E6830–E6838.
ISSN: 0027-8424. DOI: `10.1073/pnas.1708157114`.

[60] B H Gibbons et al. "Phylogeny and expression of axonemal and cytoplasmic dynein
genes in sea urchins." In: *Molecular Biology of the Cell* 5.1 (Jan. 1994), pp. 57–70.
ISSN: 1059-1524. DOI: `10.1091/mbc.5.1.57`.

[61] Y Tanaka, Z Zhang, and N Hirokawa. "Identification and molecular evolution of
new dynein-like protein sequences in rat brain". In: *Journal of Cell Science* 108.5
(May 1995), 1883 LP –1893.

[62] Z.F. Altun et al. *wormatlas.org*. 2019.

[63] Guangshuo Ou et al. "Functional coordination of intraflagellar transport motors".
In: *Nature* 436.7050 (July 2005), pp. 583–587. ISSN: 00280836. DOI: `10.1038/nature03818`.

[64] Saikat Mukhopadhyay et al. "Distinct IFT mechanisms contribute to the gener-
ation of ciliary structural diversity in C. elegans". In: *The EMBO Journal* 26.12
(June 2007), pp. 2966–2980. ISSN: 0261-4189. DOI: `10.1038/sj.emboj.7601717`.

[65] Guangshuo Ou et al. "Sensory ciliogenesis in Caenorhabditis elegans: Assignment
of IFT components into distinct modules based on transport and phenotypic pro-
files". In: *Molecular Biology of the Cell* 18.5 (May 2007), pp. 1554–1569. ISSN:
10591524. DOI: `10.1091/mbc.E06-09-0805`.

Bibliography

[66]   Michael A. Silverman and Michel R. Leroux. *Intraflagellar transport and the gen-eration of dynamic, structurally and functionally diverse cilia*. July 2009. DOI: `10.1016/j.tcb.2009.04.002`.

[67]   D Chretien and R H Wade. "New data on the microtubule surface lattice". In: *Biol Cell* 71.1-2 (1991), pp. 161–174. ISSN: 0248-4900 (Print) 0248-4900 (Linking).

[68]   Y H Song and E Mandelkow. "The anatomy of flagellar microtubules: polarity, seam, junctions, and lattice". In: *J Cell Biol* 128.1-2 (Jan. 1995), pp. 81–94. ISSN: 0021-9525 (Print) 0021-9525 (Linking). DOI: `10.1083/jcb.128.1.81`.

[69]   Pablo Sartori et al. "Dynamic curvature regulation accounts for the symmetric and asymmetric beats of Chlamydomonas flagella". In: *eLife* 5 (May 2016). ISSN: 2050-084X. DOI: `10.7554/eLife.13258`.

[70]   Daniela Nicastro et al. "The molecular architecture of axonemes revealed by cryo-electron tomography." In: *Science (New York, N.Y.)* 313.5789 (Aug. 2006), pp. 944–8. ISSN: 1095-9203. DOI: `10.1126/science.1128618`.

[71]   Haixin Sui and Kenneth H. Downing. "Molecular architecture of axonemal micro-tubule doublets revealed by cryo-electron tomography". In: *Nature* 442.7101 (July 2006), pp. 475–478. ISSN: 0028-0836. DOI: `10.1038/nature04816`.

[72]   Takashi Ishikawa. "Cryo-electron tomography of motile cilia and flagella". In: *Cilia* 4.1 (Dec. 2015), p. 3. ISSN: 2046-2530. DOI: `10.1186/s13630-014-0012-7`.

[73]   Ludek Stepanek et al. "Microtubule doublets are double-track railways for in-traflagellar transport trains". In: *Science* 352.6286 (May 2016), pp. 721–724. ISSN: 1095-9203 (Electronic) 0036-8075 (Linking). DOI: `10.1126/science.aaf4594`.

[74]   Bruce J. Schnapp et al. "Single microtubules from squid axoplasm support bidi-rectional movement of organelles". In: *Cell* 40.2 (Feb. 1985), pp. 455–462. ISSN: 00928674. DOI: `10.1016/0092-8674(85)90160-6`.

[75]   Ronald D. Vale, Thomas S. Reese, and Michael P. Sheetz. "Identification of a novel force-generating protein, kinesin, involved in microtubule-based motility". In: *Cell* 42.1 (Aug. 1985), pp. 39–50. ISSN: 00928674. DOI: `10.1016/S0092-8674(85)80099-4`.

[76]   Takashi Funatsu et al. "Imaging of single fluorescent molecules and individual ATP turnovers by single myosin molecules in aqueous solution". In: *Nature* 374.6522 (Apr. 1995), pp. 555–559. ISSN: 00280836. DOI: `10.1038/374555a0`.

[77] Ronald D. Vale et al. "Direct observation of single kinesin molecules moving along microtubules". In: *Nature* 380.6573 (Apr. 1996), pp. 451–453. ISSN: 00280836. DOI: `10.1038/380451a0`.

[78] D Axelrod, N L Thompson, and T P Burghardt. "Total internal inflection fluorescent microscopy". In: *J Microsc* 129.Pt 1 (1983), pp. 19–28. ISSN: 0022-2720 (Print) 0022-2720 (Linking).

[79] Zeynep Ökten et al. "Myosin VI walks hand-over-hand along actin". In: *Nat Struct Mol Biol* 11.9 (2004), pp. 884–887. ISSN: 1545-9993 (Print) 1545-9985 (Linking). DOI: `10.1038/nsmb815`.

[80] Samara L. Reck-Peterson et al. "Single-Molecule Analysis of Dynein Processivity and Stepping Behavior". In: *Cell* 126.2 (July 2006), pp. 335–348. ISSN: 00928674. DOI: `10.1016/j.cell.2006.05.046`.

[81] David M. Warshaw et al. "Differential labeling of myosin V heads with quantum dots allows direct visualization of hand-over-hand processivity". In: *Biophysical Journal* 88.5 (May 2005), pp. L30–L32. ISSN: 00063495. DOI: `10.1529/biophysj.105.061903`.

[82] Joanna Andrecka et al. "Structural dynamics of myosin 5 during processive motion revealed by interferometric scattering microscopy". In: *eLife* 2015.4 (Mar. 2015). ISSN: 2050084X. DOI: `10.7554/eLife.05413`.

[83] Keith J. Mickolajczyk et al. "Kinetics of nucleotide-dependent structural transitions in the kinesin-1 hydrolysis cycle". In: *Proceedings of the National Academy of Sciences* 112.52 (2015), E7186–E7193. ISSN: 0027-8424. DOI: `10.1073/pnas.1517638112`.

[84] Francisco Balzarotti et al. "Nanometer resolution imaging and tracking of fluorescent molecules with minimal photon fluxes". In: *Science* 355.6325 (Feb. 2017), pp. 606–612. ISSN: 10959203. DOI: `10.1126/science.aak9913`.

[85] Russell E. Thompson, Daniel R. Larson, and Watt W. Webb. "Precise nanometer localization analysis for individual fluorescent probes". In: *Biophysical Journal* 82.5 (2002), pp. 2775–2783. ISSN: 00063495. DOI: `10.1016/S0006-3495(02)75618-X`.

[86] Jerry Chao, E Sally Ward, and Raimund J Ober. "Localization accuracy in single molecule microscopy using electron-multiplying charge-coupled device cameras". In: *Proc SPIE Int Soc Opt Eng* 8227 (Mar. 2012). ISSN: 0277-786X (Print) 1996-756X (Linking). DOI: 10.1117/12.908951.

[87] Jonathan B Grimm et al. "Bright photoactivatable fluorophores for single-molecule imaging". In: *Nature Methods* 13.12 (Dec. 2016), pp. 985–988. ISSN: 1548-7091. DOI: 10.1038/nmeth.4034.

[88] Jonathan B Grimm et al. "A general method to fine-tune fluorophores for live-cell and in vivo imaging". In: *Nature Methods* 14.10 (Oct. 2017), pp. 987–994. ISSN: 1548-7091. DOI: 10.1038/nmeth.4403.

[89] Martin Storath, Andreas Weinmann, and Laurent Demaret. "Jump-sparse and sparse recovery using potts functionals". In: *IEEE Transactions on Signal Processing* (2014). ISSN: 1053587X. DOI: 10.1109/TSP.2014.2329263. arXiv: 1304.4373.

[90] Willi L. Stepp and Zeynep Ökten. "Resolving kinesin stepping: one head at a time". In: *bioRxiv* (May 2019), p. 651281. DOI: 10.1101/651281.

[91] Arthur J Michalek et al. "Full-length myosin Va exhibits altered gating during processive movement on actin". In: *Proceedings of the National Academy of Sciences* 109.5 (Jan. 2012), E218–E224. ISSN: 0027-8424. DOI: 10.1073/pnas.1109709109.

[92] David D Hackney. "Kinesin ATPase: Rate-limiting ADP release". In: *Proc Natl Acad Sci U S A* 85.17 (Sept. 1988), pp. 6314–8. ISSN: 0027-8424.

[93] Ahmet Yildiz et al. "Intramolecular strain coordinates kinesin stepping behavior along microtubules". In: *Cell* 134.6 (Sept. 2008), pp. 1030–1041. ISSN: 1097-4172 (Electronic) 0092-8674 (Linking). DOI: 10.1016/j.cell.2008.07.018.

[94] S Ray et al. "Kinesin follows the microtubule's protofilament axis". In: *J Cell Biol* 121.5 (1993), pp. 1083–1093. ISSN: 0021-9525 (Print) 0021-9525 (Linking).

[95] Melanie Deborah Brunnbauer. "Mechanische Untersuchungen heterodimerer Kinesin-2 Motoren". PhD thesis. 2011, XI, 102 S.

[96] Allison M. Gicking et al. "The Orphan Kinesin PAKRP2 Achieves Processive Motility via a Noncanonical Stepping Mechanism". In: *Biophysical Journal* 116.7 (Apr. 2019), pp. 1270–1281. ISSN: 15420086. DOI: 10.1016/j.bpj.2019.02.019.

[97] J Kerssemakers et al. "The distance that kinesin-1 holds its cargo from the microtubule surface measured by fluorescence interference contrast microscopy". In: *Proc Natl Acad Sci U S A* 103.43 (2006), pp. 15812–15817. ISSN: 0027-8424 (Print) 0027-8424 (Linking). DOI: `10.1073/pnas.0510400103`.

[98] A Maheshwari et al. "alpha- and beta-Tubulin Lattice of the Axonemal Microtubule Doublet and Binding Proteins Revealed by Single Particle Cryo-Electron Microscopy and Tomography". In: *Structure* 23.9 (2015), pp. 1584–1595. ISSN: 1878-4186 (Electronic) 0969-2126 (Linking). DOI: `10.1016/j.str.2015.06.017`.

[99] Toshiyuki Oda, Haruaki Yanagisawa, and Masahide Kikkawa. "Detailed structural and biochemical characterization of the nexin-dynein regulatory complex". In: *Molecular Biology of the Cell* 26.2 (Jan. 2015). Ed. by Wallace Marshall, pp. 294–304. ISSN: 1059-1524. DOI: `10.1091/mbc.E14-09-1367`.

[100] J M Scholey. "Cilium assembly: delivery of tubulin by kinesin-2-powered trains". In: *Curr Biol* 23.21 (2013), R956–9. ISSN: 1879-0445 (Electronic) 0960-9822 (Linking). DOI: `10.1016/j.cub.2013.09.032`.

[101] David R. Mitchell. "The Evolution of Eukaryotic Cilia and Flagella as Motile and Sensory Organelles". In: *Eukaryotic Membranes and Cytoskeleton*. New York, NY: Springer New York, 2007, pp. 130–140. DOI: `10.1007/978-0-387-74021-8_11`.

[102] Georgyi V. Los et al. "HaloTag: a novel protein labeling technology for cell imaging and protein analysis". In: *ACS Chem Biol* 3.6 (June 2008), pp. 373–382. ISSN: 1554-8937 (Electronic) 1554-8929 (Linking). DOI: `10.1021/cb800025k`.

[103] A Keppler et al. "A general method for the covalent labeling of fusion proteins with small molecules in vivo". In: *Nat Biotechnol* 21.1 (2003), pp. 86–89. ISSN: 1087-0156 (Print) 1087-0156 (Linking). DOI: `10.1038/nbt765`.

[104] N J Carter and R A Cross. "Mechanics of the kinesin step". In: *Nature* 435.7040 (2005), pp. 308–312. ISSN: 1476-4687 (Electronic) 0028-0836 (Linking). DOI: `10.1038/nature03528`.

[105] Raghuveer Parthasarathy. "Rapid, accurate particle tracking by calculation of radial symmetry centers". In: *Nature Methods* (2012). ISSN: 15487091. DOI: `10.1038/nmeth.2071`.

[106]   Angela Oberhofer et al. "Myosin Va's adaptor protein melanophilin enforces track selection on the microtubule and actin networks in vitro". In: *Proceedings of the National Academy of Sciences* (2017). DOI: 10.1073/pnas.1619473114.

[107]   Melissa Linkert et al. "Metadata matters: access to image data in the real world". In: *The Journal of Cell Biology* 189.5 (May 2010), pp. 777–782. ISSN: 0021-9525. DOI: 10.1083/JCB.201004104.

Acknowledgment

I would like to thank everyone that helped to make this work possible over the last years. Many of these people have not only been involved in this work, but also in my bachelor and master thesis and therefore in almost my whole academic life.

Thank You Zeynep, for the possibility to work in your lab for a pretty long time, for your enthusiasm and guidance. This includes scientific questions, but also negotiation skills and politics in academia.

Thank You Angela for the introduction into the world of biochemistry and the patience for a physicist that uses a pipette for the first time. For all the discussions, the days of skiing and for being an absolute role model for reliability and work attitude.

Thank You Hieu, I can't imagine what life in the lab would be like without you. I can't appreciate enough all the countless times you have helped me out and saved me.

Thank You Melanie, especially for the outside but insider view on things over the last years.

Thank You Rudi for always having an open ear for my extravagant component ideas for the microscope. The setup would not be what it is without your contributions.

Thank You Mohamed for being a good friend, for the runs and genuine insights into your culture.

Thank You E22, E27 and the Dietz group for all the discussions and a work environment that always let me go to work in a good mood over the years.

Thank You dad for letting me find my own way into physics. Thank you for all the discussion and for a genuine interest in my work. Less pretentious, thank you for reading this manuscript and your input.

Thank You mum for always open ears and support. For all the deep insights into how people work and the tactical guidance in interpersonal matters.

Thank You Klara for being the best sister a brother could ask for.

Thank You Ali for the company during the last stretch of this work.